NEUTRON-UNBOUND STATES IN THE NUCLEUS ^{31}NE

By

Dayah Chrisman

A DISSERTATION

Submitted to
Michigan State University
in partial fulfillment of the requirements
for the degree of

Physics - Doctor of Philosophy

2022

ABSTRACT

NEUTRON-UNBOUND STATES IN THE NUCLEUS ^{31}NE

By

Dayah Chrisman

Studies of nuclei far from stability reveal trends among groups of neighboring nuclei where new and unexpected properties appear. One such region, the Island of Inversion near the $N = 20$ shell gap, is home to nuclei with reordered single-particle energy levels compared to the spherical shell model. Studies of the ^{31}Ne nucleus have revealed that its ground state has a halo component, characterized by a valence neutron orbiting a deformed ^{30}Ne core. This lightly-bound nucleus with a separation energy of $S_n = 0.15^{+0.16}_{-0.10}$ MeV is expected to have excited states that are neutron unbound.

This work presents a first study of the neutron-unbound excited states of ^{31}Ne. Neutron-unbound states in ^{31}Ne were populated in a two-proton knockout reaction from an 89 MeV/u ^{33}Mg beam incident on a segmented Be reaction target. The ^{30}Ne fragment and associated neutron from the decay of ^{31}Ne* were detected by the MoNA-LISA-Sweeper experimental setup at the National Superconducting Cyclotron Laboratory. Invariant mass spectroscopy was used to reconstruct the two-body decay energy ($^{30}\mathrm{Ne} + \mathrm{n}$).

The two-body decay energy spectrum exhibits two features: a low-lying peak at 0.30 ± 0.17 MeV and a broad enhancement at 1.50 ± 0.33 MeV, each fit with an energy-dependent asymmetric Breit-Wigner line shape representing a resonance in the continuum. Accompanying shell model calculations combined with cross-section calculations using the eikonal reaction theory indicate that these features in the decay energy spectrum originate from

multiple resonant states in ^{31}Ne.

ACKNOWLEDGMENTS

I have found an incredible amount of support during my graduate school experience at Michigan State University from my advisors, the MoNA research group, collaborators, MSU and NSCL personnel, and my fellow graduate students. I would first like to thank my advisors, Michael Thoennessen and Artemis Spyrou, for their dedication, guidance, and encouragement. Paul Gueye also served the role of an advisor within the MoNA research group, and similarly provided another source of support and expertise. I would also like to thank the members of my thesis committee, Kirsten Tollefson, Scott Bogner, and Jaideep Singh for their time, feedback, and advice during our meetings.

I would like to thank B. Alex Brown and Jeff Tostevin for their collaboration in nuclear theory matters, providing their expertise, contributing significantly to the interpretation of this work and collaborating on a research paper. Their attentive support and willingness to answer any questions made the work valuable and rewarding.

Working with the MoNA collaboration has been extremely rewarding. From the day I joined they made me feel welcome, providing extensive support throughout my time as a research assistant. I would like to thank Anthony Kuchera, Nathan Frank, Thomas Baumann, and Paul DeYoung for their assistance in experimental research matters from beginning to end and showing dedication to my success. I also want to thank my fellow graduate students within the MoNA research group who influenced my time at MSU. Thomas Redpath, Han Liu, Krystin Stiefel, and Daniel Votaw all provided valuable feedback and discussion in research matters as well as coursework.

A special thank you to Kim Crosslan, whose immense patience and attention I strongly value.

She shut down any misconceptions I had about my own academic ability, and remembered my name and face the first day I started. She made me feel welcome and supported, especially in the first year when I was finding my footing as a new graduate student.

In my time at MSU, I was fortunate enough to meet other students who proved to be some of my best friends. Sara Miskovich, Mara Grinder, and Aalayah Spencer showed me undying support through their friendship, studying together and brainstorming in our office, and capturing our best quotes to hang on the whiteboard. They became a group to relax with after long days of study, with camping trips, weekly visits to the rock-climbing gym, and, of course, considering buying a goat share together. I count myself lucky to have met them and found their support during some of the toughest parts of my life.

I would also like to thank the friends and family that helped me throughout my academic pursuits. They have encouraged me in my interest in math and science, made it possible to attend college, and have supported me through all the stress it entails. Thank you to my parents for always making sure I had what I needed to continue my education in any direction I decided, even when it meant moving far from home. A special thanks to my sister Leah for the gaming sessions, the open ear, and providing feedback on my thesis and cover letters. Another special thanks goes to Tiarra Stout, my best friend from my time as an undergraduate, providing a sense of sisterhood I needed in my home-away-from-home and encouraging me to join a dance club. Doing homework together, dancing together, and climbing to the peak of Mt. Borah together are some of my favorite memories, which wouldn't have happened if we hadn't both pursued physics degrees and found immense support in the other. I also want to thank Torry Torres for being a close and long-term support in my life. These contributions from friends and family encouraged my passion and kept me going

through struggles, academic and otherwise.

TABLE OF CONTENTS

LIST OF TABLES

LIST OF FIGURES

Chapter 1

Introduction

1.1 The nuclear landscape

An atomic nucleus is a many-body system comprised of one or more protons and neutrons. Each species of atomic nucleus, called a nuclide, is identified by the number of protons (or atomic number, Z) and number of neutrons (N) it contains. The chart of nuclides arranges all known nuclear species plotted on the (N, Z) plane, shown in Figure 1.1. The total mass number $A = Z + N$ is often used with the atomic number (Z) to refer to a nucleus. A common notation for nuclides is ${}^{A}_{Z}X_{N}$, or more concisely, ${}^{A}X$, where X is the atomic symbol corresponding to the atomic number (Z). Isotopes are nuclei which have the same atomic number (Z) but varying neutron number (N) and are visualized as rows in the chart of nuclides. Conversely, isotones are nuclei with the same N but different Z, visualized as columns in the chart of nuclides. Isobars are nuclei with identical mass number A, visualized on the diagonal from top left to bottom right within the chart of nuclides. The central region containing stable nuclei (denoted by black boxes in Figure 1.1) is often referred to as the "valley of stability" in the nuclear landscape.

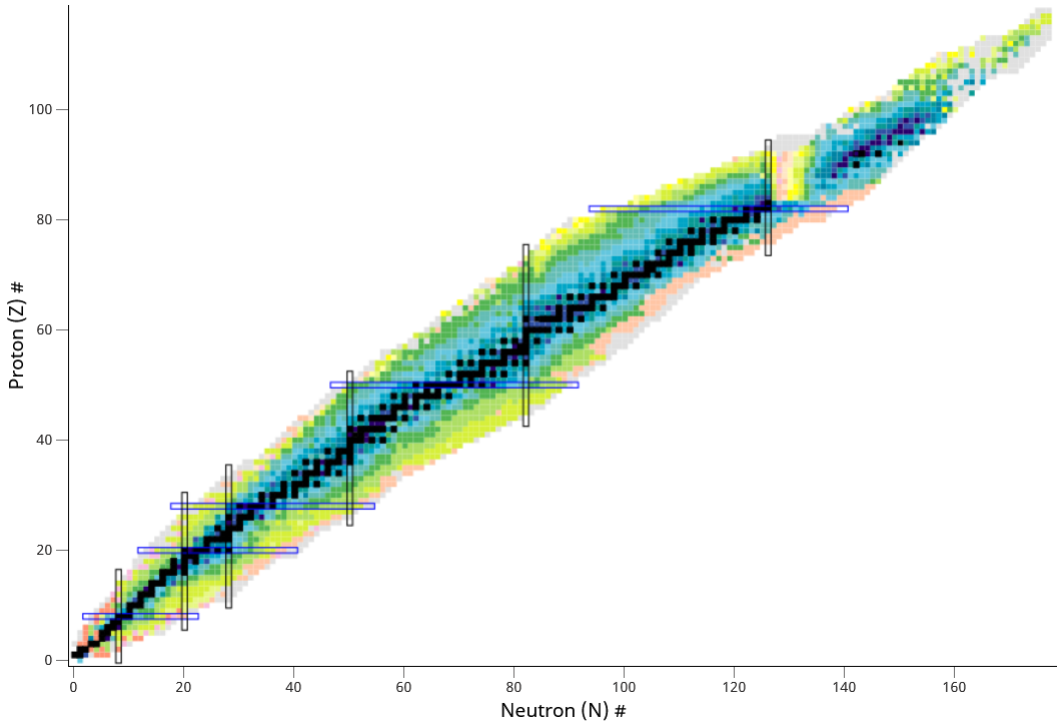

Figure 1.1: The chart of nuclides from National Nuclear Data Center (NNDC) [1]. Colors represent ground-state half lives.

1.1.1 Nuclear stability

Generally speaking, the further a nuclide is from the "valley of stability" on the nuclear chart, the faster it will decay back toward stability. On either side of the valley are nuclei susceptible to decay over some time scale. Observed half-lives for unstable nuclei range from longer than the age of the universe down to $10^{-}22$ s for particle-unbound nuclei.

On the neutron-deficient side of the valley of stability (left), the primary decay mode is β^{+} decay, turning a proton into a neutron. On the neutron-rich side of the valley (right) the trend is the opposite: β^{-} decay turning a neutron into a proton. Far from the valley of stability in neutron-rich nuclei, half-lives drop significantly from roughly 1 ms down to about 1^{-18} ms. The "weak" nuclear force responsible for β decay processes have characteristic half-lives much longer compared to the "strong" nuclear force which is responsible for binding

nucleons together. The timescale of the strong nuclear force (1^{-18} ms) is characteristic of the motion of the nucleons within a nucleus and can be used as a lower limit for the condition of nuclear existence.

The one-neutron separation energy S_n refers to the amount of energy needed to separate one neutron from a specific nuclide, the trends of which can be examined to expose patterns of nuclear properties. For nuclides that meet the condition of existence and for which the ground state energetically favors emitting a nucleon (having a negative one-nucleon separation energy), the nucleus decays directly by nucleon emission and are considered particle-unbound nuclei. The location on the nuclear chart where this happens is called the neutron "dripline" [6]. The limits of the nuclear chart and the limits of nuclear existence have yet to be fully explored. One of the main goals of nuclear physics research is to predict the interactions of protons and neutrons and the nuclei they form using a concise, cohesive model across all nuclear systems.

1.1.2 Nuclear theory methods

Theoretical approaches to nuclear physics are numerous and are, individually, applicable to some range of nuclei. The strong nuclear force is fundamentally what determines the nuclear structure. In the Standard Model of particle physics, protons and neutrons are built from elementary particles called quarks. Nuclear interactions can be built using Quantun Chromo-Dynamics (QCD) to model the exchange of gluons between the quarks that make up the nucleons in the Standard Model. The typical energy regime of nuclear physics makes the calculation non-trivial (requiring lattice QCD) and it is computationally expensive, thus an easier access to nuclei with very few nucleons [7]. An effective field theory (EFT) for nucleons

and mesons is equivalent to the QCD calculation if it obeys the same symmetries [8]. With an EFT, slightly higher nuclear mass numbers than lattice QCD can be reached because nuclei are built starting from nucleon-nucleon interactions [9]. However, the calculations quickly become computationally intensive similar to lattice QCD. This limitation encourages an empirical approach to nuclear physics theory where experimental data informs the model used. Configuration interaction (CI) methods can predict physical properties by applying an appropriate interaction model based on a range of applicability, often determined by location in the nuclear chart or by a specific mass regime, where the calculations are guided by experimental data. The nuclear shell model is an example of one such theoretical approach and is discussed in the next section.

For the heaviest nuclei, even configuration interaction methods are limited by the cost of computation. A density functional theory (DFT), such as those used in atomic and condensed matter physics, uses continuous densities and currents rather than individual particles to calculate ground and excited state energies. Combining these methods and their range of applicability, theorists can model and study nuclear systems with any number of nucleons, extending to predictions for superheavy [10] and hyperheavy [11] nuclides which have yet to be observed.

Though nuclear properties can be mostly accounted for using an approach for the appropriate mass regime, a unified method is sought which has predictive power spanning the nuclear chart in its entirety. Experimental data can help to benchmark these theory approaches and inform the models used to describe nuclear properties.

1.2 The nuclear shell model

The nuclear shell model is an example of a configuration interaction (CI) approach to nuclear structure theory, where empirical observation informs models of a nuclear potential.

Along the nuclear chart, patterns of stability indicated by sharp drops in quantities such as binding energy were observed at a "magic number" of either protons or neutrons (2, 8, 20, 28, 50, 52, etc.). The liquid drop model proposed by Gamow [12] worked well to describe the binding energy of many stable nuclei, but could not account for this pattern. The appearance of these "magic numbers" hinted at a shell structure not unlike electron shells in atoms, where atoms with closed electron shells (noble gases) require a significant amount of energy (compared to atoms without closed electron shells) to remove an electron. A new set of interactions needed to be developed that could reproduce this pattern of enhanced stability due to nucleonic "shell" structure and explain the observed trends at the "magic numbers."

The shell model framework describes a nucleon moving in a mean-field potential $V(r)$. A Hamiltonian is built with matrix elements determined by an empirically-chosen potential for the appropriate mass regime. The eigenvalues and eigenstates are characterized by a set of quantum numbers (n, l, j, and energy E) and used to predict nuclear structure properties. To build a nuclear shell model, an appropriate potential $V(r)$ describing the nucleon interaction is characterized in three key areas of the nucleus: the interior, the surface, and the exterior. The potential for a bound nucleus should be attractive ($V(r) < 0$) and roughly flat in the "interior," assuming the nucleon-nucleon interaction is short-range and the nuclear density is constant. Near the surface of the nucleus, $V(r)$ weakens to reflect the smaller number of interactions available to the outer nucleons. At distances greater than the range

of interaction, $V(r)$ approaches zero. As a first approximation, the harmonic oscillator (HO) is chosen as $V(r)$ due to its simple and analytic nature. However, the shape of a Woods-Saxon potential more closely resembles the shape of nuclear densities obtained empirically. The nuclear potential $V(r)$ is used to generate a spectrum of energy levels available to the nucleons.

A Woods-Saxon potential is defined by

$$f(r) = \frac{V_0}{1 + e^{(r-R_0)/a_0}} \tag{1.1}$$

where V_0, R_0, and a_0 are fitted to reproduce experimental binding energies. However, the Woods-Saxon potential alone is insufficient in reproducing the experimentally-observed magic numbers. In 1949 Mayer and Jensen added a spin-orbit component [13, 14, 15], resulting in energy-level spacing that correctly reproduced the large gaps in the single-particle energy at the observed "magic numbers," for which they earned the Nobel Prize in Physics in 1963.

Figure 1.2 shows the energy levels for the harmonic oscillator, Woods-Saxon, and Woods-Saxon plus spin-orbit potentials. The Mayer and Jensen model clearly exhibits characteristic shell closures at the magic numbers, labeled by the numbers between energy levels in Figure 1.2. The spin-orbit term can be understood as a valence nucleon experiencing "residual" interactions with other valence nucleons. The Woods-Saxon plus spin-orbit potential require parameters for the mean-field potential (Woods-Saxon) and a model for the residual interaction (spin-orbit) to calculate observable quantities.

The shell model is best-suited to nuclei at or near shell closures, where there are very few

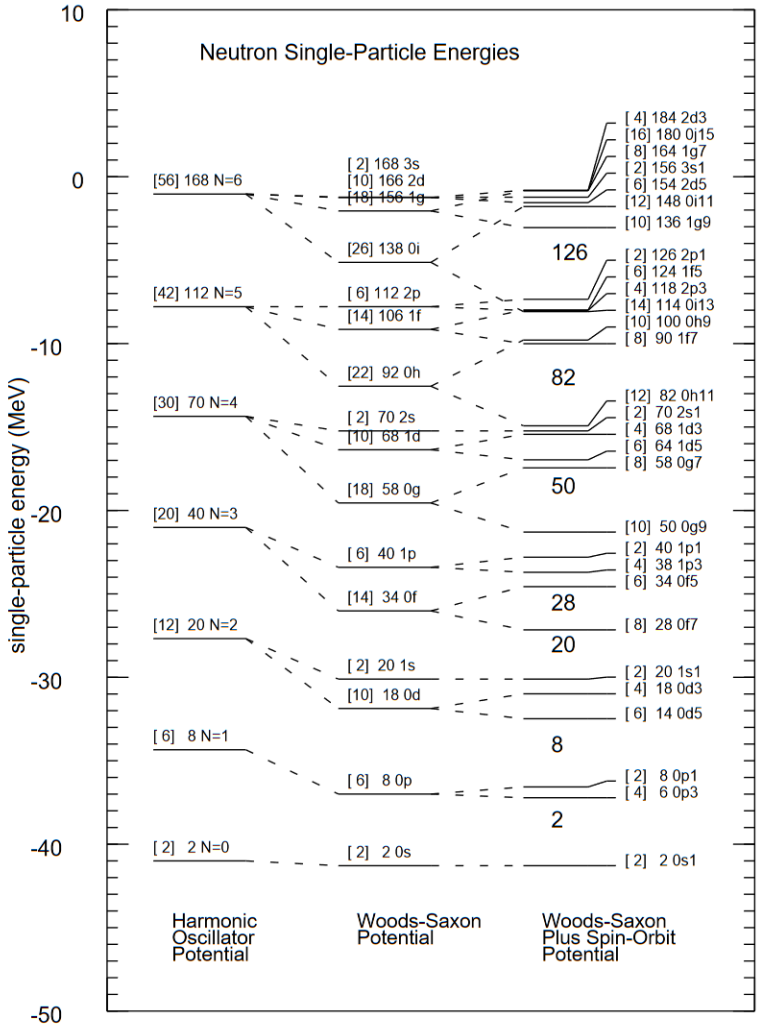

Figure 1.2: Shell model single-particle energy levels based on a harmonic oscillator potential (left), a Woods-Saxon potential (center), and a Woods-Saxon plus spin-orbit potential (right). Note that the latter creates the gaps in energy levels at the experimentally observed "magic numbers." For each energy level, the labels indicate: the nucleon capacity in square brackets followed by the cumulative nucleon capacity and then the orbital label. The orbitals for the Woods-Saxon are in spectroscopic notation where the number is an index of the number of levels with a certain l-value. In the Woods-Saxon plus spin-orbit levels, the additional last integer is $2j$ where j is the total angular momentum quantum number given by $j = l \pm s$. Figure reproduced from reference [2]

(or zero) valence nucleons and the residual interactions are small. Away from closed shells, the participation of more valence nucleons makes the residual interaction more significant: anomalies in nuclear structure such as deformation and collective motion are often found between shells where the mean-field description breaks down. The appearance, development, and evolution of shell structure across the nuclear chart is an attractive subject, particularly for unstable and near-stable nuclei.

1.2.1 Shell evolution and inversion

Properties of nuclei at or near shell closures are well-described by the shell model and show remarkable agreement with experimental data. However, nuclei far from stability have recently become a focus area for nuclear physics. Patterns among nuclei near the edges of the nuclear chart emerge that indicate a departure from standard shell structure [16] and increased nuclear deformation[17].

Nuclear deformation arising from features such as nuclear rotations associated with quadrupole deformation of the nucleus involves collective motion of many nucleons rather than the motion of only a few valence particles. Rotational collectivity can enhance binding energy based on the projection of a valence orbit onto the symmetry axis of prolate or oblate deformed nuclei [18].

The spherical shell model is based on a spherically symmetric nuclear potential, which, while appropriate for stable and near-stable nuclei, cannot explain collective nuclear structure features that vary smoothly with mass number A. This trend is accounted for when quadrupole collectivity is considered using a deformed nuclear potential, resulting in shell model energy levels that depend on the spatial orientation of an occupied orbit. Thus, the experimentally

observed enhanced binding energies suggest a strong degree of quadrupole deformation [19]. The deformed nuclear potential can produce energy levels of single-particle orbits in which normal shell ordering dictated by a spherical nuclear potential is broken. This uncovers a "shell inversion," or re-ordering of neutron orbitals relative to those obtained with spherical potential at a high degree of deformation. Regions of the nuclear chart where this shell inversion is characteristic are called "Islands of Inversion." [3] The $N = 20$ Island of Inversion is one such region, centered at $Z = 11$ and $N =$ 21 as shown in Figure 1.3. These nuclei

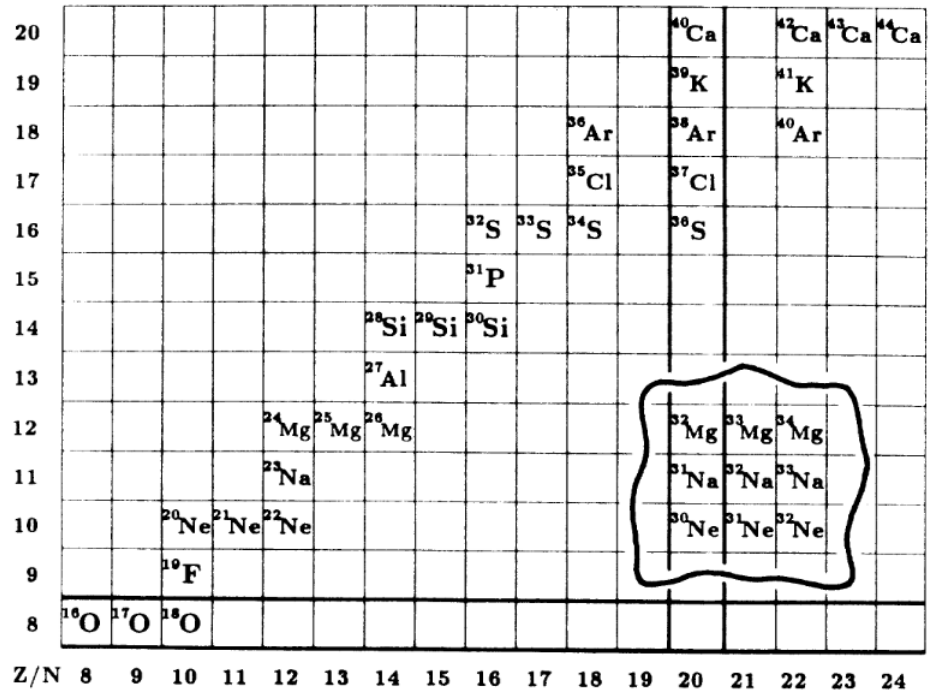

Figure 1.3: The nuclei belonging to the $N = 20$ island of inversion. Figure reproduced from reference [3].

were shown to exhibit a change in shell structure through studies of the very neutron-rich nuclei ^{31}Na and ^{32}Mg [20]. Large-scale shell model calculations indicate the conventional N=20 shell gap is diminished for neutron-rich nuclei with Z ¡= 12, giving rise to anomalous properties brought on by deformation effects [16, 17, 21]. This deformation can be described

within the Nilsson model [22] which uses a quadrupole deformed nuclear potential, producing energy levels that change smoothly with a deformation parameter. Because the nuclear potential for neutrons only has a centrifugal barrier, orbitals with low angular momentum (l=0, 1) can form a density "tail" extending the nuclear matter radius, which can indicate shell inversion if the conventionally-occupied shell model orbit cannot account for this effect. One way to observe this anomaly is through cross-section measurements of a nuclear interaction. The reaction rate is represented by the quantity σ called the cross-section, determined by the fraction of detected to incident particles. Measurements of one-nucleon removal cross-sections on both a heavy (Pb) and a light (C) target can be combined to distinguish the relative contributions of Coulomb and nuclear effects to a breakup reaction and a Coulomb-breakup cross section can be extracted. A large coulomb-breakup cross section is indicative of an underlying halo structure, meaning the nucleus can be modeled as a two-body system composed of a "core" nucleus with one (or two) weakly-bound valence nucleons where the core-valence interaction is small. These are often found in deformed nuclei far from stability, and they exhibit strong single-particle structure.

The observed nuclear properties of various nuclei in this region have been successfully reproduced by the shell model for both stable and unstable nuclei where experimental data is available [21, 3, 16]. However, there are some neutron-rich nuclei for which no experimental data is available. Experimental studies concerning nuclei near and past the neutron drip line provide valuable insight into trends of nuclear existence. Such studies can also validate and inform the creation of shell model Hamiltonians for a wide range of nuclear masses. The nuclear properties characteristic of the $N = 20$ island of inversion are discussed in the next section.

1.2.2 The $N = 20$ island of inversion

Energy levels of nuclei near the valley of stability have significant gaps in their level spacing at "magic numbers" of nucleons (2, 8, 20, 28, 50, 52, etc.). However, near the neutron dripline where deformation plays a role, the shell structure changes [16]. Deformation in the neutron-rich $N \approx 20$ nuclei causes some orbitals to rearrange themselves based on their spatial orientation relative to the deformed nucleus, closing the conventional $N = 20$ shell gap at large N/Z [16].

Shell model calculations construct their basis states relative to a closed-shell configuration. To describe the $N = 20$ (a "magic number") near-dripline nuclei, an appropriate configuration space involves particles promoted to orbitals that conventionally lie across a large energy gap. For neutron number $N \approx 20$, the configuration space considers neutron particles and holes in both the *sd*-shell and the fp-shell on either side of the $N = 20$ shell gap. A simple schematic is shown in Figure 1.4 illustrating the closed shell and the active shells in the calculation. Shell model calculations indicate the 2p-2h configuration is lower in energy than the 0p-0h state for some nuclei in the N=20 isotones. The strong degree of ground-state deformation near the drip line is associated with the dominance of two-particle two-hole excitations (2p-2h) across the diminished gap between the *sd* and fp shells [17, 21, 16].

Both configurations are compared in Figure 1.5, with zero denoted by a solid horizontal line. An increase in the neutron pairing energy E_{nn} and the proton-neutron interaction energy E_{pn} lowers the relative energy of the 2p-2h configurations [3, 4]. The island of inversion includes the $N = 20$ nuclei circled in Figure 1.5 where the gap energy between 2p-2h and 0p-0h configurations becomes negative, that is also observed in $Z = 10 - 12$, $N = 20 - 22$ nuclei. Nuclei with few protons outside the $Z = 8$ shell closure experience an increase in

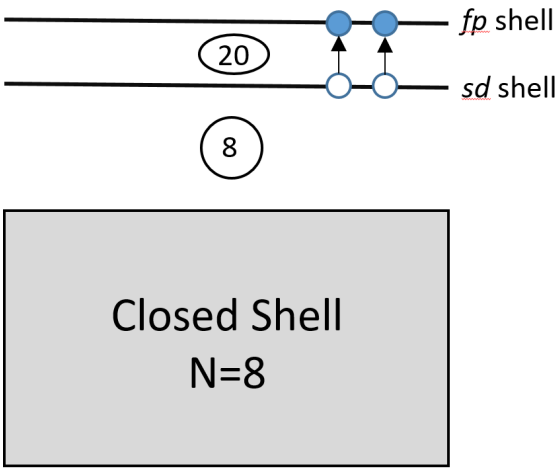

Figure 1.4: A sample version of a model space showing closed shells and active orbitals for neutrons near $N = 20$. The closed shell at magic number $N = 8$ is represented by the shaded box and includes the $0s$ and $0p$ orbitals. The sd shell contains active orbitals $1s$ and $0d$ and is shown as one bar for simplicity. The $N = 20$ shell gap shown here is small, with a two-particle two-hole excitation illustrated. The fp shell includes $0f$ and $1p$ active orbitals and is depicted as one bar.

neutron-proton interaction energy (E_{pn}).

The configuration space is the collection of particle-hole wavefunctions that define the basis states for the shell model calculation. Therefore, a nuclear wavefunction generally contains a mixture of different particle-hole configurations (1p-1h, 2p-2h, 3p-3h, etc.). In the $N = 20$ island of inversion nuclei, strong configuration mixing arises from competition between the mean-field approach (favoring 0p-0h) and the growing nuclear correlations (favoring deformed 2p-2h).

The collective structure and associated degree of deformation for these nuclei are encouraged by the nearly-degenerate $p_{3/2}$ and $f_{7/2}$ orbitals in the fp-shell. A transition from a spherical to a deformed nuclear shape at $N = 20$ occurs, driven by large correlation energies of the deformed configurations [21, 23].

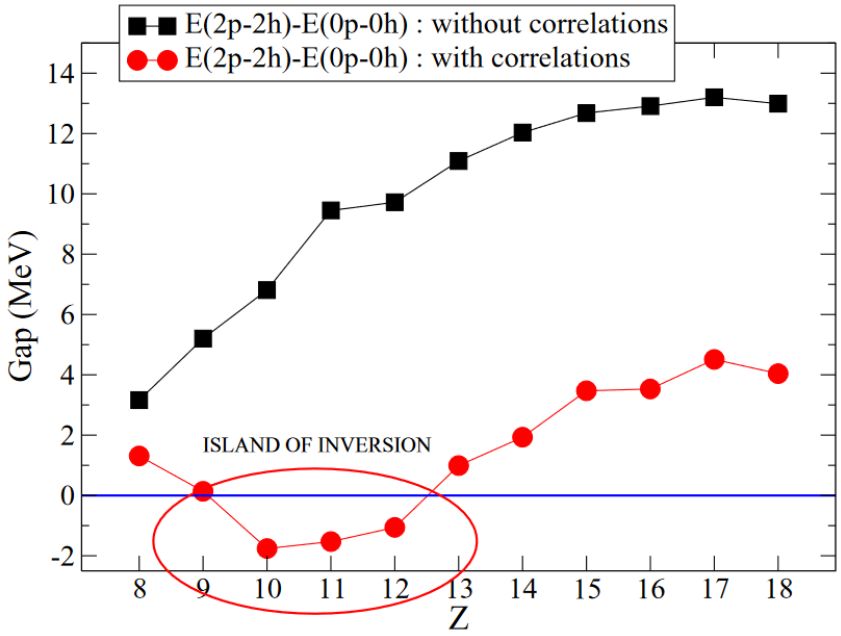

Figure 1.5: The energy gap between the 0p-0h and 2p-2h configurations for $N = 20$ isotones, plotted without correlations (squares) and including correlations (circles). A horizontal line marks zero, where the two configurations have the same energy. Nuclei below are possible members of the island of inversion. Figure reproduced from reference [4].

Some odd-N nuclei near $N = 20$ exhibit novel structures through the occupation of low angular momentum single particle orbitals. For example, a nucleus with one neutron in the fp-shell ($N = 21$) may have its occupancy split between the $p_{3/2}$ and $f_{7/2}$ orbitals. The un-paired neutron would conventionally occupy the $f_{7/2}$ orbital ($l = 3$), which is suppressed by the centrifugal barrier for the neutron potential, and contributions from the p orbitals ($l = 1$) can grow. For example, the nucleus ^{31}Ne exhibits the occupation of a low angular momentum orbit [24, 25] not predicted by the spherical shell model. This results in the idea of a halo structure, composed of a deformed ^{30}Ne core plus one valence neutron, with a particle or hole in a low-l orbital. The ^{31}Ne nucleus is the focus of this work and is discussed in further detail in the next section.

1.2.3 Previous studies of ^{31}Ne

The trends of nuclear structure and existence toward the drip line indicate a breakdown of the conventional shell model "magic numbers" arising from deformation attributed to intruder configurations in regions of the chart referred to as the "islands of inversion"[3, 4, 26].

The nuclear potential for neutrons has a centrifugal barrier that strengthens with the orbital's angular momentum l, and no Coulomb barrier to contend with. Thus, halo structures in this region are associated with low-l intruder orbitals, and cross-section measurements and calculations can give insight into the mechanism of this structure formation. The cross section represents the "size" of the nucleus, interpreted as a probability of an interaction. An example is a one-neutron removal cross section, where the interaction in question is the removal of one neutron from the nucleus. In the spherical-potential shell model (shown on the right in Figure 1.2), the valence neutron of ^{31}Ne ($N = 21$) would occupy the $1f_{7/2}$ orbital (l=3). However, in the $N = 20$ island of inversion, normal and intruder configurations mix considerably and give way to deformation and collective structure effects. Shell model calculations performed by Warburton, Becker, and Brown [3] placed ^{31}Ne among the $N = 20$ island of inversion nuclei, characterized by a lowering of the deformed $2\hbar\omega$ configuration below that of the $0\hbar\omega$ configuration. A 1996 experiment [27] established the particle-stability of ^{31}Ne with respect to one-neutron decay, previously thought to be particle-unbound due to non-observation in a 1990 experiment [28]. Mass measurements [29] indicated an ambiguous one-neutron separation energy $S_n = 0.29 \pm 1.64$ MeV with a large uncertainty where both bound and unbound scenarios are in line with these mass measurements.Measurements of the one-neutron removal cross section of ^{31}Ne on ^{12}C and ^{208}Pb targets performed by Nakamura et al. in 2009 indicated a large Coulomb-breakup cross section [24], suggesting the valence

neutron occupies a low-l orbital with a small separation energy ($S_n \leq 0.8$ MeV), consistent with the formation of a halo structure. Nakamura, et al. performed one-neutron removal cross section measurements in 2014 with the addition of gamma-ray detection, the analysis of which indicated the separation energy to be $S_n = 0.15^{+0.16}_{-0.10}$ MeV, the "smallest S_n of any known neutron-rich nucleus" [25]. Both experiments indicated the occupancy of a low-l intruder orbital (l=0,1) is responsible for the halo formation. The spin-parity of the ground state was determined to be $\frac{3}{2}^-$ with the halo formed by "a weakly-bound p-wave neutron carrying only about 30% of a single-nucleon strength," indicating strong configuration-mixing of fp orbitals [25]. A study of nuclear radii [30] and interaction cross sections [31, 32] in the neon isotopes revealed a dramatic increase for ^{31}Ne as seen in Figure 1.6 consistent with a low-l orbital occupation for a weakly-bound valence neutron and with previous experimental studies [24, 25]. Coulomb breakup cross sections calculated within the Glauber and Eikonal models [33] also suggest a ground-state spin-parity of $\frac{3}{2}^-$ and confirm that the $1f_{7/2}$ configuration yields much smaller cross sections than $2p_{3/2}$, solidifying the link between halo structure and inversion observed for ^{31}Ne.

Nilsson model [22] calculations use a quadrupole deformed nuclear potential, placing limits on the combination of a one-neutron separation energy (S_n) and a ground state spin-parity assignment by comparison with experimentally measured cross sections [24]. Specifically, if $S_n < 500$ keV then the ground state can be a p-wave halo with spin-parity $3/2^-$. However, the possibility of a ground-state spin-parity of $\frac{1}{2}^+$ remains, which would indicate a high degree of deformation ($\beta_2 \geq 0.6$) and a radical change in shell structure [34, 35]. Studies within the particle rotor model [36, 37] that include core excitations suggest ^{31}Ne has a very low one-neutron separation energy ($0.13 \leq S_n \leq 0.20$ MeV). Its ground state spin-parity

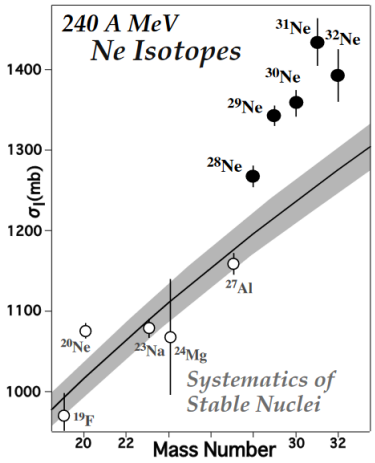

Figure 1.6: Interaction cross-sections σ_I taken from ref. [**?**]. Solid markers represent σ_I for neon isotopes with the solid line representing systematics of stable nuclei. Existing stable-nuclide data (σ_I for ^{19}F, ^{24}Mg, ^{20}Ne and ^{23}Na and σ_R for ^{27}Al) is shown in open markers.

was suggested to be $\frac{3}{2}^-$ with quadrupole deformation β_2=0.20 based on comparison with measured Coulomb-breakup and reaction cross sections [24]. However, the possibility of spin-parity $\frac{1}{2}^+$ is not excluded, though it requires a large $\beta_2 \sim 0.95$.

Deformation effects on reaction observables were studied in the framework of anti-symmetrized molecular dynamics (AMD) [38], but the drastically large cross section could not be reproduced for ^{31}Ne without a modification for the nuclear matter density using the resonating group method (RGM) [5, 39], resulting in the density distribution shown in Figure 1.7 . The tail of this density distribution is especially significant for ^{31}Ne, with the largest cross section of the neon isotopes. Kimura et al. [40] also performed AMD calculations with a tail correction provided by RGM and determined that the ^{31}Ne ground state can be well-described by a valence neutron in a $2p_{3/2}$ orbital coupling to a deformed and rotating ^{30}Ne ground band. They also calculated the one-neutron separation energy to be S_n=0.45 MeV. The structure of the ^{31}Ne ground state is well described as a prolate-deformed halo nucleus with a weakly-bound valence neutron occupying a low-l intruder orbital and a ground state spin-parity of

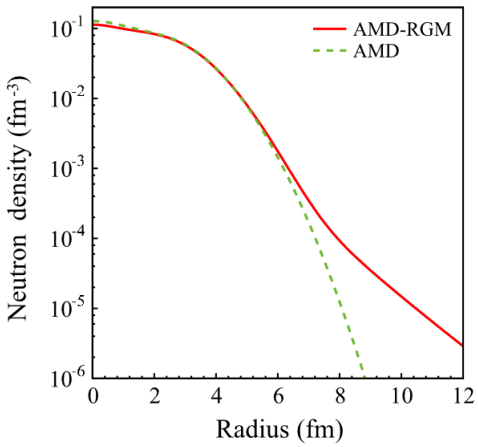

Figure 1.7: Neutron one-body densities in ^{31}Ne. The results of the calculation with AMD is shown by the dashed line, and the result from AMD + RGM is shown by the solid line. Taken from reference [5].

$\frac{3}{2}^-$, though the possibility of $\frac{1}{2}^+$ cannot be excluded [40]. It is useful to consider the one-neutron separation energy for ^{31}Ne: it was originally taken from mass measurements [29] as $S_n = 0.29 \pm 1.64$ MeV. This was the value used until 2014 when Nakamura et al. [25] obtained the value $S_n = 0.15^{+0.16}_{-0.10}$ MeV. The ambiguity of the one-neutron separation energy, while improved, challenges the predictions and interpretations of the low-energy spectrum of ^{31}Ne. With such a weak binding, this nucleus likely has low-lying excited states that are neutron-unbound, or a resonance of the ^{30}Ne + n system in the continuum. Experimental data on these excited states can shed light on the complex shell evolution among deformed nuclei near the drip line.

1.3 Motivation and purpose

^{31}Ne is a prime example of a deformed halo nucleus. It lies within a region of the nuclear chart characterized by an onset of shape coexistence, shell inversion, and deformation by virtue of core rotation. The strong single-particle nature of the even-Z nucleus with one neutron

($N = 21$) outside the $N = 20$ shell closure allows for streamlined theory calculations. The two protons outside the $Z = 8$ shell closure create a significant proton-neutron interaction influencing the nuclear properties and observables. Data regarding excited states of this nucleus can be useful for determining and describing systematic trends of nuclear existence and the location of the neutron drip line. This thesis examines the excited states of ^{31}Ne through the energy released in the one-neutron decay of ^{31}Ne* neutron-unbound excited states via the invariant mass spectroscopy method.

Chapter 2

Theoretical Background

The present work examines ^{31}Ne neutron-unbound excited states populated by the two-proton knockout ^{33}Mg(-2p). A decay energy was reconstructed from the detection of the one-neutron decay products. The method of invariant mass spectroscopy is employed to calculate the energy released in the one-neutron decay, called the decay energy. To create a theory-generated decay energy spectrum to compare with experimental data, both the two-proton knockout of ^{33}Mg populating the ^{31}Ne states as well as the following one-neutron decay to ^{30}Ne were calculated. This involves a combination of reaction and structure theory. Shell model theory provides the structure part of the knockout and decay calculations. R-Matrix methods were employed to calculate the two-proton knockout cross sections and provided a derivation of an appropriate lineshape to simulate a one-neutron decay from a neutron-unbound state.

2.1 Invariant mass spectroscopy

The direct measurement of neutron-unbound states is not possible because the neutron decay is, for all intents and purposes, immediate [6]. One way to study such short-lived systems is through the method of invariant mass spectroscopy. This section will consider the kinematics of a two-body decay where the decay energy quantity is derived based on the conservation

of four-momentum and the invariant mass quantity. The decay energy is defined as the amount of energy released in the decay in the center-of-mass frame. Figure 2.1 shows a simple schematic relevant to the considered decay. The following equations use units with $\hbar = c = 1$.

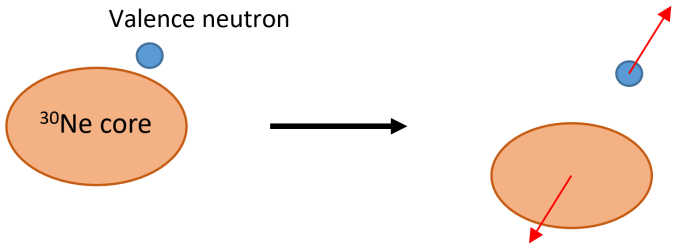

Figure 2.1: Schematic of the two-body decay $^{31}\mathrm{Ne} \rightarrow {}^{30}\mathrm{Ne} + n$.

Consider a two-body decay of the form

$$A \rightarrow B + C \tag{2.1}$$

The conservation of energy and momentum require the initial state four-momentum to be equal to the sum of the four-momenta of all final state particles:

$$P_A^\mu = P_B^\mu + P_C^\mu \tag{2.2}$$

The quantity $(P^\mu)^2$ is referred to as the "invariant mass" quantity and is Lorentz-invariant, meaning it can be evaluated in any frame of reference. Squaring equation 2.2 yields

$$(P_A^\mu)^2 = (P_B^\mu + P_C^\mu)^2 \tag{2.3}$$

Expanding the right side of this equation gives

$$(P_A^\mu)^2 = (P_B^\mu)^2 + (P_C^\mu)^2 + 2(P_B)^\mu(P_C)^\mu \tag{2.4}$$

The squared terms evaluated in their rest frames are the square of the rest mass of the relevant particle and the cross term is evaluated in the lab frame. Equation 2.4 becomes

$$m_A^2 = m_B^2 + m_C^2 + 2(E_B E_C - \vec{p}_B \cdot \vec{p}_C) \tag{2.5}$$

The energy difference between the initial nucleus and the decay products is referred to as the decay energy and is expressed as:

$$E_{decay} = m_A - (m_B + m_C) \tag{2.6}$$

Substituting m_A into equation 2.6 by taking the square root of equation 2.5 results in the decay energy expression:

$$E_{decay} = \sqrt{m_B^2 + m_C^2 + 2(E_B E_C - \vec{p_B} \cdot \vec{p_C})} - m_B - m_C \tag{2.7}$$

The decay energy quantity is now defined in terms of the rest masses, energies, and momentum vectors of the two particles in the final state. Particles B and C are interchangeable for this example. For the relevant single neutron decay, A represents the decaying nucleus ^{31}Ne, B represents the daughter nucleus ^{30}Ne, and C represents a neutron, and equation 2.7 becomes

$$E_{decay} = \sqrt{m_{^{30}\mathrm{Ne}}^2 + m_n^2 + 2(E_{^{30}\mathrm{Ne}}E_n - \vec{p}_{^{30}\mathrm{Ne}} \cdot \vec{p}_n)} - m_{^{30}\mathrm{Ne}} - m_n \tag{2.8}$$

2.2 Shell model calculations

The shell model is an example of a configuration-interaction (CI) approach to nuclear structure. A CI calculation requires the selection of a complete basis, the matrix elements of the Hamiltonian within this basis, and the resulting eigenvalues and eigenvectors of the matrix. The shell model described here follows the formalism from reference [2] performed with the NuShellX code [41]. The required associated wrapper codes bring in a prescribed Hamiltonian for which NuShellX finds the overlaps for the a^+ and a^+a^+ operators. These overlaps are then converted by the wrapper codes into spectroscopic factors and two-nucleon transfer amplitudes, respectively. The spectroscopic factor is interpreted as the "probability" that the overlap of the initial and final states looks like the single-particle assumed in the calculation. The two-nucleon transfer amplitudes inform two-nucleon removal cross section calculations. The present work involves overlaps for both the two-proton knockout cross sections populating states of ^{31}Ne, and the subsequent one-neutron decay from the neutron-unbound excited states. The $\langle n, ^{30}\mathrm{Ne}(J_f^\pi)|^{31}\mathrm{Ne}(J_i^\pi)\rangle$ overlaps provide spectroscopic factors for the one-neutron particle-unbound decay. The $\langle 2p, ^{31}\mathrm{Ne}(J_f^\pi)|^{33}\mathrm{Mg}(3/2^-)\rangle$ overlaps provide the two-nucleon transfer amplitudes used for the cross section calculation.

The NuShellX code uses a proton-neutron basis with a fixed total angular momentum J and isospin component T_z, where the J basis states are linear combinations of M states. The NuShellX basis states have the form

$$\mid B_i, J \rangle = \mid [p_i \otimes n_i] J \rangle \tag{2.9}$$

where p_i stands for labels (J_{p_i}, α_{p_i}), with the proton angular momentum J_{p_i}, and α_{p_i} all the other quantum numbers required for a complete basis; with similar labels for neutrons with n_i representing (J_{n_i}, α_{n_i}). The basis states can be partitioned, dictated by a model space, into a set of active shells and particle-hole configurations for each species of nucleon.

The Hamiltonian for configuration mixing of two states is a symmetric matrix with diagonal terms H_{11} and H_{22} where the matrix is organized $H_{11} < H_{22}$.... Considering interaction between the states introduces non-zero off-diagonal elements H_{12}. The generalized Hamiltonian can be expressed as

$$\begin{bmatrix} H_{11} & H_{12} \\ H_{21} & H_{22} \end{bmatrix}, \tag{2.10}$$

The addition of non-zero off-diagonal elements H_{12} introduces a small difference (δ) in the eigenvalues of the Hamiltonian. For this mixed configuration, the eigenvalues are

$$\begin{aligned} E_1 &= H_{11} - \delta \\ E_2 &= H_{22} + \delta \end{aligned} \tag{2.11}$$

where the subscripts 1(2) indicate eigenstates associated with the particle wavefunction $\Phi_{1(2)}$ for the case where $H_{12} = 0$, and where δ contains the dependence on H_{12}. As H_{12} grows, the states will be separated by an additional 2δ.

The Hamiltonian chosen for the present work was generated by the empirically-determined

FSU $spsdf-p$ cross-shell interaction [42] that has been successful at reproducing absolute binding energies for a large range of nuclei and the shell inversion associated with the $N = 20$ island of inversion. This interaction also describes two-particle two-hole cross-shell excitations and binding energies remarkably well even for nuclei which were not part of the fit. Therefore, it is appropriate for the nuclei relevant to this work, which lie in the region where this interaction excels at reproducing experimental data.

2.2.1 Spectroscopic factors

The spectroscopic factor with isospin dependence, in terms of the creation operator a^+, is

$$S(t_z) \equiv C^s S = |\langle TT_z|T'T'_z tt_z\rangle|^2 \frac{|\langle \Psi^A \omega JT||a^+||\Psi^{A-1}\omega' J'T'\rangle|^2}{(2J+1)(2T+1)}, \tag{2.12}$$

where ω is an additional quantum number, introduced when there is more than one state for a given J. The $|\langle TT_z|T'T'_z tt_z\rangle|$ is the isospin Clebsch-Gordan coefficient and the $(2J+1)$ quantity is conventionally associated with the heavier nucleus (A). The spectroscopic factor is used to calculate structure properties of the one-neutron decay of ^{31}Ne unbound excited states. The neutron decay widths for unbound states are obtained by using single-particle widths (for unbound states in one-body potentials) multiplied by the spectroscopic factors from configuration mixing.

2.2.2 Two-nucleon amplitudes

To model the population of ^{31}Ne states from ^{33}Mg(-2p), a combination of structure and reaction theory were used. The structure part is provided by the two-nucleon spectroscopic

amplitudes (TNAs) calculated with the $\langle 2p,^{31}(J_f^\pi)|^{33}(3/2^-)\rangle$ overlaps. The TNAs can be expressed in the tensor form of either the creation or destruction operators A^+ or $\tilde{A}$ respectively. The tensor form of the destruction operator for two particles is defined by

$$\tilde{A}(k_\alpha k_\beta J_0 M_0) = N_{12}[\tilde{a}_{k_\alpha} \otimes \tilde{a}_{k_\beta}]^{J_0}_{M_0} \tag{2.13}$$

with

$$N_{12} = \frac{1}{\sqrt{\left(1+\delta_{k_\alpha k_\beta}\right)}} \tag{2.14}$$

J_0 and M_0 are associated with the ground state of the projectile nucleus to which the two valence neutrons are coupled. In terms of the destruction operator representing a two-nucleon knockout, the TNAs are defined by

$$\mathrm{TNA}(\omega, \mathrm{J}, \omega', \mathrm{J}', \mathrm{k}_\alpha \mathrm{k}_\beta \mathrm{J}_0) = \frac{\langle (\mathrm{n}-2)\omega \mathrm{J}||\tilde{\mathrm{A}}(\mathrm{k}_\alpha \mathrm{k}_\beta \mathrm{J}_0)||\mathrm{n}\omega' \mathrm{J}'\rangle}{(2\mathrm{J}+1)} \tag{2.15}$$

In the present work the TNAs were used by the reaction theory to generate two-proton knockout cross sections for the reaction ^{33}Mg(-2p)^{31}Ne. The details of the reaction theory are discussed in the next section.

2.3 Reaction theory

Reaction theory using R-matrix methods were used to calculate the two-proton knockout cross sections into each state in ^{31}Ne and also provides a derivation of an appropriate

one-neutron decay lineshape. The R-Matrix formalism here is presented in Thompson and Nunes [43] and a simplified version of the derivation is outlined here.

2.3.1 R-matrix methods

There are two spatial regions to consider in the R-matrix formalism: the interior of the nucleus where particles interact via the strong force and the exterior, where they do not. These regions meet at a radius a, chosen such that this assumption holds true. The R-matrix basis states for the two regions are required to have fixed logarithmic derivatives at $R = a$.

The generalized R-matrix for a transition from the entrance channel α to the exit channel α' and pole p for the uncoupled case has elements

$$\mathbf{R}_{\alpha'\alpha}(E) \;=\; \sum_{p=1}^{P} \frac{\gamma_{p\alpha}\gamma_{p\alpha'}}{e_p \;-\; E} \tag{2.16}$$

where $\gamma_{p\alpha}$ are the reduced width amplitudes, e_p is the pole (resonance) energy, P is the number of poles, and E is the energy of the incident particle.

The scattering S matrix is then defined as:

$$\mathbf{S} \;=\; \frac{\mathbf{t}^{1/2}\mathbf{H}^{-} \;-\; a\mathbf{R}\mathbf{t}^{1/2}(\mathbf{H}^{-} \;-\; \beta\mathbf{H}^{-})}{\mathbf{t}^{1/2}\mathbf{H}^{+} \;-\; a\mathbf{R}\mathbf{t}^{1/2}(\mathbf{H}^{+} \;-\; \beta\mathbf{H}^{+})} \tag{2.17}$$

The diagonal matrix $\mathbf{t}$ has elements $t_\alpha = \hbar^2/2\mu$ and the diagonal $\mathbf{H}^{\pm}$ matrices have Hankel functions as the diagonal elements. β is the logarithmic derivative of the $\mathbf{R}$ matrix evaluated at the radius a. The Hankel function for a particular partial wave is composed of regular

and irregular Coulomb functions $H_l^{\pm} = G_l \pm iF_l$. The S matrix can be transformed into the symmetric matrix $\tilde{\mathbf{S}}$ using the transformation

$$\tilde{\mathbf{S}} = \mathbf{v}^{\frac{1}{2}}\mathbf{S}\mathbf{v}^{-\frac{1}{2}} \tag{2.18}$$

where $\mathbf{v}$ is a diagonal matrix with elements $v_\alpha = \hbar k_\alpha/\mu_\alpha$.

2.3.1.1 Two-proton knockout

The two-proton knockout is calculated using the eikonal, direct reaction model as outlined in[44]. The ^{33}Mg(-2p)^{31}Ne reaction is modeled as the sudden removal of two protons in a peripheral, high-speed reaction with the target nucleus, using the spectator-core approximation where the "core" nucleus ^{31}Ne interacts (at most) elastically with the target nucleus.

The projectile ^{33}Mg is treated as an anti-symmetrized $A+2$ nucleon system having a many-body wavefunction $\Psi(A,1,2)$ that describes the shell-model ground state. This state is associated with an angular momentum and isospin J_i and T_i, and respective projections M_i and τ_i. The ^{33}Mg projectile experiences the sudden removal of two protons upon collision with the target. The resulting ^{31}Ne* (A=31) residue is generally found in one of a number of final states $\Phi_{J_f M_f}(A)$ having spin J_f and isospin T_f with the respective projections M_f and τ_f.

The two protons removed from one or more partially-filled single-particle orbitals ϕ_j with spherical quantum numbers $n(ls)jm$, are assumed to couple to states with intermediate total angular momentum I, μ and isospin T, τ. The overlap functions relative to a specific core state f is a sum over a number of two-particle configuration contributions, expressed as

$$\begin{aligned}\Psi^{(f)}_{J_iM_iT_i\tau_i} &\equiv \langle \Phi_{J_fM_fT_f\tau_f}(A)|\Psi_{J_iM_iT_i\tau_i}(A,1,2)\rangle \\ &= \sum_{I\mu\alpha} C_\alpha^{J_iJ_fIT_iT_fT}(I\mu J_fM_f|J_iM_i)(T\tau T_f\tau_f|T_i\tau_i)[\overline{\phi_{j_1}(1)\otimes\phi_{j_2}(2)}]^{T\tau}_{I\mu}\end{aligned} \tag{2.19}$$

Where the $[\overline{\phi_{j_1}(1)\otimes\phi_{j_2}(2)}]^{T\tau}_{I\mu}$ are the normalized antisymmetrized two-nucleon wavefunctions and $C_\alpha^{J_iJ_fIT_iT_fT}$ are the shell-model two-nucleon amplitudes carrying the structure information, discussed in section 2.2.2.

In the eikonal direct reaction theory, the interaction of the two nucleons (labeled 1 and 2) and the A-body residue f with the target are described by their elastic $\mathbf{S}$-matrices $\mathbf{S}_i$, which are functions of their individual impact parameters b_i and assumed to be spin-independent. The absorption cross section is the projectile ground-state expectation value

$$\sigma_{abs} = \frac{1}{2J_i+1}\sum_{M_i}\int d\boldsymbol{b}\langle\Psi_{J_iM_i}|[1-|\mathbf{S}_f\mathbf{S}_1\mathbf{S}_2|^2]|\Psi_{J_iM_i}\rangle \tag{2.20}$$

2.3.1.2 One-neutron decay lineshape

The decay of an unbound resonant state is characterized by a central energy and width. Extracting these quantities from the experimental spectrum involves de-convolution of resolution and acceptance effects. A decay line shape specified by an energy and width can instead be simulated and subjected to the experimental resolutions and acceptances. This method allows for a direct fit to the experimental data to extract the energy and width of the decay. This section will use R-matrix reaction theory to derive an energy-dependent Breit-Wigner lineshape which is used to simulate the desired neutron-unbound decay.

The single neutron decay is described in R-matrix theory as an inelastic scattering process with different entrance and exit channels denoted α and α'. This method allows a derivation of an appropriate line shape which describes a resonant decay and is directly fit to the data to extract a pole energy and width. Defined in section 2.3.1, the symmetric **S**-matrix $\tilde{\mathbf{S}}$ can be written:

$$\tilde{\mathbf{S}} \;=\; \Omega[1 \;+\; 2iP^{\frac{1}{2}}(1 \;-\; a\mathbf{R}L)^{-1}\mathbf{R}P^{\frac{1}{2}}]\Omega, \tag{2.21}$$

where Ω is the matrix with diagonal elements $e^{i\phi\alpha}$, and ϕ_α are the hard-angle phase shifts. For the two-channel case relevant to this work, the $\tilde{\mathbf{S}}$ elements are

$$\tilde{\mathbf{S}}_{\alpha'\alpha} \;=\; e^{i\phi\alpha}\left[\delta_{\alpha'\alpha} \;+\; \frac{2iP_\alpha^{\frac{1}{2}}\gamma_\alpha\gamma_{\alpha'}P_{\alpha'}^{\frac{1}{2}}}{(e_p \;-\; E)(1 \;-\; aR_{11}L_1 \;-\; aR_{22}L_2)}\right]e^{i\phi\alpha'} \tag{2.22}$$

which looks like an isolated Breit-Wigner resonance with a total formal width $\Gamma_{tot} = 2\gamma_1^2P_1 + 2\gamma_2^2P_2 = \Gamma_1 + \Gamma_2$. The total cross section for scattering to channel α from α_i is

$$\begin{aligned}\sigma_{\alpha\alpha_i}(J^\pi_{tot}) &= \frac{\pi}{k_i^2}g_{J_{tot}}|\tilde{\mathbf{S}}_{\alpha\alpha_i}|^2 \\ &= \frac{\pi}{k_i^2}g_{J_{tot}}\frac{\Gamma_\alpha\Gamma_{\alpha_i}}{(E - E_r^f)^2 + \Gamma_{tot}^2/4}\end{aligned} \tag{2.23}$$

which is the form of an isolated Breit-Wigner resonance with a strong peak at $E \approx E_r^f$ and a full-width half-max Γ_{tot}. E_r^f is the formal resonance energy, defined by

$$E_r^f \equiv e_p \;-\; \gamma_1^2\mathbf{S}_1^0 \;-\; \gamma_2^2\mathbf{S}_2^0 \tag{2.24}$$

Note that the formal resonance energy is shifted from the pole energy e_p due to channel-coupling. Substituting the elements of the symmetric S-matrix from equation 2.22 yields

$$\sigma_{\alpha\alpha'} \;=\; \frac{\pi}{k_{\alpha}{}^2}\left(\frac{2J\;+\;1}{(2I_p\;+\;1)(2I_t\;+\;1)}\right)\left[\frac{\Gamma_\alpha\Gamma_{\alpha'}}{(E\;-\;E_r^f)^2\;+\;\frac{1}{4}\Gamma^2}\right] \tag{2.25}$$

From equation 2.24 in which the formal resonance energy depends on the coupling between reaction channels, we can define an "energy-dependent" lineshape. The cross section can now be written in terms of the pole energy and total width and takes the form of an "energy-dependent" Breit-Wigner distribution with a strong peak at E_r^f and a full-width at half-max (FWHM) of Γ. This function is also called an "asymmetric" Breit-Wigner for $l > 0$.

$$\sigma(E; e_p, \Gamma_l) \;=\; A\frac{\Gamma_l}{\big(e_p\;-\;E\;+\Delta_l(E; e_p, \Gamma_l)\big)^2\;+\;\frac{1}{4}\Gamma_l^2} \tag{2.26}$$

where A is a proportionality constant. This line shape was used to simulate resonances with $l > 0$ with pole energy and total width parameters $_p$ and Γ_l respectively . After being propagated through the simulated experimental setup, these resonant lineshapes are fit directly to the experimental data.

Chapter 3

Experimental Techniques

The experiment to study ^{31}Ne neutron-unbound excited states took place at the National Superconducting Cyclotron Laboratory (NSCL) in November of 2017. The Coupled Cyclotron Facility (CCF) [45] and the A1900 Fragment Separator [46] produced a secondary beam of ^{33}Mg via fast fragmentation [47] of a ^{48}Ca primary beam. The experimental setup included a segmented target, the MoNA (Modular Neutron Array) and LISA (Large multi-Institutional Scintillating Array) arrays, and the Sweeper superconducting dipole magnet with its suite of charged particle detectors. This chapter details the beam production and detectors utilized.

3.1 Beam production

In this work, the ^{33}Mg secondary beam was produced and delivered by the CCF [45] and A1900 fragment separator [46] seen in Figure 3.1. An electron-cyclotron resonance (ECR) ion source produced $^{48}Ca^{8+}$ ions which were extracted and accelerated through the K500 cyclotron to roughly 12 MeV/u. The beam was then sent to the K1200 cyclotron where the ions were stripped of their remaining electrons and accelerated to 140 MeV/u. The fully ionized $^{48}Ca^{20+}$ ions were then accelerated by the K1200 cyclotron to an energy of 140 MeV/u. The ^{48}Ca ion beam then impinged on an 846 mg/cm^2 thick beryllium pro-

duction target, undergoing a fragmentation reaction which created a diverse assortment of nuclei called "fragments".

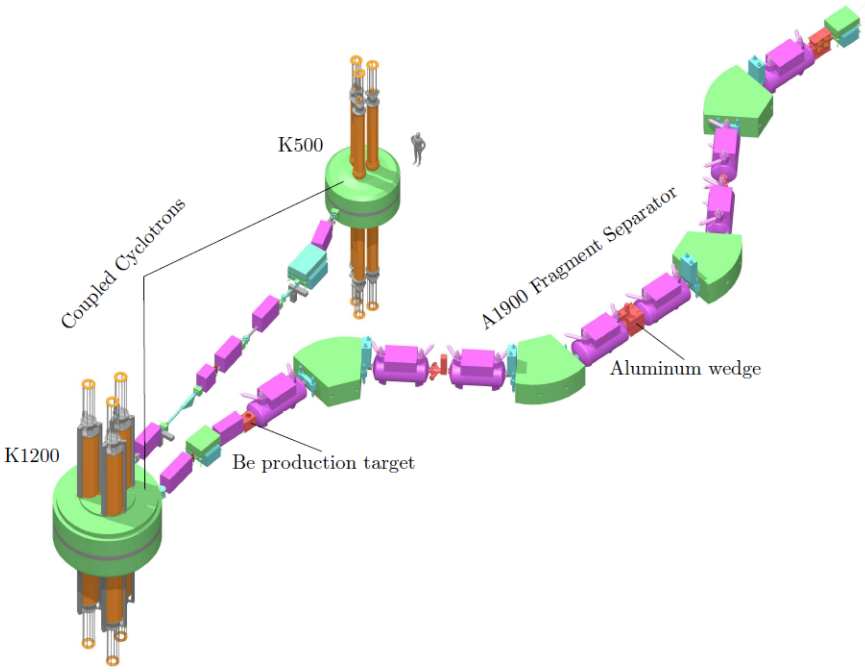

Figure 3.1: The layout of the NSCL coupled cyclotrons and the A1900 fragment separator utilized in this work.

To isolate the desired secondary beam of ^{33}Mg from the rest of the fragments, the A1900 Fragment Separator was utilized. The A1900 is a magnetic separator consisting of four main dipoles and eight quadrupole triplets. The dipole magnetic fields were tuned to the magnetic rigidity (B$\rho = p/q$) of the ^{33}Mg fragment of interest. The fragments followed trajectories through the magnet based on their magnetic rigidity (Bρ) and an adjustable slit was used to remove particles having sufficiently different rigidity. To assist in fragment separation, a 736 mg/cm^2 aluminum wedge was included in the middle of the A1900 Fragment Separator. Because the energy loss through the aluminum wedge is dependent on the atomic number (Z), charged fragments with similar $B\rho$ were separated in the magnets downstream. A second set of slits were used after the wedge to remove more particles with incompatible $B\rho$ using a

momentum acceptance of 0.01%. After fragment separation, the ^{33}Mg secondary beam was 57% pure, with an energy of 88.8 ± 0.17 MeV/nucleon corresponding to a magnetic rigidity of 3.82 ± 0.038 Tm. The secondary beam passed through a timing scintillator at the A1900 focal plane before being transmitted to the experimental area, shown in Figure 3.2, where it passed through another timing scintillator and then entered the segmented target, which contained four silicon wafer detectors and three beryllium targets in alternating order. The beam then traveled through a large-gap dipole magnet and into a suite of charged particle detectors. The details of these detectors are discussed in the following sections.

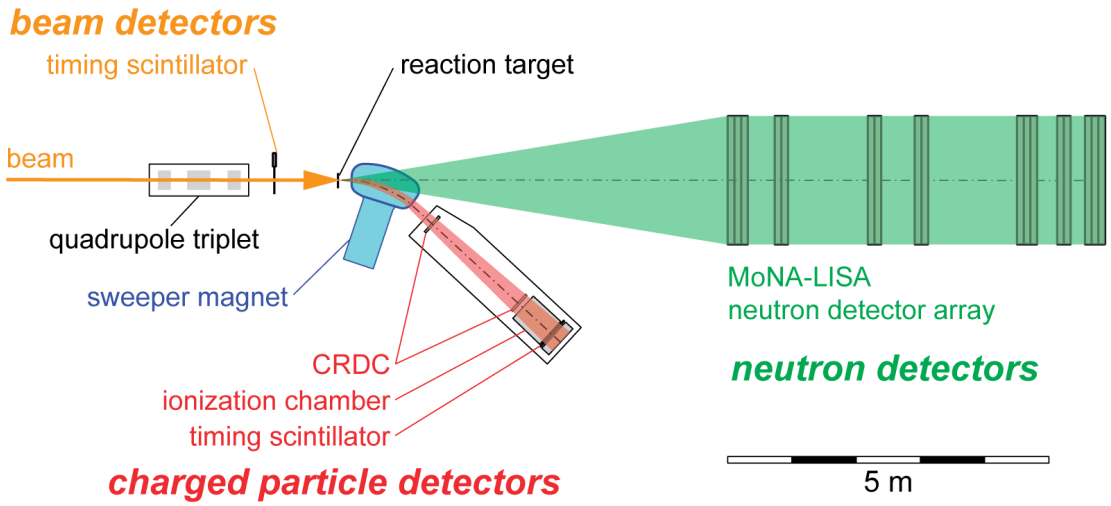

Figure 3.2: Overhead view of the detector configuration for the performed experiment, which was located in the N2 experimental vault at the NSCL.

3.2 A1900 and Target scintillators

The time-of-flight of the secondary beam was measured by two plastic timing scintillators upstream from our reaction target in the N2 experimental vault. The first was the A1900 extended focal plane (XFP) plastic timing scintillator 10.9 m upstream from the reaction target, made of 144 μm thick BC-400 material and coupled to a photo-multiplier tube (PMT).

The second scintillator was the Target scintillator, 1.03 m upstream of the reaction target, made of 420 μm thick BC-404 material and coupled to a PMT.

3.3 Segmented target

The secondary beam then traveled to the Segmented Target, an array of four position-sensitive silicon detectors and three target holder positions in an alternating order as depicted in Figure 3.3 [48]. The group of four silicon detectors and the group of three targets are located on independent drives and each group can be individually inserted in the beam line. The beam passed through the segmented target components inserted in the beam line, losing energy in each component and potentially fragmenting in the beryllium targets or silicon detectors.

3.3.1 Silicon detectors and beryllium targets

The silicon detectors, phosphorus-doped n-type silicon wafers, with dimensions 62 mm $\times$ 62 mm and $\sim$140μm thick, had four corner signals and an anode signal. The corner signals were taken from the detector face, a boron-implanted p-type resistive anode layer with a border of resistive ion-implanted strips that are 0.5 mm wide. The anode signal was taken from the back face and measured the energy deposited independently of the corners.

For this experiment, three beryllium targets each approximately 1,076 μm thick were used. Prior to the experiment, calculations were performed to select the target thicknesses which optimized both the production rate of the desired nucleus and the decay energy resolution. Target thicknesses were measured using calipers, with a measurement uncertainty of ± 4 μm (± 0.7 mg/cm^2) Be. The silicon detector thicknesses are reported by the manufacturer

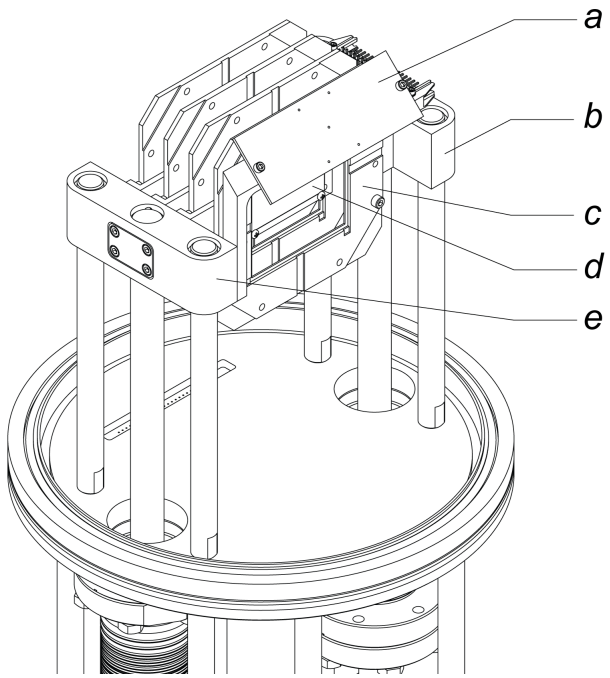

Figure 3.3: Schematic of the segmented target utilized in the experiment. The labels illustrate the locations of: (a) the beam viewer plate used during beam tuning, (b) the detector mounting base, (c) the frames for the silicon detectors, (d) one of three beryllium targets located between each pair of silicon detectors, and (e) the target mounting base. The target and detector mounts are on independent pneumatic drives.

with uncertainties of ± 1 μm (± 0.2 mg/cm^2) Si. The thicknesses of the beryllium targets and the silicon detectors used in this work are listed in Table 3.1.

Table 3.1: Silicon detector and beryllium target thicknesses used in the Segmented Target.

Segment	Thickness [μm]	Areal Density [mg/cm^2]
Si 0	140	32.5
Be 1	1076	199.1
Si 1	135	31.3
Be 2	1076	199.1
Si 2	138	32.0
Be 3	1075	198.9
Si 3	142	33.0

3.3.2 Segmented target readout and electronics

Each silicon detector had four corner signals and one anode signal, for a total of 20 signals for the assembly. Each anode signal was sent to a preamplifier that was characterized by an 0.05 μs rise time and 500 μs fall time with a typical output signal of 30 mV when a 5.5 MeV α source was placed 7.1 m in front of the detector in vacuum [49]. The signals are then sent to to a Tennelec 241S shaping amplifier with a shaping time of 6 μs before being sent to an ADC. The corner signals were each sent to one of 16 Mesytec MMPR1 preamplifiers and then to a single Mesytec MSCF-16 shaping amplifier. These are separate (from the anode) preamplifier and shaping amplifier, having a shaping time of 2 μs for all corner channels. Both anode and corner signals are then sent to the same Mesytec MADC-32 ADC. Figure 3.4 shows the electronics diagram for the segmented target signals.

3.4 Sweeper magnet

The beam continued toward the Sweeper magnet, a large-gap (14 cm) superconducting dipole magnet with a bending angle of 43.3 degrees and a radius of 1 meter with a maximum magnetic rigidity of 4 Tm. The field was controlled by setting the current in the superconducting

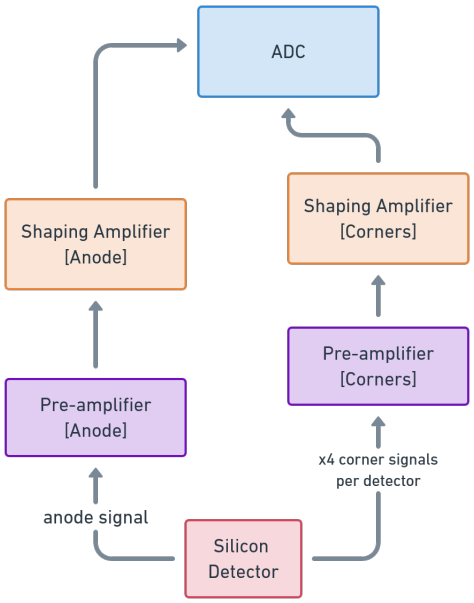

Figure 3.4: Segmented Target electronics diagram for one silicon detector. The anode and four corner signals were sent to separate preamplifiers and shaping amplifiers before being sent to the same ADC.

coils and was monitored using a Hall probe. To center the trajectory of the ^{33}Mg secondary beam through the magnet, the current was set to 345 Amps (Bρ = 3.73 Tm). For the ^{30}Ne fragments of interest in the production setting, the current was set to 337 Amps (Bρ = 3.67 Tm).

All charged particles from the fragmentation reactions (and any un-reacted beam) were "swept" off their trajectory toward the charged particle detectors as they passed through the magnetic dipole field. The neutrons continued through the 14 cm vertical gap of the Sweeper magnet and through the air toward the MoNA-LISA neutron detectors which are discussed in Section 3.6.

3.5 Sweeper detectors

A variety of charged particle detectors were used along the path of the beam and the associated charged fragments. The first three were the A1900 and Target scintillators, which were described in Section 3.2 and the Segmented Target, discussed in Section 3.3. The remainder of the charged particle detectors were contained in a large vacuum box directly following the Sweeper Magnet, referred to as the Sweeper detectors. These consisted of two cathode readout drift chambers (CRDCs) used to measure the position of the charged particles, an ion chamber to measure the energy loss, and a "Thin" plastic timing scintillator to measure the outgoing time-of-flight for the charged fragments.

3.5.1 Cathode Readout Drift Chambers

There are two CRDCs placed approximately 1.55 m apart in the Sweeper detector box that individually measure the horizontal (x) and vertical (y) position of a charged fragment. The angle of a fragment detected in both CRDCs is deduced from this position information. The fragment's momentum at the reaction vertex, necessary for calculating the decay energy, is reconstructed with position and angle information provided by the CRDCs.

The CRDCs are gas-filled detectors with a 30 cm $\times$ 30 cm active area perpendicular to the incoming beam axis. The volume is filled with a 1:4 mixture of isobutane and CF_4. Ion pairs, created by charged particles interacting with the gas, drift apart due to a 1,000 V electric field applied vertically between a plate at the top and a Frisch grid near the bottom of the detector. An anode wire and 128 aluminum pads each 2.54 mm wide are laid out in the horizontal (x) direction underneath the Frisch grid. When the electron avalanche reaches the anode, it induces charge on the cathode pads and the distribution of the deposited charge

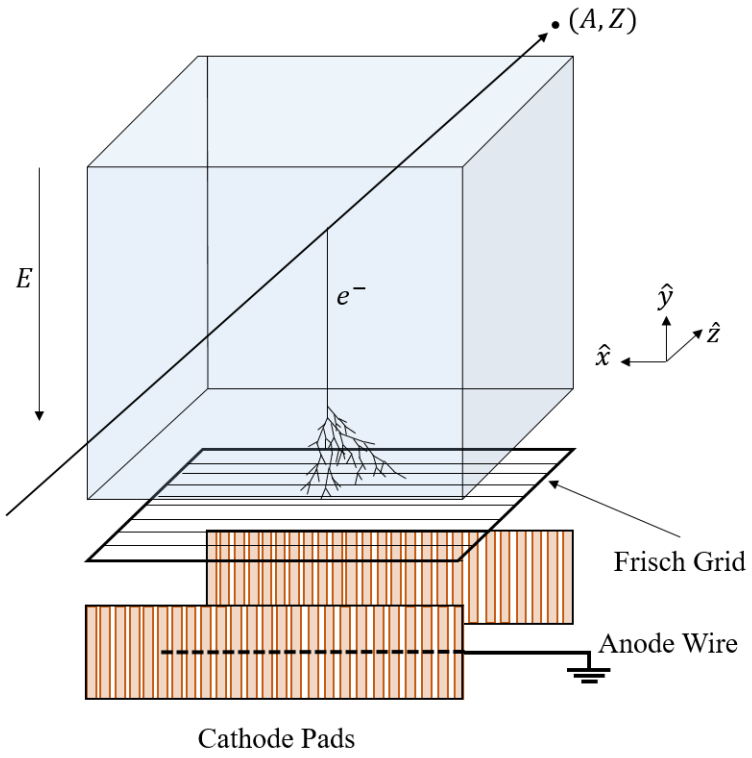

Figure 3.5: CRDC schematic with the z dimension expanded. The electron avalanche does not occur until the electron reaches the Frisch grid but is shown for illustrative purposes.

is fit to extract the x-position of the fragment. The y-position is determined by the drift time of the electron through the applied electric field.

3.5.2 Ionization chamber

The ionization chamber is a gas-filled detector with an active volume 40 cm × 40 cm × 65 cm. The front window of the chamber measured 30 cm × 30 cm perpendicular to the beam axis to match the dimension of the CRDC2 immediately preceding it, while the rear window measured 40 cm × 40 cm to allow for dispersion. The detector volume was filled with P-10 gas (90% argon, 10% methane) at 300 Torr. As particles passed through the ion chamber they created ion pairs that drifted apart, subject to a drift voltage of 10 V applied between a large plate at the top and 16 collection pads at the bottom of the detector. The pads

were discretized in the direction of the beam path (z) and extended along the horizontal (x) direction perpendicular to the beam. Energy loss through the ion chamber was determined using the sum of the charge collected on all pads.

3.5.3 Thin scintillator

A "Thin" timing scintillator contained in the Sweeper detector vacuum box was the last detector along the charged particle path. The Thin scintillator, made of EJ-204 material, is shown in Figure 3.6. It had dimensions 55 cm × 55 cm perpendicular to the beam axis with an active area of 40 cm × 40 cm, and a thickness of 5 mm. Four trapezoidal light guides were attached, two at the top and two at the bottom as shown in Figure 3.6, each coupled to a PMT. This scintillator provided a trigger for the data acquisition upon detection of a charged fragment and measures time-of-flight relative to the target or XFP timing detector.

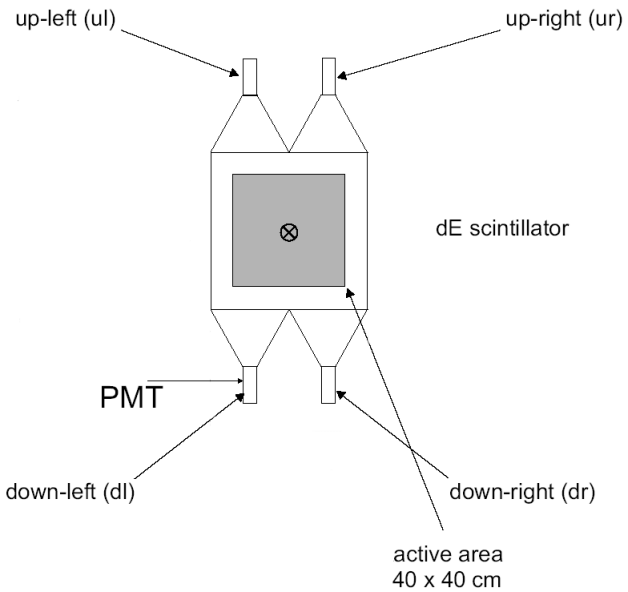

Figure 3.6: Schematic drawing of the Thin scintillator which measures outgoing time-of-flight for the charged fragments. The upper-left (ul) PMT provides the system trigger for the data acquisition.

3.6 MoNA-LISA

The Modular Neutron Array (MoNA) and the Large multi-Institutional Scintillating Array (LISA) [50] were utilized in this experiment to measure the three-dimensional neutron hit position as well as the time-of-flight for the detected neutrons. Both are large neutron detectors of similar modular design and can be arranged in a variety of configurations.

MoNA and LISA were comprised of 128 and 144 plastic scintillator bars respectively, each bar measuring 2 m $\times$ 10 cm $\times$ 10 cm. The 2 m length of the bars extend along the horizontal (x) direction. They were organized into 8 layers for MoNA and 9 layers for LISA, and each layer contained a vertical stack of 16 bars. MoNA layers were labeled A through H and LISA layers were labeled J through R. The two arrays were separated into 3 groups of layers referred to as "tables," displayed in Figure 3.7. The front of the first table in the beam path was LISA II (layers N-R), 596 cm from the target position, followed by LISA I (layers J-M), 812 cm from the target. All MoNA layers A-H comprised the last table, 1041 cm from the target.

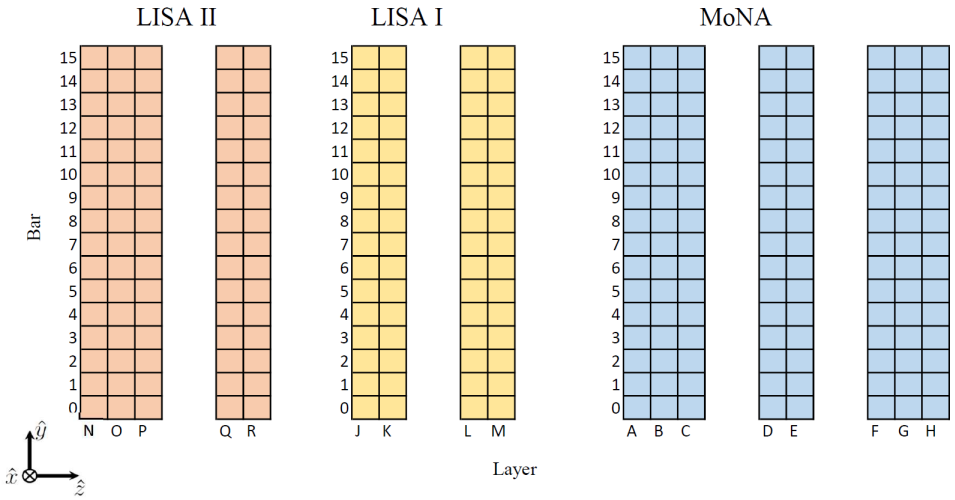

Figure 3.7: MoNA-LISA experimental setup orientation and grouping (spacing between layer groups not to scale) viewed from the side. Neutrons travel left to right through the array.

The MoNA bars are made of BC-408 and the LISA bars of EJ-200 material, each with a light attenuation length greater than 3.8 m which are physically and chemically equivalent. The bars were individually wrapped with reflective material to reduce light leaks and with black plastic to avoid introducing ambient light. On either end of each 2 m scintillator bar was a light guide coupled to a photo-multiplier tube (PMT). MoNA utilized Photonis XP2262/B PMTs and LISA utilized Hamamatsu R329-02 PMTs.

Neutrons undergo a nuclear interaction within the plastic detector volume which produced scintillation light. The neutron-to-hydrogen mass ratio is much larger than the neutron-to-carbon mass ratio so neutron-proton interactions produced more scintillation light. The recoiling protons deposited energy in the plastic, causing light to be produced that propagates to both ends of the bar and is detected by the PMTs on either end. The PMTs each had an anode signal for timing information, used in the reconstruction of the neutron four-momentum and a dynode signal for the charge collected which assisted in neutron event selection.

The time difference between the left and right PMT signals is used to determine the horizontal (x) position of a neutron hit along the bar. The average of the two timing signals is used to determine the time-of-flight from the target position to the neutron hit position. The segmentation in the vertical (y) direction and beam axis (z) direction allows determination of a 3-dimensional location for the neutron hit. Under the condition that the neutrons originate from the center of the reaction target, this provides all the necessary information for the reconstruction of the neutron four-momentum at that location.

3.7 Electronics and Data Acquisition System

The electronics and data acquisition (DAQ) for the MoNA-LISA and Sweeper systems has been described and characterized in previous works [51, 52, 53, 49, 54]. An overview will be summarized here with settings specific to this work.

3.7.1 Data acquisition hardware

There are three subsystems of the data acquisition that operate independently: one for MoNA, one for LISA, and one for the Sweeper detectors. They are connected through a logic system handled by Xilinx Logic Modules (XLMs) with field-programmable gate arrays (FPGAs) which is split into three "levels". Levels 1 and 2 determine whether a MoNA-LISA event is valid. Level 3 controls the coincidence between MoNA-LISA and the Sweeper and is responsible for generating and distributing the system trigger and a timestamp for each registered event to all three individual subsystems.

For this experiment, the data acquisition ran in "Sweeper singles" mode, meaning the Level 3 logic generated a system trigger from the channel 0 (upper left) PMT of the Thin timing scintillator in the Sweeper subsystem. This trigger opens a coincidence gate for a signal from a hit in MoNA-LISA. Regardless of the validity of an event in MoNA-LISA, the Sweeper subsystem is read out. If MoNA-LISA registers a hit without the system trigger, Level 3 will be set to "busy" and the MoNA-LISA acquisition is cleared. A schematic of the MoNA, LISA, and Sweeper subsystems is shown in Figure 3.8.

The two independent subsystems of MoNA and LISA have electronics setups identical in design. Each of the PMTs for each MoNA-LISA bar had an anode signal used for timing and a dynode signal used to measure the light deposited. Each PMT anode signal was sent

to a constant fraction discriminator (CFD). A copy of this signal was sent to both a time-to-digital converter (TDC) and an XLM for the subsystem trigger logic. The CFD provided the start signal for the TDC and the stop signal was generated by the Level 3 logic. Each PMT dynode signal is sent to a charge-to-digital converter (QDC) module that integrated the charge collected to determine the amount of scintillation light detected. The time and charge signals from the TDC and QDC respectively were read out by the DAQ computer. A schematic of the MoNA-LISA electronics is shown in Figure 3.9.

The Sweeper subsystem detectors for this experiment included three timing scintillators, four segmented-target silicon detectors, two CRDCs, and an ion chamber. Each of the three timing scintillators (A1900 XFP scintillator, Target scintillator, and Thin scintillator) signals were sent to CFDs and TDCs for timing information. In addition, the channel 0 (top left PMT) signal of the Thin scintillator was sent to the Level 3 logic, providing the system trigger. The PMT charge signals for the Target and Thin scintillators were separately processed by an ADC. The CRDC anode signals were sent to a time-to-amplitude converter (TAC) and then to an analog-to-digital converter (ADC). The CRDC pad signals were sampled by Front-End-Electronics (FEEs) and sent to an XLM for readout. The individual ion chamber pad signals were sent to a shaping amplifier and to an ADC. The segmented target electronics have been discussed in Section 3.3.

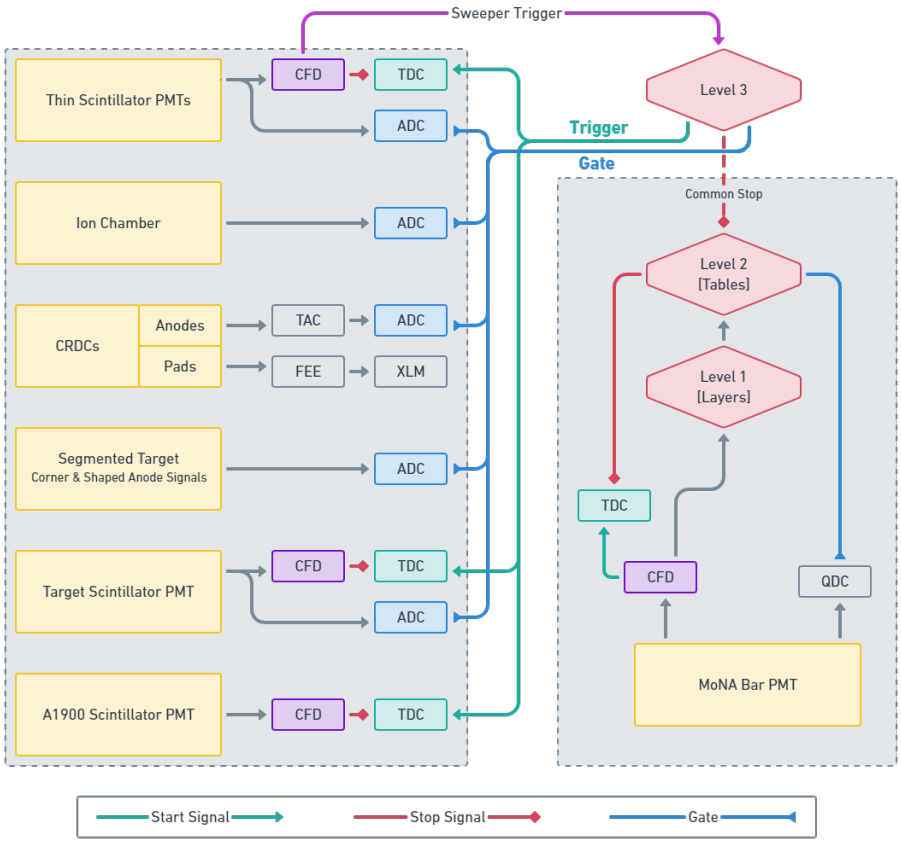

Figure 3.8: Level 3 data acquisition electronics schematic for this experiment.

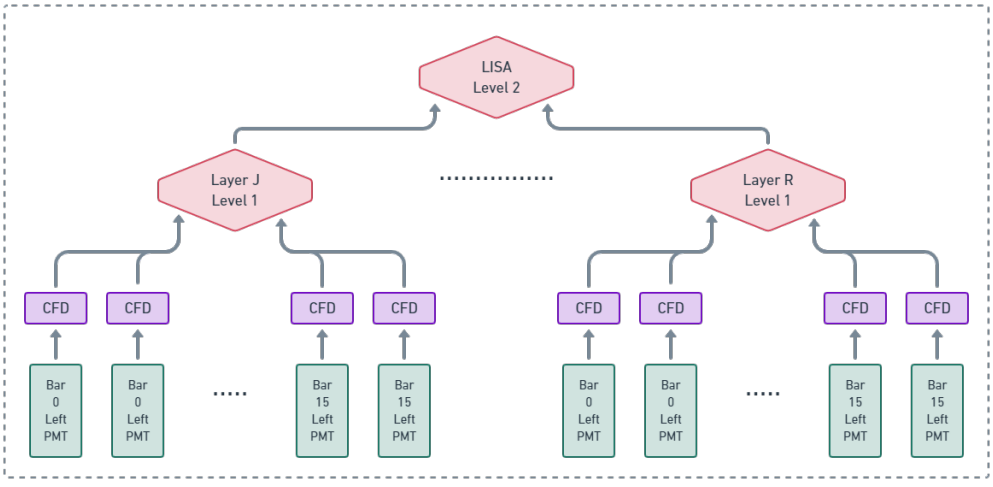

Figure 3.9: LISA data acquisition electronics schematic. MoNA uses an identical setup.

3.7.2 Data acquisition software

The MoNA, LISA, and Sweeper subsystems had individual readout programs for this experiment that used the NSCLDAQ version 11.2 run on a dedicated DAQ computer for each device (spdaq40 for MoNA, spdaq42 for LISA, and spdaq34 for the Sweeper). Each had its own ring buffer, a data structure having a fixed size with the pointers "*put*" and "*get*". Each ring buffer had a single producer (MoNA, LISA, or Sweeper) and multiple consumers, and behaved in a first-in-first-out manner. Additional details can be found in the NSCLDAQ documentation [55]. A producer stores data in a ring buffer with the *put* pointer, and a consumer can read the data in the ring buffer with the *get* pointer. After use, the respective pointer is incremented. The ring buffer is defined as full when incrementing *put* will give the location of *get* and empty if *put* and *get* are at the same location.

When the MoNA, LISA, and Sweeper subsystems operated simultaneously, a "Master" readout was utilized that synchronized all the independent readouts and was the producer for the Master ring buffer called the "built" ring. Events were built in the Master readout by combining ring items from each subsystem using 64-bit timestamps. A consumer of this "built ring" used the *get* pointer to write the data to a binary file, which was unpacked offline into a ROOT file for calibration and analysis. Other consumers for the ring buffers include individual TclTK scripts used by SpecTcl [56] for each subsystem which allowed for visualization and analysis of data as it came in during the course of the experiment. A DAQ software diagram showing the ring buffers and detector subsystems is shown in Figure 3.10.

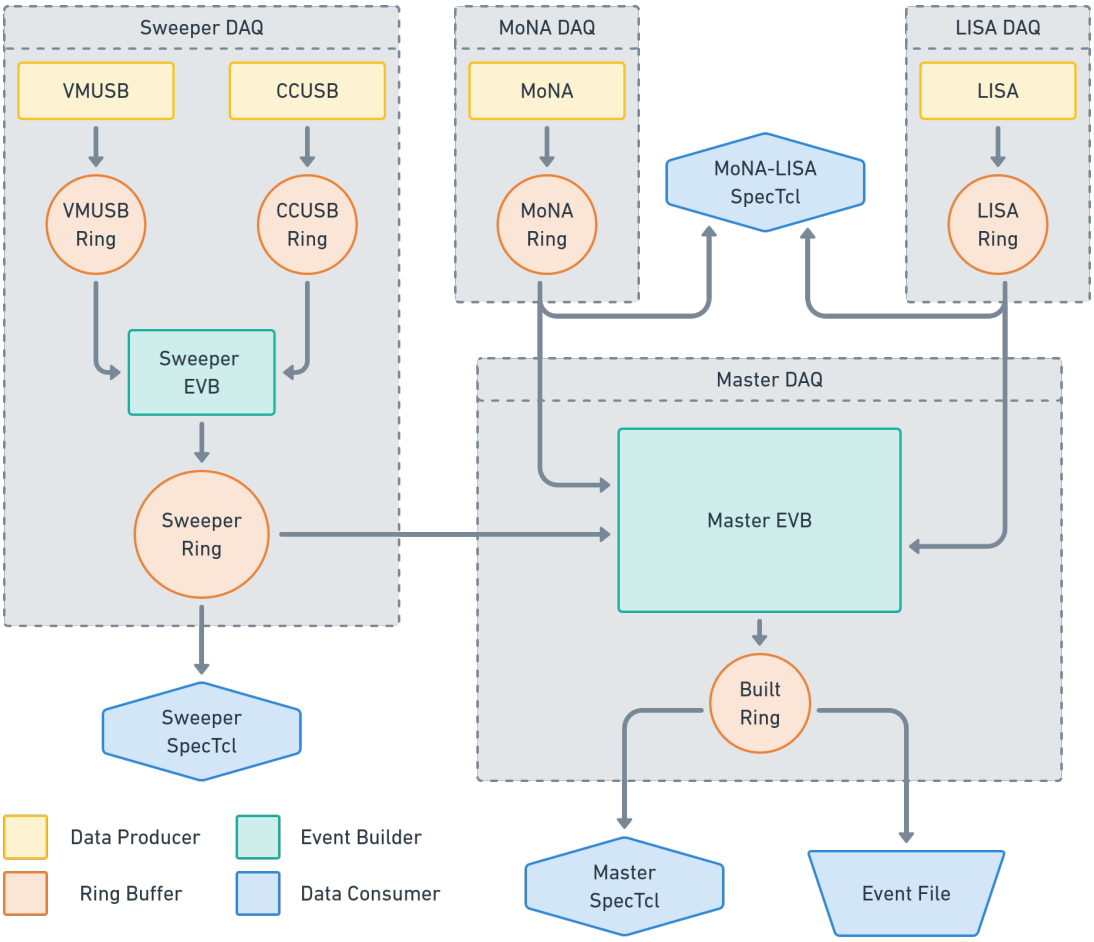

Figure 3.10: The DAQ software schematic. Yellow denotes a data producer (MoNA, LISA, and Sweeper subsystems), orange denotes a ring buffer, green denotes an event builder (EVB) which builds events from one or more ring buffers using a 64-bit timestamp, and blue denotes a data consumer. The sweeper producers VMUSB and CCUSB refer to crate controllers for VME and CAMAC crates respectively.

Chapter 4

Data Analysis

4.1 Charged particle detector calibrations

4.1.1 Cathode Readout Drift Chambers

The cathode readout drift chambers (CRDCs) are responsible for detecting the positions and angles of the incoming fragments as discussed in section 3.5.1. Each CRDC provides an x- and y-position for each fragment event, the combination of both detector positions allows extraction of the angles of the fragments relative to the beam axis in both horizontal and vertical directions. In order to obtain accurate position information the pad responses are normalized and a position calibration is performed.

4.1.1.1 CRDC pedestal calibration

Each cathode readout drift chamber has 128 charge collection pads. When the detectors and associated electronic modules are powered, there is a small current that is induced and processed throughout all modules. This electronic noise, which should be the same for each channel, shows up in the energy spectrum of the CRDC pads. This feature is called a "pedestal" and needs to be subtracted for all CRDC pads so their minimum charge collected is the same. An offline data acquisition with the CRDCs turned on is used to populate

these pedestals, and they are fit with a Gaussian function on each collection pad. The mean value of this fit is then subtracted for the respective pad. Some CRDC pads show spectra indicating poor charge collection and are removed from the analysis, listed in Table 4.1. The result of the CRDC pedestal calibration is shown in Fig. 4.1.

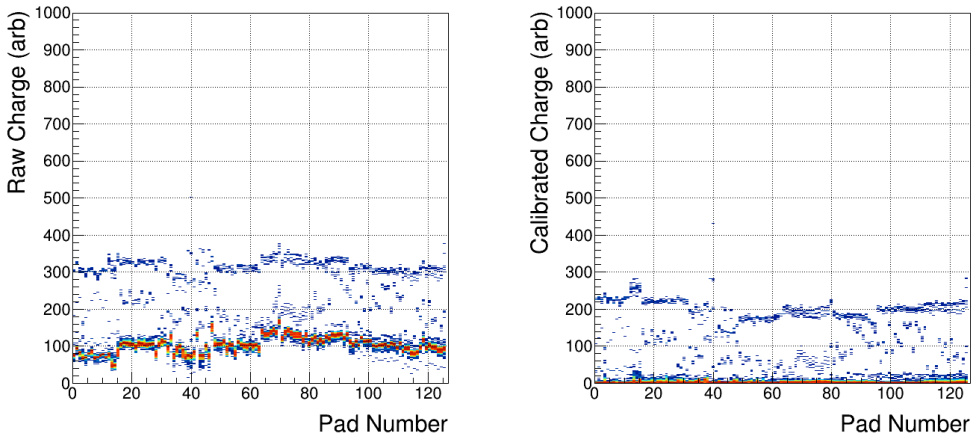

Figure 4.1: CRDC pedestal response calibration. Red regions indicate the highest number of counts. The Un-calibrated (raw) spectrum is on the left and the calibrated spectrum is on the right.

4.1.1.2 CRDC gainmatch

The deposited energy is a function of the incident ion proton number Z, distributed on a number of neighboring pads in the region of the particle interaction. This distribution is fit with a Gaussian function to extract the horizontal (x) position. The response of each pad in each CRDC needs to be matched such that each pad has the same response when it detects the same amount of energy. To do this, a "sweep" run is performed during the experiment. The ^{33}Mg beam is continuously moved across the face of the CRDCs in the x-direction, using a varying magnetic field produced by the Sweeper magnet. This aims to illuminate as many of the pads as possible. Un-reacted beam events are selected to isolate

particles with the same Z. The charge collected by each pad is then normalized to a chosen reference pad near the center of the array using a linear calibration. Some CRDC pads show spectra indicating poor charge collection or have little charge collection, because the cone of the beam is not large enough to cover the face of the detector, and they are removed from the analysis, listed in Table 4.1. Fig. 4.2 shows the gainmatch performed on CRDC2. An identical process was used to gainmatch CRDC1.

Table 4.1: Pads removed from analysis for CRDC1 and CRDC2 due to charge collection spectrum features.

CRDC 1	CRDC 2
1-40	1-13
80	127
96-127	

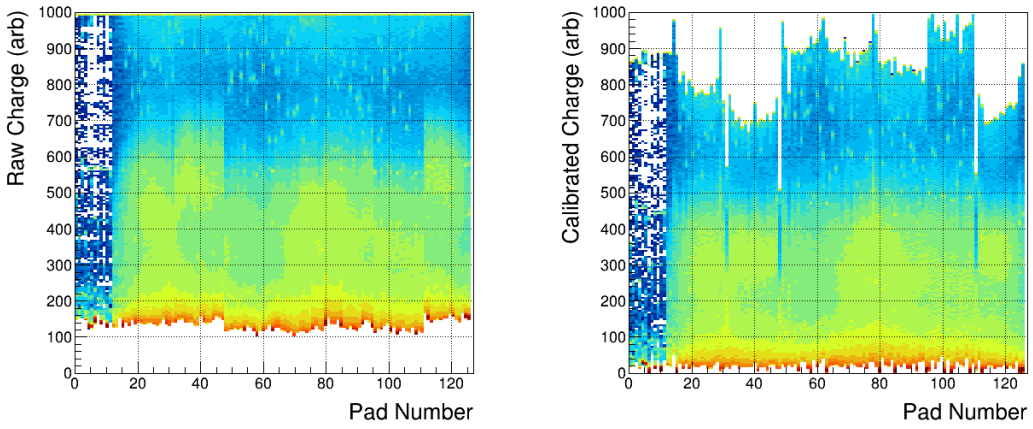

Figure 4.2: CRDC gainmatch. Events shown correspond tothe un-reacted beam with $Z = 12$. The un-calibrated (raw) spectrum is on the left and the calibrated spectrum is on the right.

4.1.1.3 CRDC time drift

The vertical (y) positions of the detected fragments in the CRDCs are measured using the drift time across an electric field in a gas volume. The measurement can drift over time due to

fluctuations in the applied electric fields and gas pressure and temperature fluctuations. To account for this, a drift correction is performed through a linear calibration which normalizes the response of the CRDC as a function of time over the course of the experiment. Figure 4.3 shows the measured drift time signal as a function of time for both CRDC1 and CRDC2. The run number is a measure of time: each run is one hour long (two hours for runs 1076 and later) and the data was gathered over the course of one week.

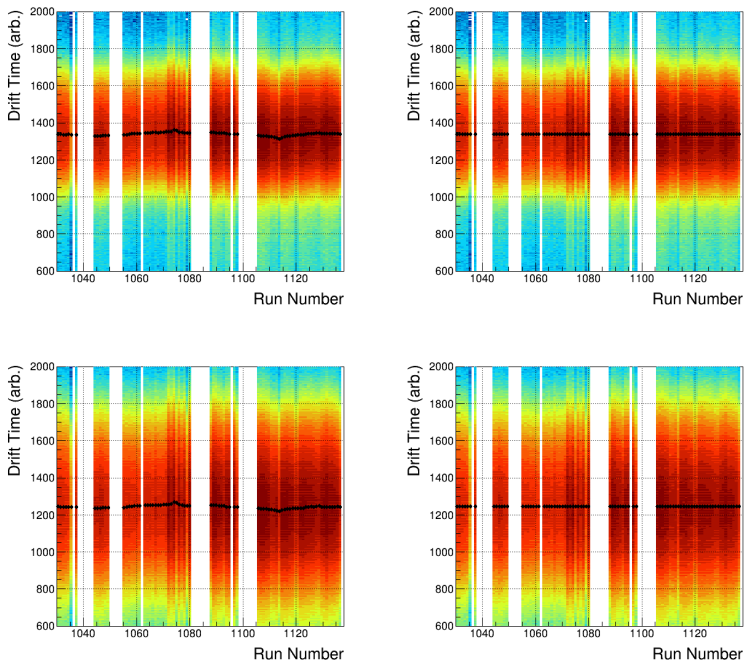

Figure 4.3: CRDC time-to-amplitude converter (TAC) drift calibration. This plot shows the TAC signal as a function of time (represented here by the run number). The black markers denote the mean drift time for each run number. The raw spectrum is on the left, and the calibrated spectrum is on the right.

4.1.1.4 CRDC position calibration

The horizontal (x) position calibration is determined by the charge collected among a handful of 2.54 mm wide pads. Pads that do not function properly were removed from the analysis in the pedestal calibration and are listed in Table 4.1. Removal of these pads should not

hinder the x-position determination, provided that a Gaussian fit of the charge deposited as a function of pad number among several illuminated pads can still be performed to extract the position. The vertical (y) position is measured via the drift time of the electron through the applied electric field at the top and bottom of the CRDCs. The drift time for the y-position and the charge distribution for the x-position need to be converted to positions in the lab frame. This detector frame to lab frame calibration is performed with a "mask run." The incoming beam is de-focused in order to detect particles in as large an area on the face of the CRDCs as possible. Two tungsten masks 6.35 mm thick with 1 mm diameter holes at known locations are inserted on independent drives in front of each CRDC one at a time. Heavy ions are either stopped by the tungsten mask or pass through the holes, creating a pattern which can be calibrated to the physical dimensions of the detector in the lab frame. A linear relationship between measured charge and x-position as well as between the measured time and y-position is obtained and applied. The x-position slope comes from the physical dimensions of the detector, and the offset is determined by the mask calibration. The y-position slope is determined by the spacing between the holes in the mask and the offset by the relative positions between the masks and CRDCs. CRDC1 has fewer mask holes visible in the spectrum because the beam spread is smaller directly following the Sweeper magnet where this CRDC sits. Slopes and offsets for the CRDC calibration are listed in Table 4.2. The CRDC pads are numbered in opposite orientations in the two detectors: CRDC1 pad number increases in the $+x$ direction in the lab frame, and CRDC2 pad numbers in the $-x$ direction. The slopes for the position calibration have opposite sign to reflect this geometry.

Table 4.2: Slopes and offsets for the CRDC position calibrations. The horizontal direction (x) and vertical direction (y) calibrations use a linear relationship. The opposite slopes reflect the opposite CRDC orientation in the lab frame.

	x_{slope} [mm/pad]	x_{offset} [mm]	y_{slope} [mm/ns]	y_{offset} [mm]
CRDC1	2.54	-176.71	-0.085	110.97
CRDC2	-2.54	186.66	-0.085	111.12

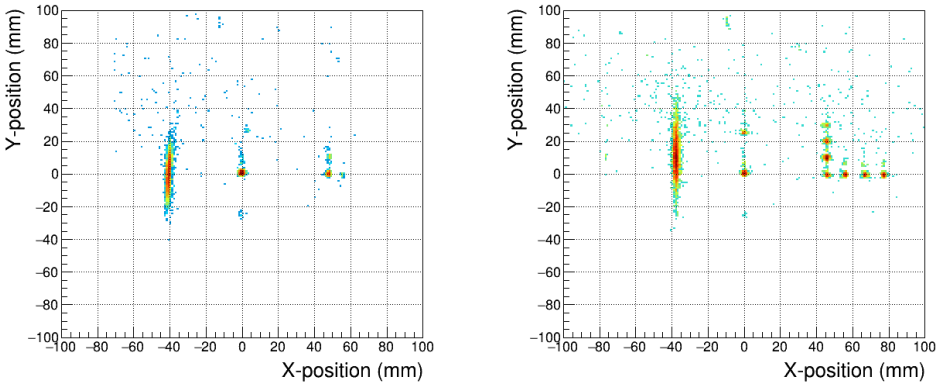

Figure 4.4: CRDC mask position calibration showing y-position versus x-position. The CRDC1 spectrum is on the left and the CRDC2 spectrum is on the right.

4.1.2 Ion chamber

The ion chamber is a gas-filled detector responsible for measuring the energy loss of a fragment in the suite of charged particle detectors, allowing for element identification of the detected fragments. The ion chamber has 16 charge collection pads segmented in the direction of the beam path. Charge collection is normalized over all pads to a reference pad for a given Z. Position dependence in the horizontal (x) direction is corrected for a given Z in order to normalize the response at the edges. The following sections detail the calibrations performed for the ion chamber.

4.1.2.1 Ion chamber gainmatch

The ion chamber is used to separate charged fragments with different proton number Z. The charge response for each pad needs to be normalized in order to ensure that the charge collected is the same for a known Z.

To get a large number of fragments with different Z, the wedge was removed from the A1900 fragment separator, discussed in section 3.1. This wedge is responsible for assisting in separation of various beam fragments with a similar $B\rho$ to the ^{33}Mg beam; the removal of this wedge allows transmission of many beam fragments created in the initial fragmentation of ^{48}Ca. The energy loss for the fragments in the ion chamber is proportional to Z^2 (Following the Bethe-Bloc formula) and the charge collection for each pad shows multiple peaks as shown in Figure 4.5 (left panel). Pads with bad charge collection are eliminated from the analysis and are listed in Table 4.3.

Table 4.3: Ion chamber pads removed from the analysis due to erroneous charge collection spectra.

Pad Number
0
4
7
15

Because the charge collection is summed over all pads, the exclusion of some pads does not affect the resulting measurement. For each pad, the peak positions are recorded and a linear fit between the peak positions relative to a reference pad is used to extract a slope and an offset. An example of this linear calibration for a single pad is shown in Figure 4.5 (right panel).

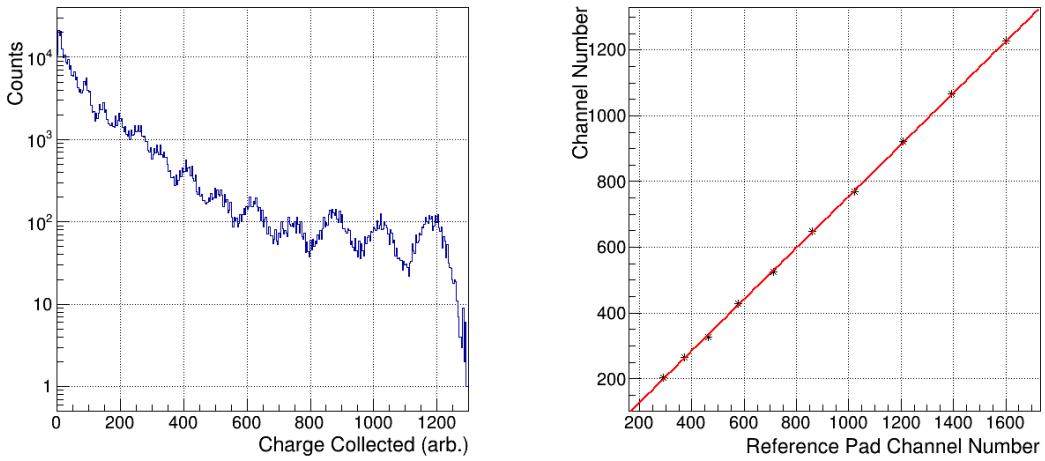

Figure 4.5: Energy loss measured by the first pad in the ion chamber during an "unwedged" beam setting. The multiple peaks in the left plot correspond to the various Z of the measured fragments. The peak locations inform the data points on the right plot.

The calibrated charge as a function of pad number for valid pads is shown in Figure 4.6 for a "beam-down-center" run for which the reaction target is removed. The two bands correspond to the desired secondary beam ^{33}Mg (Z=12) on bottom and the most prominent contaminant beam ^{36}Si ($Z = 14$) above. The un-calibrated spectrum is on the left and the calibrated spectrum is on the right.

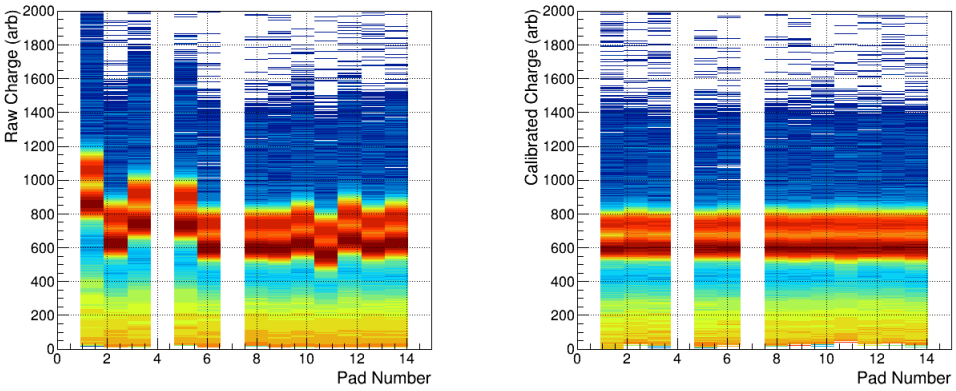

Figure 4.6: Ion chamber collected charge as a function of pad number during a "beam down center" run. The red region indicates the highest number of counts. The two bands correspond to the secondary beam ^{33}Mg with Z=12 (bottom) and the heavier contaminant beam ^{36}Si with Z=14 (top). The left spectrum shows the un-calibrated response and the right shows the calibrated one.

4.1.2.2 Ion chamber position correction

After the charge in each pad has been normalized for proton number Z, the position dependence in the horizontal direction must be corrected. The charge collected in the center of the ion chamber pads should be the same as the charge collected at the edges. To correct the position dependence of the ion chamber, "sweep" runs are performed during the experiment with no reaction target, varying the current supplied to the Sweeper dipole magnet discussed in section 3.4. Due to low statistics, two types of "sweep" runs were combined and used in the analysis: a "continuous sweep" where the beam was swept by continuously varying the dipole magnet currents, and "step sweeps" where the beam is swept using discrete currents for each run. The former illuminates the full area of the CRDCs available to the beam, while the latter illuminates different CRDC positions depending on the selected current. Events corresponding to un-reacted beam in the ion chamber are selected in order to isolate particles with the same Z. The energy loss as a function of position in the second CRDC, which lies

directly upstream of the ion chamber, is then used to correct the position dependence of the charge collection in the ion chamber. This correction is shown for one ion chamber pad in Figure 4.7. The un-corrected spectrum is shown on the left and the corrected spectrum is shown on the right.

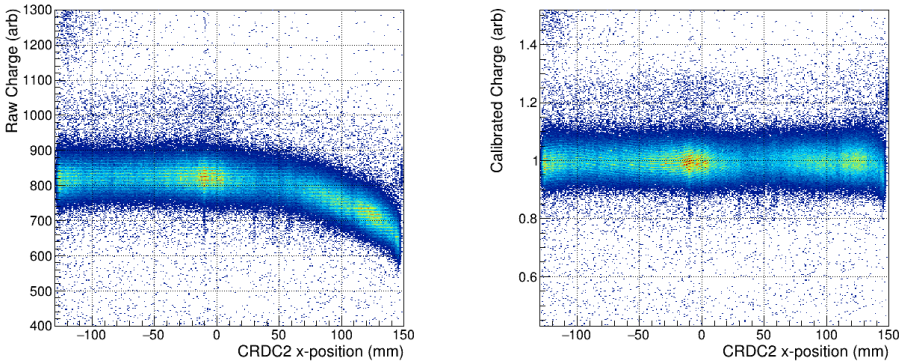

Figure 4.7: Ion chamber position correction. This plot shows the charge collected in the ion chamber as a function of the CRDC2 calibrated position. The raw spectrum is on the left and the calibrated spectrum is on the right.

4.1.3 Segmented reaction target

4.1.3.1 Detector drift correction

Over the course of the experiment, the silicon detectors in the segmented target array (discussed in section 3.3) incur radiation damage, impacting the efficiency of their charge collection. A calibration based on charge collected over time during the experiment is performed such that the detector has the same response to a given Z throughout the experiment. A linear calibration is performed on each detector's anode signal for ^{33}Mg beam particles as a function of the experiment run number which is analogous to time. This correction can be seen in Figure 4.8 for the first silicon detector.

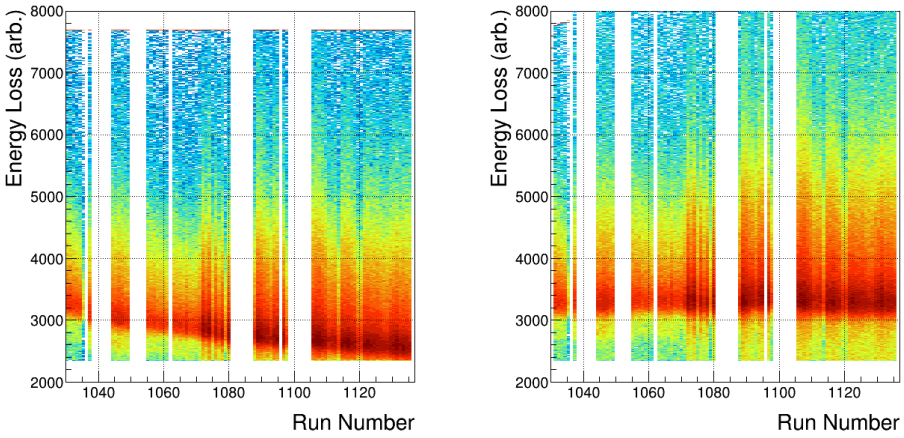

Figure 4.8: Silicon detector drift correction. The charge collected is shown as a function of the experiment run number (time) for events corresponding to un-reacted ^{33}Mg beam. The un-calibrated spectrum is on the left and the calibrated spectrum is on the right.

4.2 MoNA-LISA calibrations and corrections

The MoNA-LISA array (details discussed in section 3.6) consists of 144 bars of plastic scintillator. Calibrations for position and both global and relative time calibrations are performed in order to accurately reconstruct the neutron four-momentum. These processes are discussed in the following sections.

4.2.1 Charge calibration

The QDC calibration involves the determination of a threshold used by the data acquisition which is set to remove the QDC pedestal which represents the minimum charge collected due to noise in the electronics. A charge calibration is then performed to normalize the charge response in each bar. In order to calibrate the QDCs, cosmic ray data is collected. This is an offline procedure capturing background events, many of which originate from cosmic ray muons interacting with the MoNA-LISA detector bars. On average, the light produced by a

cosmic ray muon in a MoNA-LISA bar is roughly 20 MeVee (MeV electron equivalent)[57]. The light collected by each PMT is converted from raw charge in QDC channels into a calibrated light output in MeVee using the pedestal for an offset and the cosmic ray muon peak location for the slope. The two remaining features are a sharp peak at low energy from background γ rays and the broad cosmic muon peak. Figure 4.9 shows the charge collected in a single LISA detector bar before calibration (left) and after calibration (right) with the pedestal feature indicated.

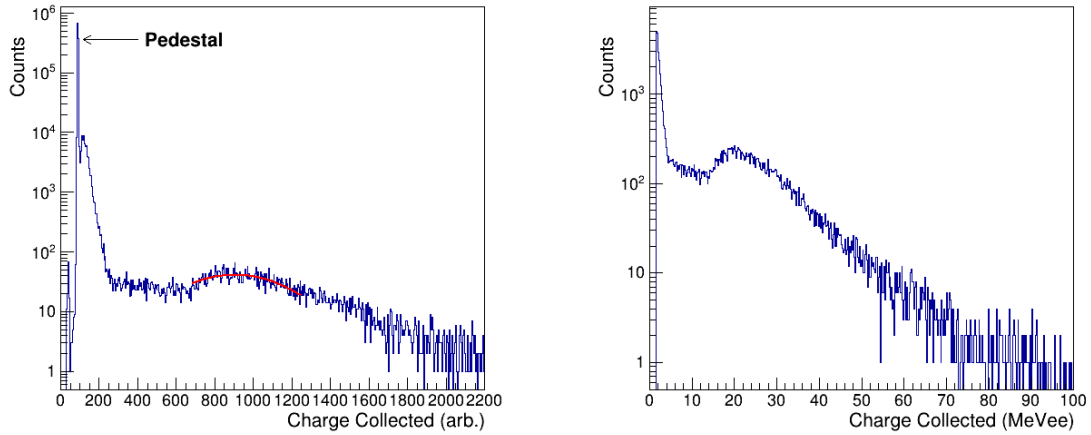

Figure 4.9: The collected charge in a single bar of the LISA array detected during an offline acquisition. The un-calibrated spectrum is on the left, and the calibrated spectrum is on the right. There is a minimum charge collected in each pad, called the "pedestal," denoted by the arrow in the left panel. The peak corresponding to the cosmic rays is calibrated to 20 MeVee as seen in the calibrated spectrum.

4.2.2 Time calibration

The MoNA-LISA detector bars are optically coupled to a PMT on both ends. The time signals are processed by a time-to-digital converter (TDC) for which a slope must be found to calibrate the time signals The offsets are set in subsequent calibration sections. A time calibrator module was utilized, providing a start and a stop signal at a set interval of 40 ns.

The time spectra associated with each PMT are characterized by a series of evenly spaced sharp peaks. The slope of a linear relationship between the TDC channels and time in nanoseconds is extracted and applied individually to each PMT. The final calibration for one PMT is shown in Figure 4.10. This provides a slope parameter for the TDC calibration, and overall timing offsets are discussed in section 4.2.4

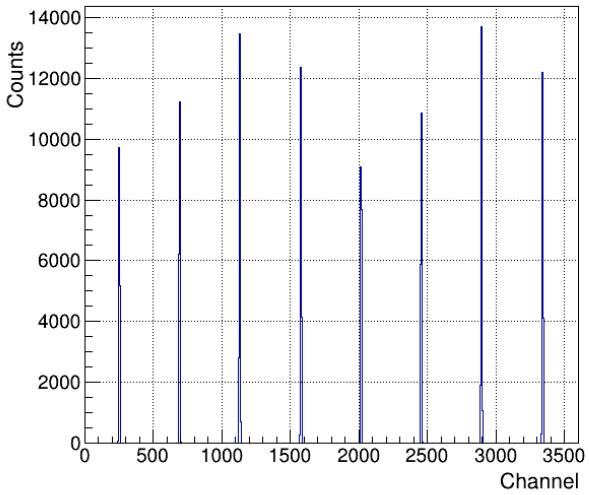

Figure 4.10: Un-calibrated (raw) LISA TDC spectrum for a single LISA detector bar during a run using a pulser (time calibrator) module. The "picket fence" pattern provides points for a linear calibration providing an identical timing response for each detector bar.

4.2.3 Position calibration

The MoNA-LISA array is segmented in the direction of the beam path (z) and in the vertical direction (y). This provides positions in these dimensions with an accuracy of the width of one scintillator bar(10 cm). The horizontal (x) position is determined by the time-of-flight of the scintillation light produced by the nuclear reaction induced by a neutron in the detector volume. Because the light produced travels at a constant speed, the position of the interaction can be deduced from the time difference between PMT signals read out from

either end. A long offline acquisition of cosmic ray muon data provides events uniformly distributed along the length of the bar. The raw calibration spectrum has distinct edges fit with a Fermi function and the locations converted to the dimensions of the detector, shown in Figure 4.11. A linear calibration slope and offset are extracted and applied, resulting in the calibrated spectrum on the right panel of Figure 4.11. The position calibration detailed here specifies the location of a hit relative to the center of the bar. Precise laser measurements of the experimental vault are used to determine the offset for absolute locations in the lab frame.

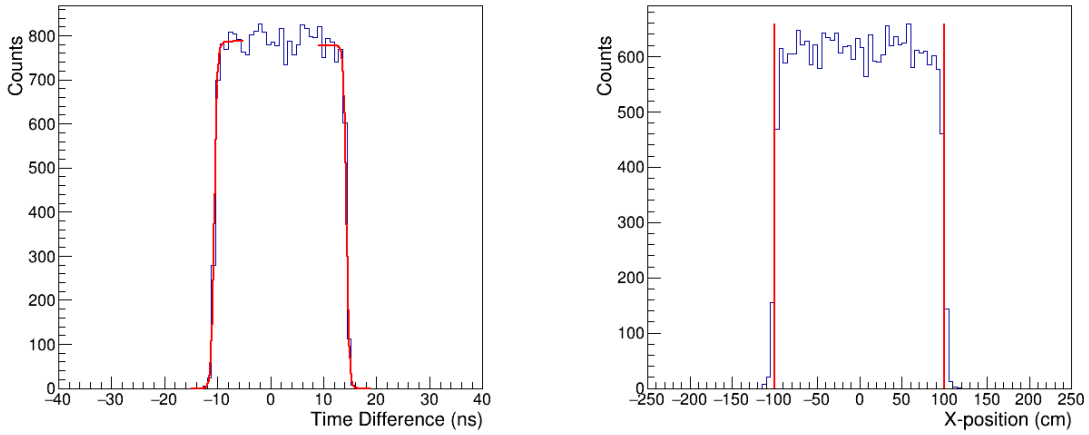

Figure 4.11: The x-position calibration for a single LISA detector bar. The un-calibrated time spectrum is on the left showing the distribution fit on both ends with a Fermi function. The calibrated position spectrum is on the right, with the red vertical lines corresponding to the ends of the bar at -100 cm and 100 cm.

4.2.4 Timing offsets

Previously detailed TDC calibrations provided a slope for a linear calibration of the MoNA-LISA detector bars. The overall timing offset must also be determined for each bar. The MoNA-LISA array is organized into three "tables" or groups of bars which are shown in chapter 3. Timing offsets between each bar and a reference bar in its layer must be de-

termined, as well as the timing offset of each table relative to the reaction target. These processes will provide time offsets for each of the MoNA-LISA detector bars such that they are all on the same time scale.

The triggering signals used are not individually wired, but chained together, so the TDC times are slightly different. This leads to shifts in average time calculated between the two TDCs which informs the x-position of the event. A long, offline run collecting cosmic ray muon data was performed and events were selected for which the muon traveled nearly vertically through a given layer. The difference in the calibrated x-position of the hits between bars in a given layer and the speed of the muons (assumed to be c) are used to determine an absolute timing offset between a given bar and a reference bar in that table.

The overall timing offset between the reaction target and each MoNA-LISA table must then be determined. γ rays from fragmentation at the reaction target occasionally deposit energy into MoNA-LISA. The speed of the photons and the calibrated position of the neutron hit in MoNA-LISA, assuming that the photons originate from the center of the segmented target array, provide an absolute time of flight as shown in Figure 4.12. Once these two timing offsets have been applied, each bar and table of the MoNA-LISA array are on the same absolute time scale and calibrations are complete.

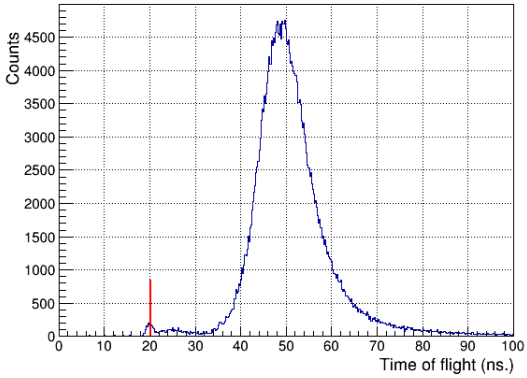

Figure 4.12: Calibrated time spectrum for the center bar in the first layer of the LISA array during all experimental runs. The large peak corresponds to the neutron time of flight, and the peak with the fastest time of flight corresponds to the γ rays, marked by the red vertical line.

4.3 Event selection

Reconstructing the decay energy spectrum of an unbound nucleus requires selecting events that correspond to a specific charged fragment detected in coincidence with a neutron. A thin scintillator detects charged fragments and is responsible for triggering the data acquisition. Secondary beam contaminants, reactions other than the two-proton knockout desired, and background events from random coincidence between MoNA-LISA and Sweeper can trigger this acquisition and must be removed from the analysis to isolate the desired ^{30}Ne fragments. The following sections detail the process of distinguishing events corresponding to the desired reaction and subsequent decay.

4.3.1 Beam identification

The ^{33}Mg secondary beam was delivered along with two other beam fragments referred to as "contaminants," ^{36}Si and ^{34}Al. Accompanying these main components are light fragments

originating from reactions in the aluminum wedge in the A1900 separator. Event selection begins with isolating those coming from the desired ^{33}Mg which is done using a combination of two software cuts: one on the time-of-flight and one on the energy loss.

The first of these cuts is on the time-of-flight from the A1900 XFP scintillator to the target scintillator. The delivered fragments all have the same magnetic rigidity ($B\rho$) but different A and Z, and thus different velocities. The time-of-flight for the ^{33}Mg beam was sufficiently isolated from the ^{36}Si and ^{34}Al beam "contaminants" as seen in Figure 4.13. The intense regions from left to right correspond to ^{36}Si, ^{34}Al, and ^{33Mg}. The red lines indicate the selected events.

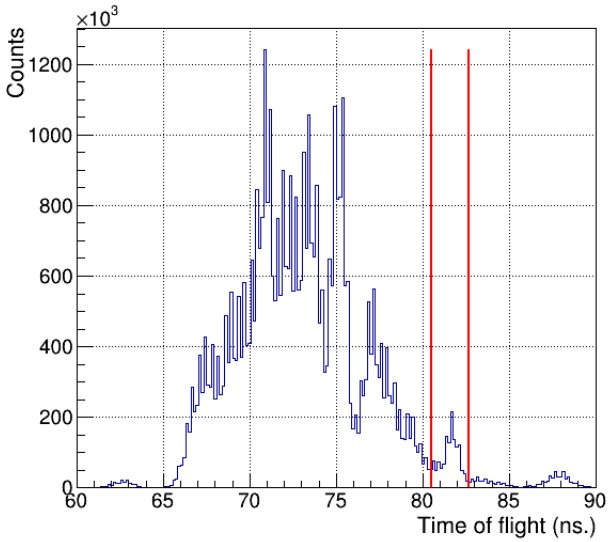

Figure 4.13: Time-of-flight between the A1900 fragment separator and the scintillator just upstream of the reaction target. The secondary ^{33}Mg time-of-flight selection is shown between the red lines.

The second cut is on the energy loss in the segmented target's first silicon detector. The delivered beam includes many low-Z fragments which need to be separated from the ^{33}Mg selection. A cut on the energy loss in the silicon detector eliminates light particles for

which the time-of-flight are the same as the desired ^{33}Mg beam. The segmented target has four silicon detectors, which had been used (and radiation damaged) in only one previous experiment [49, 48]. The bias voltage for these detectors was not changed to account for this radiation damage, and signal pileup is evidenced by the observed "tails" of the energy loss distributions. The time-of-flight gate will include nuclides with identical $\frac{A}{Z}$ to ^{33}Mg. Any lighter nuclides whose tail may "leak" into the ^{33}Mg selection are filtered out of the analysis when element selection is done in a later step. There are no nuclides heavier than ^{33}Mg expected from the A1900 fragment separator and thus the full vertical extension of the tail is accepted as part of the ^{33}Mg beam selection. Figure 4.14 shows the energy loss as a function of time-of-flight. The three intense regions above 3000 in the figure correspond to the three heaviest nuclides: ^{36}Si, ^{34}Al and ^{33}Mg from left to right, respectively. The collection of intense regions below channel 3000 are various lighter species of nuclei produced in the fragmentation of the primary ^{48}Ca beam. The final beam selection of ^{33}Mg can be seen in Figure 4.14.

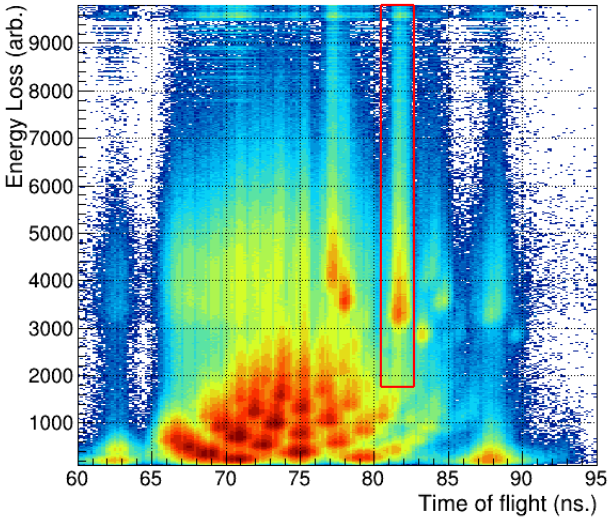

Figure 4.14: Energy loss in the first silicon detector of the reaction target as a function of the time-of-flight between the A1900 fragment separator and the scintillator just upstream of the reaction target. The secondary ^{33}Mg beam selection is shown in the red box.

4.3.2 Element identification

At the segmented reaction target, the ^{33}Mg nuclei may fragment in any of the three beryllium reaction targets. Most of the beam will not react and these events can provide a benchmark for isotope identification. After the ^{33}Mg secondary beam is selected using the first silicon detector, the neon isotopes must be separated from the rest of the reaction products. This is achieved by examining the energy loss in the ion chamber as a function of the time of flight between the scintillator in front of reaction target and the one directly following the ion chamber. The corresponding reaction products originating from the fragmentation of the ^{33}Mg beam are shown in Figure4.15. The most intense region of the histogram corresponds to un-reacted ^{33}Mg. Because the energy loss is proportional to Z^2, the resulting bands can easily be identified, starting from ^{33}Mg at $Z = 12$. The events corresponding to the lighter elements can be assigned in descending order. The neon reaction products, with $Z = 10$, are

identified in the red box in Figure 4.15.

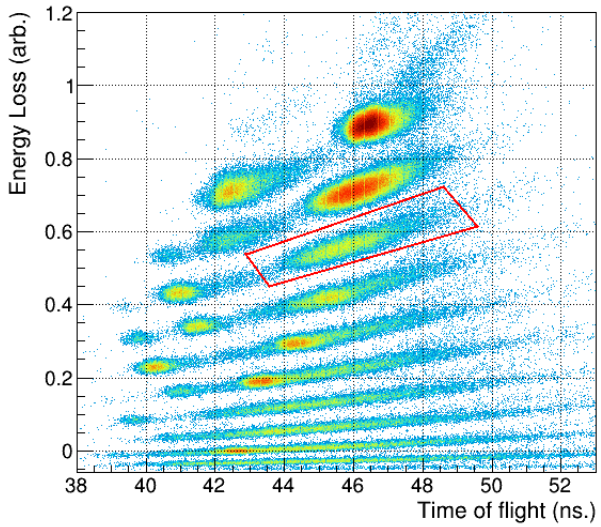

Figure 4.15: Energy loss in the ion chamber as a function of the time of flight between the scintillator just upstream of the reaction target and one directly following the ion chamber. The most intense region of the histogram represents un-reacted secondary ^{33}Mg beam events. The neon element selection is shown in the red box.

4.3.3 Reaction target identification

The segmented reaction target used in this experiment is comprised of four silicon detectors which measure the energy loss of the detected particles, and three thin beryllium targets interleaved with the silicon detectors, where the two-proton knockout from ^{33}Mg into ^{31}Ne takes place, as well as the instantaneous neutron decay to ^{30}Ne. The energy loss measurements before and after each reaction target provide a way to distinguish particles with different Z, making it possible to identify the specific target associated with the desired two-proton-knockout and improve the resolution of the decay energy measurement by limiting the ambiguity about the reaction location. To do this selection, a plot of the energy loss in one silicon detector is plotted versus another for events which entered the setup as

^{33}Mg and reaction products which have been determined to be neon. The incoming particles will lose energy in the first silicon target corresponding to the ^{33}Mg beam, and the neon reaction products will deposit less energy in the detectors following the target where the reaction took place. The selections for each target are shown in Figure 4.16, along with a schematic that explains the selection requirements in the top left panel. Figure 4.17 shows the one-dimensional projections of the cuts made on the data.

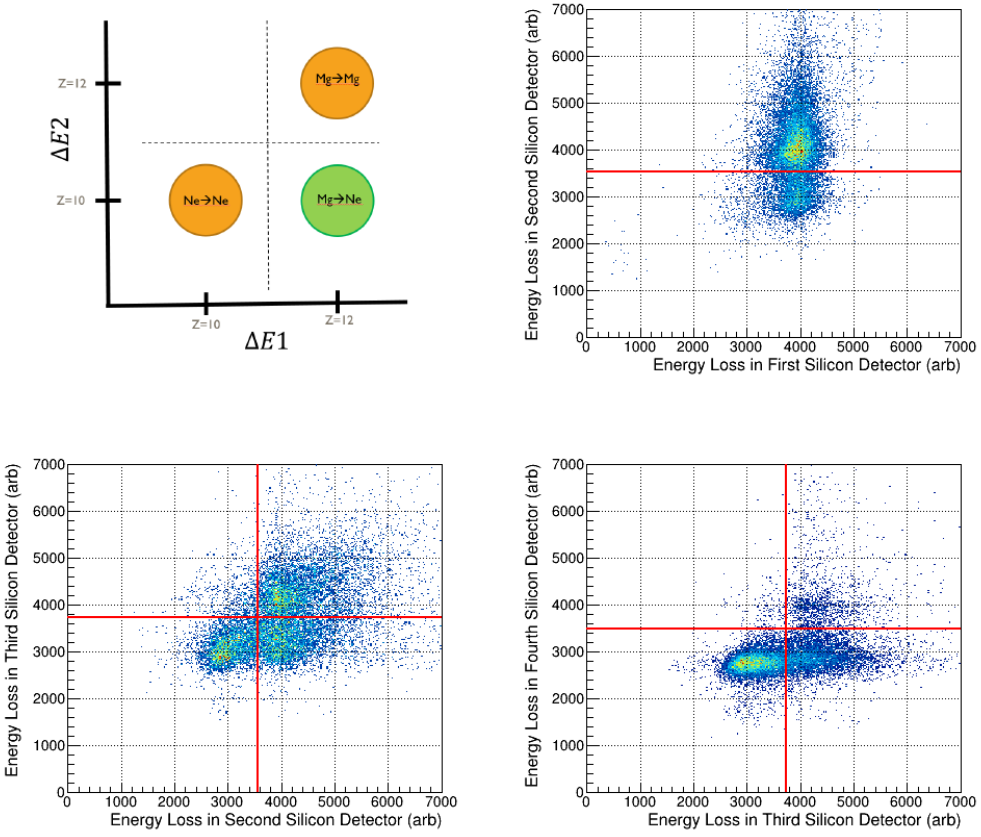

Figure 4.16: Target selection gates for each of the three Beryllium targets. The energy loss of one silicon detector is plotted versus the energy loss in the preceding one; the reaction target associated with the identification is between them. Top left: schematic showing an example of the selection. The selection in the data are shown for target 1 (top right), target 2 (bottom left) and target 3 (bottom right). This plot includes only events which originate as ^{33}Mg and react to form a neon isotope.

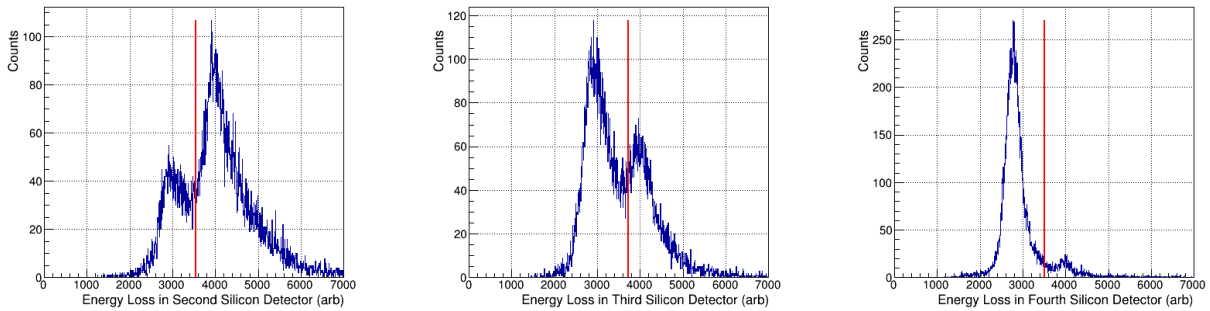

Figure 4.17: Target selection gates for each of the three Beryllium targets. The energy loss is shown for the second (left), third (middle), and fourth (right) silicon detectors, with red lines showing the gates from Figure 4.16. This plot includes only events which originate as ^{33}Mg and react to form a neon isotope.

4.3.4 Isotope identification

After specific events are selected to isolate the reaction products by atomic number Z, an identification of mass number A must be made in order to isolate the fragment of interest, in this case ^{30}Ne. The magnetic rigidity of each (non-relativistic) charged fragment is given by $B\rho = \frac{mv}{q}$ and the velocity $v = \frac{\Delta L}{\Delta t}$. Therefore, the time of flight through a magnetic field is proportional to the fragment mass number A:

$$v = \frac{\Delta L}{\Delta t} = \frac{B\rho q}{m} = \frac{B\rho Ze}{Am_u} \propto \frac{1}{A} \tag{4.1}$$

where L is the path length of the trajectory of the fragment through the magnetic field, t is the time of flight, $q = Ze$ is the fragment charge, A is the mass number and m_u is the nucleon mass. In principle, a time-of-flight measurement can be used to separate mass number for fragments with the same B_ρ.

The position and angle at the CRDCs and the time-of-flight are all dependent on the mass

number A but cannot independently provide isotope identification. Variations in the path length L and magnetic rigidity B_ρ cause the time-of-flight and position distributions of individual isotopes to be washed out and overlap. These distributions are influenced by the momentum acceptance of the A1900 fragment separator, straggling in the segmented target, the non-uniformity of the Sweeper magnetic field, and decay and reaction dynamics. Assuming the incident beam position to be the reference position and with an angle perpendicular to the target, a correlation between these the remaining parameters can be untangled to provide a "corrected" time-of-flight parameter which is capable of separating the isotopes of an element band such as the neon selected in Figure 4.15.

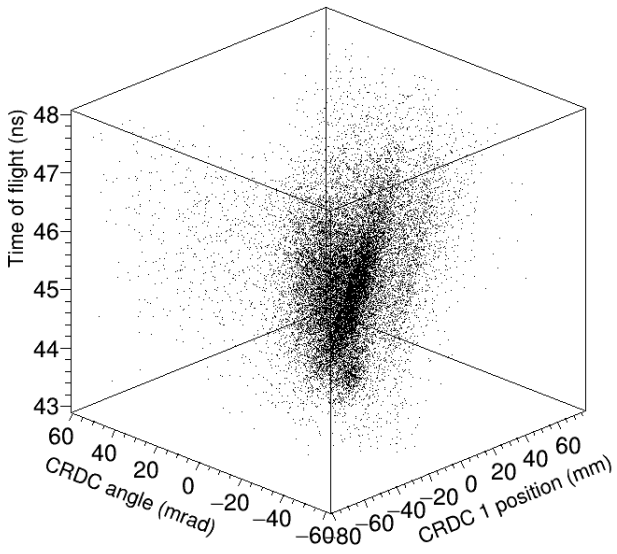

Figure 4.18: Correlation between time-of-flight, position, and angle for neon reaction products.

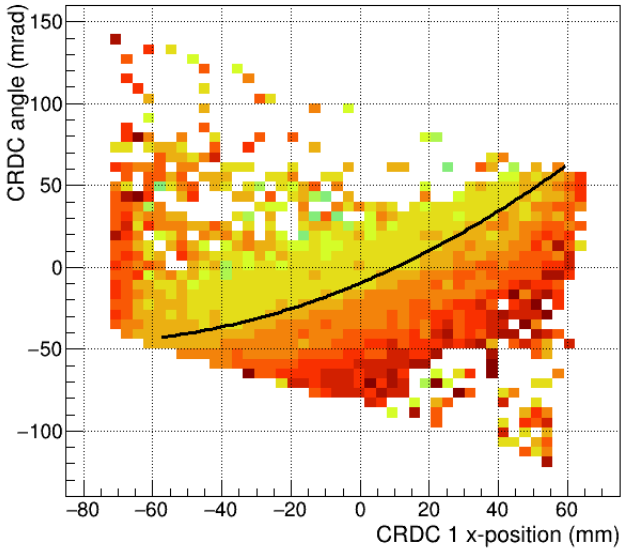

Figure 4.19: Projection of the time-of-flight onto the dispersive angle and dispersive position. The curve follows the contour of a constant time-of-flight.

The first step in the isotope identification is to construct a parameter which contains information about the relationship between the time-of-flight and the dispersive plane position and angle. A 3D scatter plot of the time-of-flight versus dispersive angle and position for the neon reaction products is shown in Figure 4.18. There are faint band structures corresponding to the various detected neon isotopes. This plot can then be projected down onto the dispersive angle versus dispersive position plane as shown in Figure 4.19. The color contours, highlighted by the curve in the figure, are representative of an iso-time-of-flight, for which particles with different A will be separated.

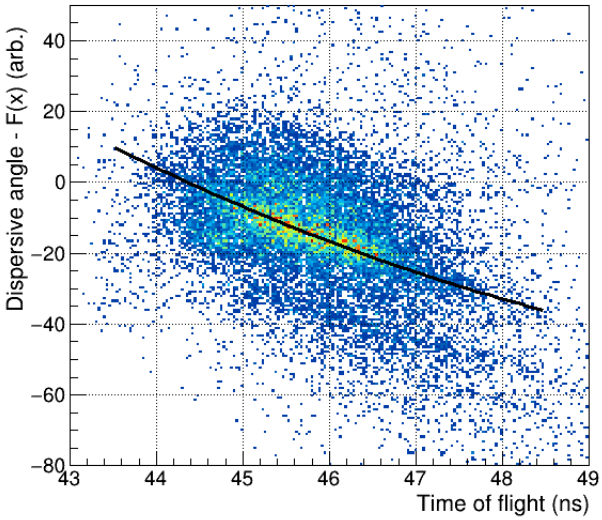

Figure 4.20: The functional dependence of the CRDC1 x position (dispersive position) on CRDC x angle (a new parameter) as a function of the time-of-flight. The curve represents the correlation function between the two parameters.

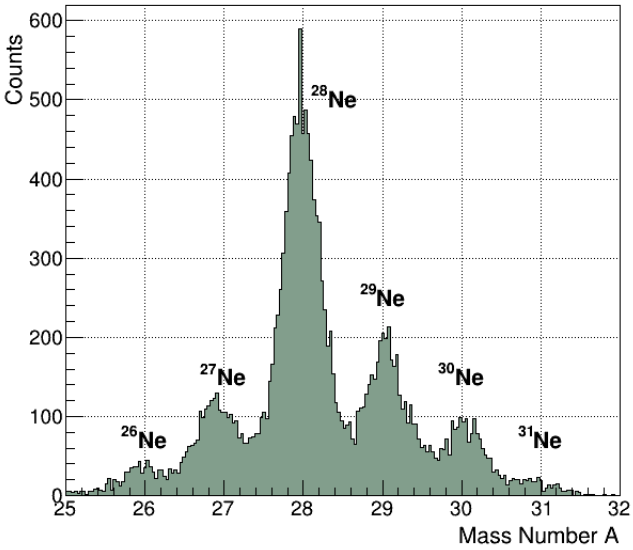

Figure 4.21: One-dimensional particle ID parameter indicating the mass number A. The labels correspond to the isotopes present.

The second-order polynomial relationship shown between the dispersive angle and dispersive position is unfolded and plotted versus the time-of-flight, shown in Figure 4.20. Another

second-order polynomial can be used here, shown as a black curve, in the same way to create another parameter which can be examined for isotope separation. This so-called "Particle Identification"(PID) parameter is shown in Figure 4.21 which is proportional to the mass number A. The heaviest expected neon reaction product from the ^{33}Mg beam will be ^{31}Ne due to the two-proton knockout, which is bound in its ground state and should be detected in the suite of charged particle detectors. Figure 4.21 shows labels for all detected neon fragments originating from fragmentation of the ^{33}Mg beam. In Figure 4.22 the detected isotopes of neon are distinctive colors, emphasizing the band structure which is hard to discern in Figure 4.18.

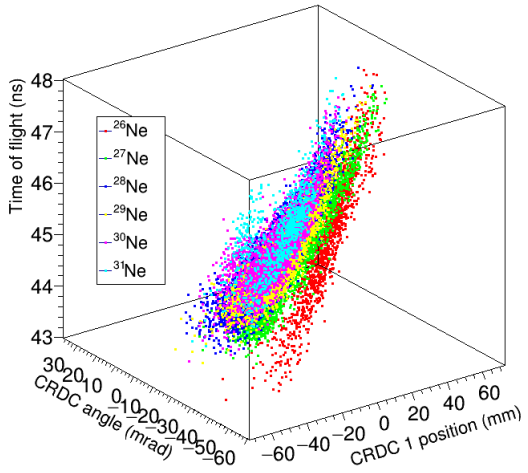

Figure 4.22: Correlation between time-of-flight, position, and angle for neon reaction products. The detected isotopes are shown in various colors to emphasize the banding structure of the various neon isotopes.

4.3.5 Neutron selection

After the desired charged particle events have been selected, a neutron requirement must be imposed to select events which correspond to a detection of both the neutron and the

desired fragment. The charge and time-of-flight spectra for MoNA-LISA contain true neutron events, but also coincidences with other particles such as photons or muons which should be removed from the analysis. To do this, an event selection is imposed on the MoNA-LISA time-of-flight and charge collection spectra in order to isolate true neutron events. The desired neutrons will have a time-of-flight similar to that of the beam and a one-dimensional cut on this parameter is utilized to isolate the desired neutrons. Further constraints on the background include a one-dimensional cut on the charge collected to eliminate events with low light output.

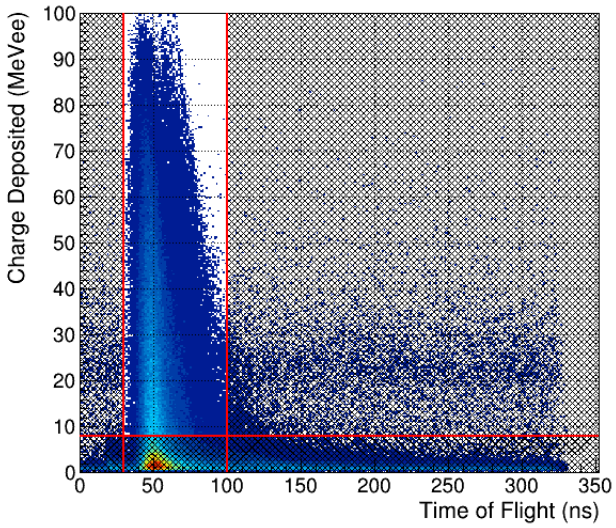

Figure 4.23: Neutron selection based on time-of-flight and deposited charge in LISA. Events which lie in the un-marked area are selected as neutron events. All others are assumed to be detected particles other than neutrons (e.g. photons).

Once the neutron events have been selected, a coincidence between the selected ^{30}Ne is imposed. Figure 4.24 shows the particle ID again in dark green, and in light green the events in coincidence with a neutron. These events originate from a ^{33}Mg beam which underwent a two-proton knockout populating ^{31}Ne* that immediately decayed via one-neutron decay

to populate ^{30}Ne, for which a neutron was detected in coincidence (represented by the light green region between the two red lines in Figure 4.24).

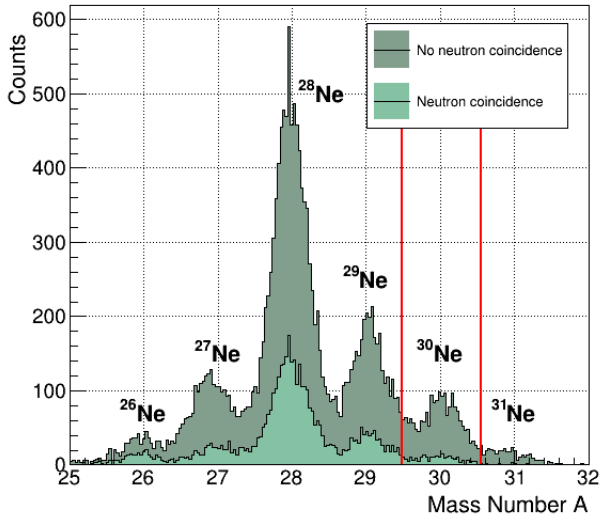

Figure 4.24: One-dimensional particle ID parameter indicating the mass number A. All detected fragments are shown in the dark green histogram, while a neutron coincidence requirement gives the light green histogram. The selection on ^{30}Ne fragments is shown between the red bars.

4.4 Fragment reconstruction

The method of invariant mass spectroscopy requires knowledge of the four-momentum vector at the decay point for the decay products. The neutrons from the various reactions and decays in the segmented reaction target travel without a significant loss of speed to the MoNA-LISA neutron detectors and their four-momentum is reconstructed based on angle and position. The charged fragments, however, pass through the magnetic dipole field of the Sweeper magnet on paths unique to each nuclide. The determination of the four-momentum at the target position is accomplished through the use of a third-order non-linear ion-optical matrix calculation with COSY INFINITY [58], with the measured fragment angles and

positions as inputs, that tracks the fragment path back to the target location and includes information about the strength and shape of the magnetic field. The angles and positions at the center of each target, as well as the energy of the fragment at the exit of the target come from this matrix calculation.

$$\begin{pmatrix} x^{(crdc1)} \\ \theta_x^{(crdc1)} \\ y^{(crdc1)} \\ \theta_y^{(crdc1)} \\ L \end{pmatrix} = \mathrm{M} \begin{pmatrix} x^{(target)} \\ \theta_x^{(target)} \\ y^{(target)} \\ \theta_y^{(target)} \\ E^{(target)} \end{pmatrix} \tag{4.2}$$

However, COSY INFINITY uses a different set of coordinates (x, a, y, b, l, δ) which are defined as

$$a \equiv \frac{p_x}{p_z} = tan\theta_x \approx \theta_x \tag{4.3}$$

$$b \equiv \frac{p_y}{p_z} = tan\theta_y \approx \theta_y \tag{4.4}$$

$$l \equiv -\frac{v_0\gamma_0}{1+\gamma_0}(t - t_0) \tag{4.5}$$

$$\delta \equiv \frac{K - K_0}{K_0} \approx 2\frac{\Delta p}{p} \tag{4.6}$$

where the subscript 0 denotes the reference particle which follows the central trajectory used in the creation of the ion-optical matrix. The transverse angles of the beam, θ_x and θ_y are assumed to be small and are represented by the quantities a and b, respectively. The quantity δ is the deviation of the kinetic energy from the reference particle.

The matrix is not square and non-linear terms must be included. The calculation was carried out to third order, and the matrix elements were calculated by COSY INFINITY. Not all phase space dimensions are used in the analysis, therefore the dimensionality can be reduced so that the matrix can be "partially inverted," resulting in the equation:

$$\begin{pmatrix} a_t \\ y_t \\ b_t \\ l_t \\ \delta \end{pmatrix} = \mathbf{M}_{part.\ inv.} \begin{pmatrix} x_d \\ a_d \\ y_d \\ b_d \\ x_t \end{pmatrix} \tag{4.7}$$

where the t subscripts refer to the target-position variables, and d refers to the detector-position variables.

Table 4.4: Inputs for the COSY INFINITY matrix calculation.

Parameter	Value	Description
order	3	Optics calculation order
angle	-0.3°	Incoming beamline angle
pos	0.050 m	Coordinate conversion for field map
drift	1.56 m	Arc length of central trajectory

The calculation of the partial inverse matrix using COSY INFINITY requires information about the angle and position of the beam line, the path length through the center of the Sweeper dipole field, and the beam particle mass, charge, and reference B_ρ. These inputs

Table 4.5: Sweeper current, Hall probe value, and magnetic rigidity for the ^{30}Ne setting used in the COSY map generation.

Current (A)	337
Hall Probe (kG)	-10.360
B_ρ for 43.3 ° bending	3.674

are detailed in Tables 4.4 and 4.5.

4.5 Modeling and simulation

After the calibrations are complete, the desired events corresponding to the one-neutron decay of ^{31}Ne have been isolated, and the desired quantities are reconstructed and calculated, a simulation must be performed to fit a decay model to the experimental data. The simulations include the effects of the acceptance and efficiency of both MoNA-LISA as well as the charged particle detectors, and take into account the incoming beam profile, energy losses in the segmented target, and also include reaction and decay processes.

There are two parts to the simulation code which handle the charged fragments and neutron interactions individually. One part of the code is comprised of an in-house C++ based simulation package called ST_MONA which handles the charged particle propagation and detection. The other part of the code is a GEANT4 simulation for the neutron interactions in MoNA-LISA using the neutron physics package MENATE_R within GEANT4. Characterization of the simulation code has been performed and benchmarked in previous studies [59, 53, 60, 51, 61, 52].

The incoming beam parameters in the transverse directions ($x-$ and y-position and angles) are modeled in ST_MONA by Gaussian distributions that can be set with a mean and standard deviation. Kinetic energy of the beam is modeled by a uniform distribution in which

the centroid and width are determined by the A1900 separator rigidity and slit settings.

The beam is propagated through the target, in which energy loss and straggling are taken into account. The reaction occurs at a randomly-chosen position, the dynamics of which are modeled in the Glauber formalism using a longitudinal momentum kick as in Ref. [62] and a transverse momentum kick as in Ref. [63]. The resonant lineshape input distribution used by ST_MONA which models the decay is sampled randomly to model the subsequent decay. The two-body decay energy is modeled within ROOT using the TGenPhaseSpace class. The fragment energy loss is calculated as the beam passes through the segmented target. The fragments are then propagated through the dipole magnetic field using the third-order COSY matrix and onto the face of CRDC1, after which a drift is applied for the fragments to reach CRDC2. Each CRDC has resolution effects on the simulated data, which is tracked backward to the target position using the partial-inverse COSY matrix. This backward-tracking is the same process applied to the data when reconstructing the four-momenta; using it for the simulation ensures the simulation and data are treated in a similar manner. The output of this ST_MONA simulation contains the charged particle detections and is sent to a GEANT4 simulation which handles the neutrons associated with the simulated ST_MONA decays.

The output ROOT file is put through a GEANT4 simulation which simulates the neutron interaction in MoNA-LISA. The neutron interactions are modeled using the MENATE_R database which supplies cross-sections for the neutron-carbon and neutron-hydrogen interactions which make up the MoNA-LISA scintillator bars. This simulation contains timing and position resolutions of the MoNA-LISA bars as well as a calculation of the light output as described in Ref. [64]. The output of the ST_MONA and GEANT4 simulations are

merged, now including both the charged particles and the neutron interactions. The inverse tracking is done at this point and the decay energy is reconstructed at the target position using the partial-inverse COSY matrix, following the same procedure as the data, allowing direct comparison.

Each simulation provides information about the position of the reaction within a specific beryllium target. However, because the segmented target contains three of these targets, one simulation for each target is performed and these three simulation files are merged before comparison with the experimental data. Cuts on the latter which select the desired fragment and neutron associated with the desired decay can inform simulation integrity as beam parameters are tuned. There are three types of parameters to set: incoming beam parameters to describe the ^{33}Mg beam, reaction parameters describing the two-proton knockout of ^{33}Mg to ^{31}Ne, and the decay parameters associated with the one-neutron decay of ^{31}Ne. The following sections describe the tuning of these parameters.

4.5.1 Incoming beam parameters

The incoming beam profile was determined by comparing the $x-$ and y-positions and angles at each CRDC corresponding to the incoming ^{33}Mg and detected charged fragment ^{30}Ne. The beam energy of 88.80 MeV/u with a spread of 0.17 MeV/u just upstream from the segmented target was determined by the settings of the A1900 fragment separator and the energy loss in the timing scintillator located upstream from the reaction target. The x- and y-positions and angles measured at the CRDCs (peak centroids) were used to tune the beam parameters such that the charged fragment distributions match the simulated data against the experimental data as shown in Figure 4.25. Table 4.6 shows the beam parameters

determined from this comparison.

Table 4.6: Beam parameters used in the ST_MONA simulation package.

Parameter	Value	Description
eBeam	88.6	Beam energy (MeV/u)
beamA	33	Beam A
beamZ	12	Beam Z
targA	9	Target A
targZ	4	Target Z
dEbeam	1.7	Width of energy distribution (MeV/u)
bSpotCx	0.006	Beam spot x centroid (m)
bSpotCtx	-0.018	Beam spot θ_x centroid (rad)
bSpotCy	-0.0095	Beam spot y centroid (m)
bSpotCty	0.0065	Beam spot θ_y centroid (rad)
bSpotDx	0.018	Beam spot x width (σ) (m)
bSpotDtx	0.008	Beam spot θ_x width (σ) (rad)
bSpotDy	0.007	Beam spot y width (σ) (m)
bSpotDty	0.007	Beam spot θ_y width (σ) (rad)

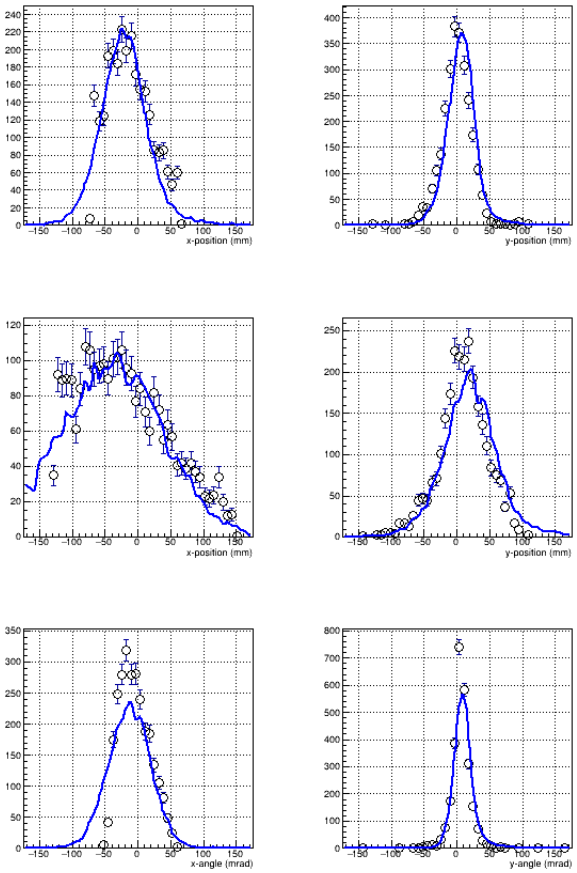

Figure 4.25: Comparisons of simulation parameters with data for positions and angles measured by the CRDCs. Data is represented by open circles and the simulation by blue curves. Top Row: CRDC1 $x-$ and $y-$position. Middle row: CRDC2 $x-$ and $y-$position. Bottom row: CRDC $x-$ and $y-$angle.

4.5.2 Reaction parameters

The two-proton knockout from ^{33}Mg was simulated by the removal of the two nucleons and a subsequent momentum kick is imposed on the resulting system. The scale of this momentum kick is a reaction parameter which needs tuning. The momentum kick was implemented by the Glauber model as described in Refs. [62, 63]. The momentum kick is input as a Gaussian distribution centered at zero with a standard deviation as defined in Refs. [62, 63], the width of which is scaled by an adjustable scaling factor. The scale of the Glauber kick was fixed

through the comparison of the width of the CRDC position and angle distributions with the experimental data. Table 4.7 shows the scale of the momentum kick used in the simulation. This kick is included in the comparison shown in Figure 4.25 and contributes to the peak widths.

Table 4.7: Glauber kick implemented for the two-proton knockout reaction in ST_MONA.

Parameter	Value	Description
glaub	3.10	Scale of momentum kick

4.5.3 Decay parameters

After the incoming beam and reaction parameters have been determined, the decay parameters for the one-neutron decay are the only free paraeters in the simulation. The neutron-decay Breit-Wigner lineshapes are detailed in Chapter 2. Each resonant lineshape is defined by an energy (E) and a width (Γ). The values of the decay parameters are determined using a method of maximum likelihood, which is discussed in the following section.

4.5.4 Parameter estimation

4.5.4.1 Binned likelihood method

Parameter estimation of the resonant lineshapes was accomplished through the use of a binned likelihood maximization, the method of which is discussed in Ref. [65]. The experimental data can be considered as a set of random values populated by some intrinsic probability density function (PDF). A functional form of this PDF can be assumed and the values of the parameters that describe it can be estimated from the experimental data set.

A maximum likelihood method is one way of performing this parameter estimation given a finite set of data. The likelihood function is defined as:

$$L(\vec{\theta}) = \prod_{i=1}^{n} f(x_i, \vec{\theta}) \tag{4.8}$$

Where θ are the parameters of the chosen PDF, n is the number of data points, and x_i are the measured values of the experimental data set. The values of the estimators $\vec{\theta}$ are determined by finding the values which maximize log $L(\vec{\theta})$. This work uses a logarithm of the likelihood function such that the product in equation (4.8) becomes a sum.

For this analysis, the log $L(\vec{\theta})$ (log-likelihood) is calculated with binned data. The histogram is treated as an N-dimensional random vector, with n entries and expectation values $\nu(\vec{\theta})$. The joint PDF is a multinomial distribution:

$$f_{joint}\left(\vec{n}, \vec{\nu}\right) = \frac{n_{tot}!}{n_1!...n_N!} \left(\frac{\nu_1}{n_{tot}}\right)^{n_1} ... \left(\frac{\nu_N}{n_{tot}}\right)^{n_N} \tag{4.9}$$

Taking the logarithm of this PDF and dropping terms that do not depend on $\vec{\theta}$ results in the log-likelihood function:

$$\log\ L(\vec{\theta}) = \sum_{i=1}^{N} n_i\ \log\ \nu_i\left(\vec{\theta}\right) \tag{4.10}$$

The estimators $\vec{\theta}$ are found by maximizing this log-likelihood function.

For a function with only one parameter, the log-likelihood can be expanded about the maximum likelihood estimator $\hat{\theta}$ by a Taylor expansion.

$$\log\ L(\theta) = \log\ L(\hat{\theta}) + \left[\frac{\partial \log\ L}{\partial \theta}\right]_{\theta=\hat{\theta}} \left(\theta - \hat{\theta}\right) + \left[\frac{\partial^2 \log\ L}{\partial^2 \theta}\right]_{\theta=\hat{\theta}} \left(\theta - \hat{\theta}\right)^2 + ... \qquad (4.11)$$

By definition, $\log\ L(\hat{\theta}) = \log\ L_{max}$ and the second term is zero when the maximum-likelihood estimator is at the "true" value. Ignoring higher-order terms yields the equation

$$\log\ L(\theta) = \log\ L(\hat{\theta}) - \frac{(\theta - \hat{\theta})^2}{2\hat{\sigma}^2_{\hat{\theta}}} \qquad (4.12)$$

or

$$\log\ L(\hat{\theta} \pm \hat{\sigma}_{\hat{\theta}}) = \log\ L_{max} - \frac{1}{2} \qquad (4.13)$$

A 1σ statistical uncertainty is identified where the maximum-likelihood value decreases by the value 0.5. For more than one parameter, the profile of the log-likelihood distributions following the maximization were used to determine statistical uncertainties for each parameter. One such profile can be seen in Figure 4.26, showing the log-likelihood distribution for the energy parameter of one resonance. The highest value in the log-likelihood profile is the parameter best value, which corresponds to the likelihood maximum of all parameters.

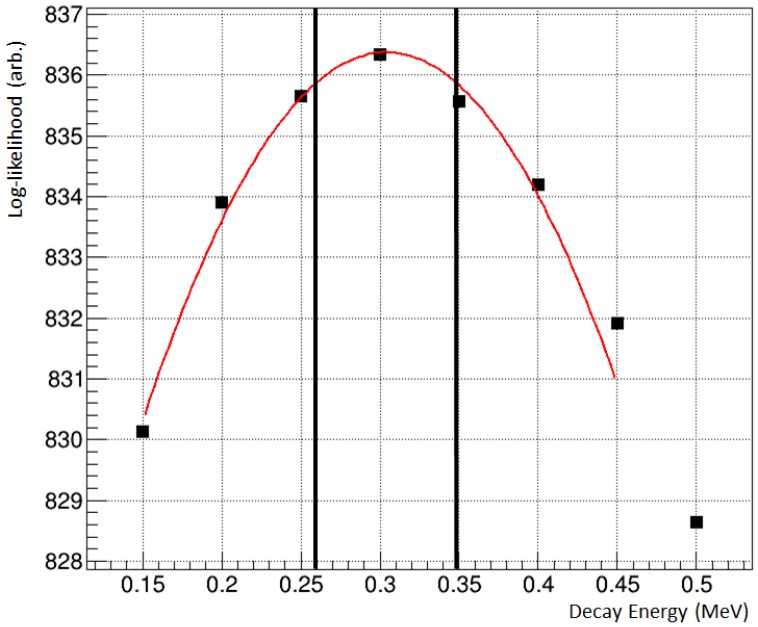

Figure 4.26: The log-likelihood distribution for the energy parameter for one resonance. A second-order polynomial fit (red curve) is applied to extract an uncertainty from the calculation, indicated by the vertical bars. The highest value is that which maximizes the likelihood for all parameters.

Chapter 5

Results and Discussion

5.1 Resolution and acceptance

In order to usefully interpret the decay energy spectrum, the experimental setup acceptance and resolution was characterized using the simulation package discussed in Section 4.5.

The acceptance was determined by the physical dimensions of the CRDCs detecting the charged particles and the vertical gap in the sweeper magnet which restricts the neutron cone detected in MoNA-LISA. The resolution of the setup was attained by a Monte Carlo simulation in which a uniform energy distribution was propagated through the experimental setup and requirements for physical dimensions were imposed. Figure 5.1 shows the acceptance of the experimental setup as a function of decay energy.

The experimental resolution was estimated by modeling a neutron decay as a delta function energy distribution and the events were propagated through the experimental setup, including resolution effects from the individual detectors used. The width of the resulting two-body decay energy distribution was fit with a Gaussian function to extract a width which determines the resolution at the input energy. The result of this calculation can be seen in Figure 5.2.

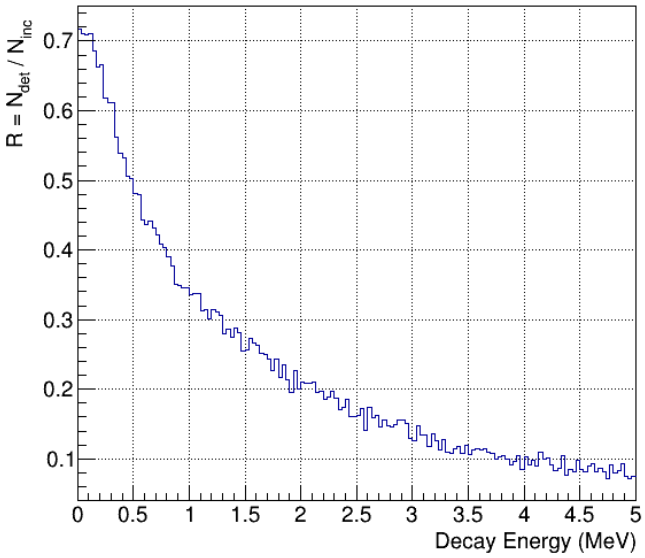

Figure 5.1: The simulated acceptance of the experimental setup, shown as the fraction of detected and incident events as a function of decay energy.

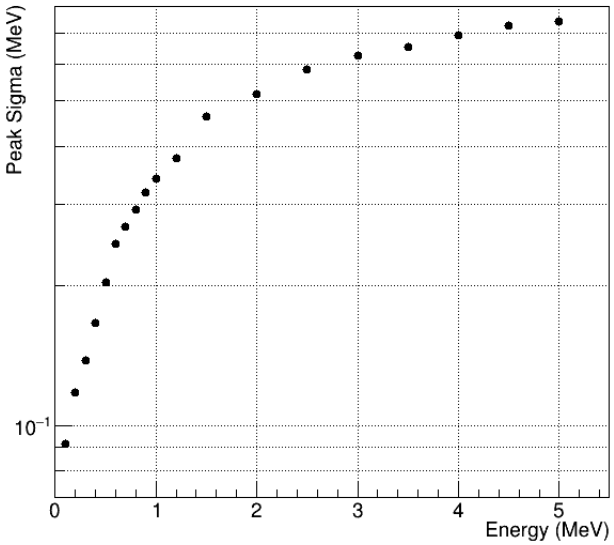

Figure 5.2: The simulated resolution of the experimental setup in terms of the reconstructed width of an input delta function as a function of the two-body decay energy.

5.2 Results

5.2.1 Two-body decay energy

The measured two-body decay energy represents the energy released in a one-neutron decay from neutron-unbound excited states in ^{31}Ne to a state in ^{30}Ne. The measured spectrum is shown in Figure 5.3. Determining the energy of a neutron-unbound excited state of ^{31}Ne relative to its ground state relies on knowledge of the one-neutron separation energy, which at present has a large uncertainty at $S_n = 170 \pm 130$ keV [66].

The fit to the decay energy distribution requires at least two resonances to describe the shape of the spectrum. The line shape of the simulated resonances is an asymmetric Breit-Wigner line shape as discussed in section 2.3.1.2.

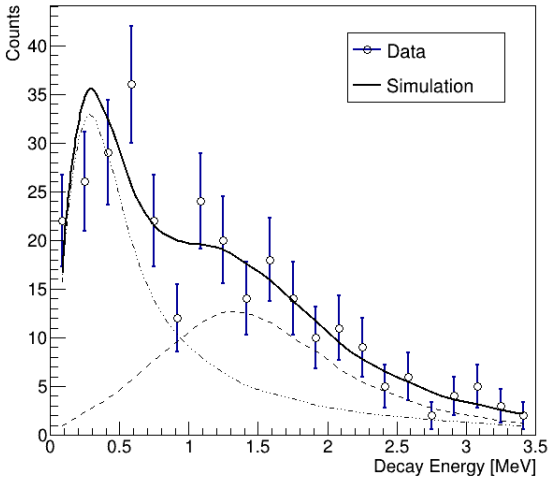

Figure 5.3: The measured two-body decay energy spectrum for the ^{30}Ne + n coincidences. The open circles are the data points. The curves are the individual line shapes of the individual decays fit to the spectrum at 300 keV (dot-dot-dash) and 1.5 MeV (dashed), with the solid black curve as the sum of these decays.

The data was fit using a method of maximum likelihood outlined in section 4.5.4.1. The free parameters of the fit were a central energy for each resonant decay, E_n, an associated

decay width, Γ_n, the orbital angular momentum l_n, and the relative contributions of each line shape. The likelihood was not sensitive to the width of the line shape, but indicates it is broader than the experimental resolution, requiring a width of at least 1 MeV to fit the decay energy spectrum as shown in Figure 5.5. The angular momentum value of the decay was expected to have negative parity and was fixed at $l = 1$ for this analysis; use of $l = 3$ to model the decay did not indicate an appreciable difference in the log-likelihood statistic. The relative scale factor was treated as a nuisance parameter for the likelihood analysis.

The remaining free parameters were the central energies for each decay, for which a best fit and a 1σ uncertainty was extracted. These uncertainties were obtained by varying parameters across a physically reasonable range and examining the likelihood statistic profile for each parameter following the methods of [65]. This profile was constructed by calculating a log-likelihood for different values of one parameter where all other parameters were held constant; this was extended to all dimensions of the fit and a global maximum likelihood was found. The likelihood statistic used will converge to a χ^2 distribution in the large sample limit, exhibiting a near-parabolic shape at its maximum (or minimum for a χ^2 analysis) which can be fit to extract a 1σ uncertainty, determined by the parameter value at which the likelihood statistic falls to its maximum value minus a value of $\frac{1}{2}$ (see equation 4.13). One such profile, shown in Figure 5.4, shows the likelihood statistic as a function of the energy of the first resonance.

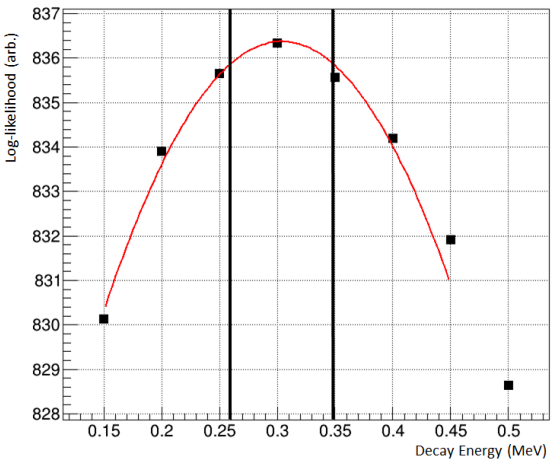

Figure 5.4: The log-likelihood statistic as a function of the energy for the first resonance. A global maximum likelihood is found, indicating a best set of parameters. Data points are the likelihood statistic using various values of a central energy; all other parameters are fixed at the value found by the maximization routine.

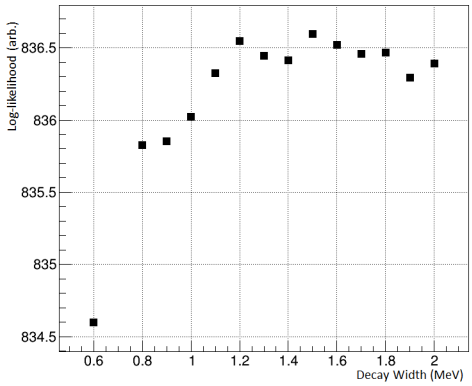

Figure 5.5: The log-likelihood statistic as a function of the decay width of the 300 keV resonance. Data points are the likelihood statistic using various values of a decay width; all other parameters are fixed at the value found by the maximization routine.

The fit using two resonances results in decay energies of 0.30±0.17 MeV and 1.50±0.33 MeV. The uncertainties quoted represent the uncertainties of the log-likelihood fit and include the detector resolutions and acceptance of the experimental setup. The energy resolutions of the experimental setup at these energies are roughly 150 keV and 370 keV respectively.

5.2.2 Theory calculations

To get information about potentially populated ^{31}Ne excited states, cross-section and shell model calculations were performed to generate a theoretical decay energy spectrum. Theory background for this modeling is covered in Chapter 2.

The cross-sections populating ^{31}Ne* are shown in Figure 5.6. The secondary beam nucleus ^{33}Mg has a ground state spin-parity of $\frac{3}{2}^-$ and only the negative-parity states of ^{31}Ne are populated through the two-proton knockout reaction. Therefore, only negative-parity ^{31}Ne* states were calculated.

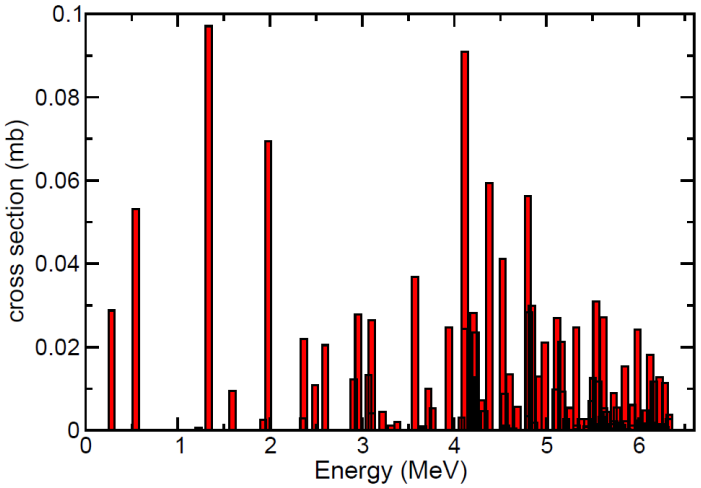

Figure 5.6: Two-proton knockout cross sections to the first 30 negative parity unbound states of each spin as a function of the ^{31}Ne* energy above threshold.

The corresponding spectroscopic factors were calculated for ^{31}Ne* decaying to the 0^+, 2^+, and 4^+ states of ^{30}Ne. A summary of the more strongly populated levels, their spin-parity, and their cross-sections including spectroscopic factors are listed in Table 5.1. Only levels in ^{31}Ne with a cross section for the one neutron decay to ^{30}Ne + n larger than 0.020 mb are shown.

Table 5.1: Calculated cross sections (σ) for the ^{33}Mg$(-2\mathrm{p})^{31}$Ne* and ^{31}Ne$^* \rightarrow {}^{30}$Ne + n decays larger than 0.020 mb. This cross-section folds in spectroscopic factors pertaining to a specific decay. E_x is the energy of the ^{31}Ne level, E_n is the decay energy and Γ_t is the decay width for each of the spin parity states J^π.

$2J^\pi$	E_x (MeV)	σ (mb)	J^π_f	E_n (MeV)	Γ_t (MeV)
5^-	0.43	0.029	0^+	0.26	0.004
7^-	0.70	0.053	0^+	0.53	0.157
9^-	1.49	0.097	2^+	0.52	0.167
11^-	2.13	0.069	2^+	1.17	0.367
7^-	2.52	0.022	2^+	1.56	0.541
5^-	3.11	0.027	2^+	2.15	0.698
7^-	3.72	0.032	4^+	1.32	0.423
7^-	4.27	0.086	4^+	1.86	0.464
7^-	4.36	0.022	4^+	1.95	0.275
5^-	4.53	0.027	2^+	3.57	0.468
5^-	4.53	0.027	4^+	2.13	0.468
7^-	4.95	0.054	4^+	2.54	0.129
11^-	4.99	0.023	4^+	2.59	0.215

5.3 Discussion

The first feature of the two-body decay energy is a low-lying peak, fit with a resonant line shape at $E_\mathrm{n} = 0.30 \pm 0.17$ MeV. The shell model predicts three states ($9/2^-, 7/2^-$ and $5/2^-$) with associated decay energies consistent with this measurement (see Figure 5.7). The $\frac{9}{2}^-$ state at 1.49 MeV has the largest cross section from the two-proton knockout at 0.097 mb and the decay to the 2^+ state in ^{30}Ne would give an E_n of 0.52 MeV. The $\frac{7}{2}^-$ state at 0.70 MeV has a cross section of 0.053 mb and a decay to the ground state of ^{30}Ne would result in an E_n of 0.53 MeV. These two decays are close in energy, but populate different daughter states in ^{30}Ne. The absence of γ ray detection in our setup means these two decays cannot be resolved. A third decay consistent with this energy is of the first excited state of ^{31}Ne, with a spin-parity of $\frac{5}{2}^-$ at 0.43 MeV, decaying to the ground state of ^{30}Ne, with a decay energy of 0.26 MeV. The widths of these individual decays are narrow (less than 200 keV,

see Table 5.1).

The second resonance in the maximum likelihood fit is at $E_{\mathrm{n}} = 1.50 \pm 0.33$ MeV above the neutron threshold. There are multiple calculated decays that are consistent with this measurement. The $\frac{11}{2}^-$ at 2.13 MeV decaying to the 2^+ state in ^{30}Ne is predicted to be a prominent decay with an E_{n} of 1.17 MeV. Also consistent with this measurement is the $\frac{7}{2}^-$ state at 3.72 MeV to the 4^+ state of ^{30}Ne with an E_{n} of 1.32 MeV.

The first $\frac{9}{2}^-$ state in ^{31}Ne decaying to the ground state of ^{30}Ne is also consistent with this measured decay energy, however it is outside the model space of the shell model calculations performed. The single-particle decay width for an $l = 5$ decay is about 0.026 keV. The spectroscopic factor for mixing an $h_{9/2}$ orbital about 30 MeV above the $0f_{7/2}$ must be less than about 0.01. This indicates a width for the decay to 0^+ being less than 0.26 eV; which is not expected to compete with the decay to 2^+ which has a decay width of 0.167 MeV (see Table 5.1). A level scheme based on experimental data and levels from shell model calculations can be seen in Fig. 5.7. The center panel shows energy levels that the 300 keV and 1.5 MeV decays could potentially originate from. On the right panel is the shell model prediction, with bar length representing the two-proton knockout cross-section to that state.

The cross-sections (Figure 5.6) show a non-negligible strength up to roughly 6.5 MeV in ^{31}Ne where the calculation was truncated. Decays were calculated from these populated ^{31}Ne* states to the ground state or either of the first two excited states of ^{30}Ne. The enhanced cross sections, the high density of the predicted excited states, and the multiple potential decay paths imply a complex decay scenario. In total, there are 140 potential decays to consider when the cross section requirement is relaxed to 0.001 mb. The decay energy spectrum of all calculated decays is shown in Figure **??**.

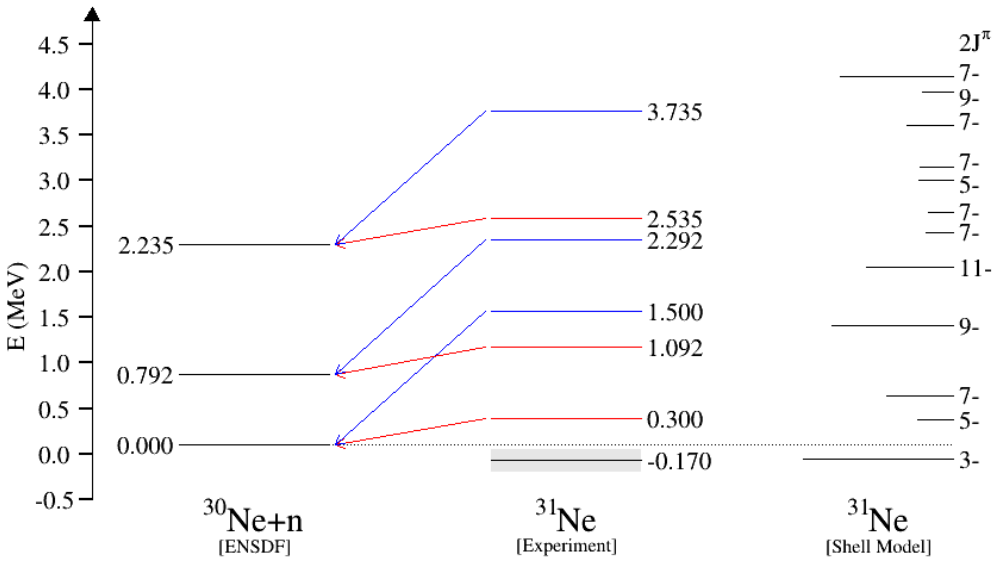

Figure 5.7: Decay energy and level scheme for the decay of ^{31}Ne into ^{30}Ne + n. The left level scheme shows states in ^{30}Ne from the Evaluated Nuclear Structure Data File (ENSDF). In the center are levels potentially observed by the present experiment, color coded by the measured decay energies (see text for detail). The arrows specify potential decay paths to states in ^{30}Ne. The right spectrum shows the NuShellX calculations with the length of the bars (excluding the ground state) indicating a population cross section from the two-proton knockout. Energies listed are relative to the one-neutron separation energy of ^{31}Ne.

The two-neutron separation energy for ^{31}Ne, beyond which two neutron decay would be possible, is at $S_{2n} = 3.72 \pm 1.62$ MeV [67] for ^{31}Ne. The reaction theory predicts a significant cross section for populating a number of states above this energy which may be subject to two-neutron decay. It is not possible to say, within the scope of the reaction and structure theory, how much mixing there is for one-neutron and two-neutron decays. Therefore, the reality lies in between two extremes. Either every ^{31}Ne* state decays via one-neutron decay or only ^{31}Ne* states below S_{2n} decay via one-neutron decay. In reality, these processes compete and an accurate picture of this complex decay spectrum lies in between the two. The overlap between these cases is shown in Figure 5.9 overlaid with the data points. The shape of the measured data spectrum is consistent with the predictions of the shell model

calculations.

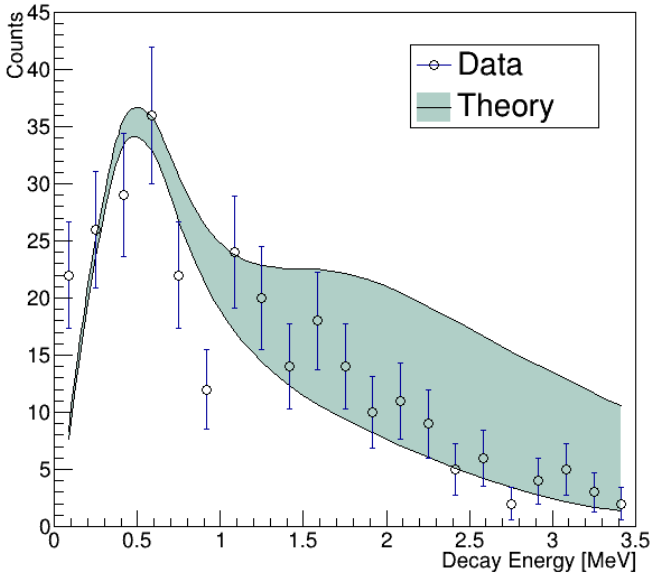

Figure 5.9: Solid lines represent theoretical spectra. The larger distribution (top line) assumes one neutron decay for all calculated ^{31}Ne states. The smaller distribution (bottom line) includes decays only from states in ^{31}Ne below $S_{2n} = 3.72 \pm 1.62$ MeV. The open markers indicate the measured spectrum. The only free parameter for this comparison is the overall scaling.

Chapter 6

Summary and Conclusions

This work studied the neutron-unbound excited states of ^{31}Ne for the first time using the method of invariant mass spectroscopy. The population of these states originated from a two-proton knockout reaction from an 88 MeV/nucleon ^{33}Mg incident beam provided by the NSCL coupled cylcotron facility at Michigan State University. The ^{31}Ne nucleus exhibits a halo structure with an un-paired valence neutron which is loosely bound. Due to the low one-neutron separation energy, it is predicted that low-lying states would be neutron-unbound. The valence neutron is emitted immediately following the population of ^{31}Ne neutron-unbound excited states. The neutron was detected by a large plastic scintillator array (MoNA-LISA) and the ^{30}Ne charged fragment nucleus was deflected by a large-gap dipole magnet and detected with a suite of charged particle detectors. The decay energy spectrum was fit with a Breit-Wigner distribution, representing a resonant decay characterized by a central energy and width. This decay line shape was propagated through a simulated experimental setup with resolution and acceptance effects before it was compared with experimental data.

The decay energy spectrum resulting from the invariant mass calculation exhibited two features that were fit as resonant decays, resulting in central energies of 300 keV and 1.50 MeV, respectively. The widths of these distributions are determined through the fit to be

much larger than the resolution of the experimental devices.

Interpretations of this data were guided by both reaction and structure theory. The two-proton knockout cross sections to ^{31}Ne excited states were calculated using the eikonal model (section 2.3.1.1) and spectroscopic factors (section 2.2) for overlaps with ^{30}Ne were calculated to describe the one-neutron decay. The results indicate a complicated decay scenario due to substantial two proton knockout cross-sections populating ^{31}Ne* states up to roughly 6 MeV, shown in Figure 5.6.

Table 6.1: Summary table of potentially observed decays. These entries have a cross-section greater than 0.02 mb. The first column specifies the fits to the spectrum that were obtained. The next two columns pertain to the ^{31}Ne nucleus. The cross-section listed in the fourth column contains the spectroscopic factor for the specified decay folded in. The last two columns pertain to the daughter nucleus ^{30}Ne.
*This resonant decay is outside the scope of the shell model calculations performed [see text].

E_{fit} (MeV)	$2J^{\pi}$ (MeV)	$E_{\rm n}$ (MeV)	σ (mb)	E_x (MeV)	J^{π}_f ^{30}Ne
0.300	9/2-	0.52	0.097	1.49	2+
	7/2-	0.53	0.053	0.70	0+
	5/2-	0.26	0.029	0.43	0+
1.50	11/2-	0.069	1.17	2.13	2+
	7/2-	0.032	1.32	3.72	4+
	9/2-*	0.097	0.091.49	1.49	0+

The first feature of the two-body decay energy was fit with a resonant line shape at a central energy of $E_{\rm n} = 0.30 \pm 0.17$ MeV. The method of maximum likelihood utilized was not sensitive to the decay width parameter, but indicates it is larger than the experimental resolution, requiring at least 1 MeV to reproduce the spectrum. The shell model predicts three states with associated decay energies consistent with this measurement. The $\frac{9}{2}^-$ state at 1.49 MeV has the largest cross section from the two-proton knockout at 0.097 mb and the decay to the 2^+ state in ^{30}Ne would give an $E_{\rm n}$ of 0.52 MeV. The $\frac{7}{2}^-$ state at 0.70 MeV has a cross section of 0.053 mb and a decay to the ground state of ^{30}Ne would result in an $E_{\rm n}$

of 0.53 MeV. These two decays are close in energy, but populate different daughter states in ^{30}Ne. Unfortunately, the absence of γ ray detection in our setup does not allow us to resolve these two decays. A third decay consistent with this energy is of the first excited state of ^{31}Ne, with a spin-parity of $\frac{5}{2}^-$ at 0.43 MeV, decaying to the ground state of ^{30}Ne, with a decay energy of 0.26 MeV. The widths of these individual decays are narrow (less than 200 keV, see Table 5.1). The resolution of the detector setup a this energy is roughly 150 keV. The large width of the fit necessary to describe this feature of the spectrum suggests this "resonance" is a group of unresolved resonant decays.

The second resonance extracted from the maximum likelihood fit is $E_\mathrm{n} = 1.50 \pm 0.33$ MeV above the neutron threshold. There are multiple calculated decays that are consistent with this measurement. The $\frac{11}{2}^-$ state at 2.13 MeV decaying to the 2^+ state in ^{30}Ne is predicted to be a prominent decay with an E_n of 1.17 MeV. Also consistent with this measurement is another prominent decay of the $\frac{7}{2}^-$ state at 3.72 MeV to the 4^+ state of ^{30}Ne with an E_n of 1.32 MeV. It is also worth noting that although the decay from the first $\frac{9}{2}^-$ state in ^{31}Ne decaying to the ground state of ^{30}Ne is consistent with this measured decay energy, it is outside the model space of the shell model calculations performed. The single-particle decay width for the $l = 5$ decay required is about 0.026 keV. The spectroscopic factor for mixing an $h_{9/2}$ orbital about 30 MeV above the $0f_{7/2}$ must be less than about 0.01. This indicates a width for the decay to 0^+ being less than 0.26 eV; which is not expected to compete with the decay to 2^+ which has a decay width of 0.167 MeV.

The cross-sections show a considerable strength up to roughly 6.5 MeV in ^{31}Ne where the calculation was truncated. Decays were calculated from these populated ^{31}Ne* states to the ground state or either of the first two excited states of ^{30}Ne. The enhanced cross sections,

the high density of the predicted excited states, and the multiple potential decay paths imply a complicated decay scenario. In total, the shell model calculations provide 140 decays to consider when the cross section requirement is relaxed to 0.001 mb.

The two-neutron separation energy for ^{31}Ne, beyond which two neutron decay would be possible, is at S_{2n} = 3.72 MeV [67] for ^{31}Ne. The reaction theory predicts a significant cross section for a number of states above this energy which may be subject to two-neutron decay. It is not possible to say, within the scope of the reaction and structure theory implemented, how much mixing there is for one-neutron and two-neutron decays. Therefore, the reality lies in between two extremes. Either every ^{31}Ne* state decays via one-neutron decay, or only ^{31}Ne* states below S_{2n} decay via one-neutron decay. In reality, these processes compete and an accurate picture of this complex decay spectrum lies in between the two assumptions.

The puzzle of ^{31}Ne neutron-unbound excited states was approached in this work for the first time. The resonant decays which fit the observed decay energy spectrum are best interpreted as groups of closely-spaced resonances which the current experimental setup is not able to discriminate. This is supported by the shell model calculations performed for this work, which indicate many low-lying states populated in the two-proton knockout. From the compilation of all states calculated, it is reasonable to conclude that many decays were likely observed, but conclusions are limited by the experimental resolution and the absence of γ-ray detection. This work suggests that the observed decay of ^{31}Ne is consistent with the predictions of the shell model due to the agreement with the predicted spectrum and the predicted decay candidates falling within the uncertainty of the decay parameters extracted by the fit.

There are ways in which this experiment could be expanded upon to improve the current interpretation of the decay scenario and the structure of ^{31}Ne. The most notable of these efforts would be to narrow down the large uncertainty in the one-neutron separation energy measurement of ^{31}Ne ($S_n = 0.15^{+\ 0.16}_{-\ 0.10}$ MeV) which affects the interpretation of the decay energy measurements relative to the ^{31}Ne ground state. Furthermore, the addition of γ-ray detectors around the target position would provide information about which daughter states in ^{30}Ne are populated in the decay of ^{31}Ne. For example, there are two competing decays with almost identical energies that lie within the $E_{\mathrm{n}} = 0.30 \pm 0.17$ MeV fit to the spectrum but decay to different daughter states in ^{30}Ne. The interpretation of the gathered data is also limited by the production rate of ^{31}Ne nuclei. A subsequent experiment could be performed with a higher ^{31}Ne production rate, available with advanced beam production facilities such as the Facility for Rare Isotope Beams (FRIB) at Michigan State University. These considerations would provide an improved understanding of the decay of the exotic ^{31}Ne nucleus and provide information pertaining to systematic evolution of nuclear structure near the neutron drip line, particularly in the N=20 island of inversion.

REFERENCES

REFERENCES

[1] NNDC. National Nuclear Data Center, https://www.nndc.bml.gov.

[2] B. Alex Brown. *Lecture Notes in Nuclear Structure Physics*. Michigan State University, 2017.

[3] E. K. Warburton, J. A. Becker, and B. A. Brown. Mass systematics for $A = 29 - -44$ nuclei: The deformed A$\sim$32 region. *Phys. Rev. C*, 41:1147–1166, Mar 1990.

[4] E. Caurier, F. Nowacki, and A. Poves. Merging of the islands of inversion at $N = 20$ and $N = 28$. *Phys. Rev. C*, 90:014302, Jul 2014.

[5] K. Minomo, T. Sumi, M. Kimura, K. Ogata, Y. R. Shimizu, and M. Yahiro. Determination of the structure of ^{31}Ne by a fully microscopic framework. *Phys. Rev. Lett.*, 108:052503, Jan 2012.

[6] M Thoennessen. Reaching the limits of nuclear stability. *Rep. Prog. Phys.*, 67(7):1187–1232, jun 2004.

[7] S. R. Beane, W. Detmold, K. Orginos, and M.J. Savage. Nuclear physics from lattice QCD. *Progress in Particle and Nuclear Physics*, 66(1):1–40, 2011.

[8] Steven Weinberg. Phenomenological lagrangians. *Physica A: Statistical Mechanics and its Applications*, 96(1):327–340, 1979.

[9] R. Machleidt and D. R. Entem. Chiral effective field theory and nuclear forces. *Physics Reports*, 503(1):1–75, 2011.

[10] S. A. Giuliani, Z. Matheson, W. Nazarewicz, E. Olsen, P.-G. Reinhard, J. Sadhukhan, B. Schuetrumpf, N. Schunck, and P. Schwerdtfeger. Colloquium: Superheavy elements: Oganesson and beyond. *Rev. Mod. Phys.*, 91:011001, Jan 2019.

[11] A.V. Afanasjev, S.E. Agbemava, and A. Gyawali. Hyperheavy nuclei: existence and stability. *Physics Letters B*, 782:533–540, 2018.

[12] G. Gamow. Zur Quantentheorie des Atomkernes. *Zeitschrift fur Physik*, 51(3-4):204–212, March 1928.

[13] M. G. Mayer. Nuclear configurations in the spin-orbit coupling model. i. empirical evidence. *Phys. Rev.*, 78:16–21, Apr 1950.

[14] M. G. Mayer. Nuclear configurations in the spin-orbit coupling model. ii. theoretical considerations. *Phys. Rev.*, 78:22–23, Apr 1950.

[15] Otto Haxel, J. Hans D. Jensen, and Hans E. Suess. On the "magic numbers" in nuclear structure. *Phys. Rev.*, 75:1766–1766, Jun 1949.

[16] N. Fukunishi, T. Otsuka, and T. Sebe. Vanishing of the shell gap in $N = 20$ neutron-rich nuclei. *Physics Letters B*, 296(3):279–284, 1992.

[17] A. Poves and J. Retamosa. The onset of deformation at the $N = 20$ neutron shell closure far from stability. *Physics Letters B*, 184(4):311–315, 1987.

[18] P. G Hansen and B Jonson. The neutron halo of extremely neutron-rich nuclei. *Europhysics Letters (EPL)*, 4(4):409–414, aug 1987.

[19] C. Thibault, R. Klapisch, C. Rigaud, A. M. Poskanzer, R. Prieels, L. Lessard, and W. Reisdorf. Direct measurement of the masses of ^{11}Li and $^{26-32}$Na with an on-line mass spectrometer. *Phys. Rev. C*, 12:644–657, Aug 1975.

[20] B. H. Wildenthal and W. Chung. Collapse of the conventional shell-model ordering in the very-neutron-rich isotopes of Na and Mg. *Phys. Rev. C*, 22:2260–2262, Nov 1980.

[21] A. Poves and J. Retamosa. Theoretical study of the very neutron-rich nuclei around $N = 20$. *Nuclear Physics A*, 571(2):221–241, 1994.

[22] S. G. Nilsson. Binding states of individual nucleons in strongly deformed nuclei. *Kong. Dan. Vid. Sel. Mat. Fys. Med.*, 29N16:1–69, 1955.

[23] J. L. Wood and K. Heyde. A focus on shape coexistence in nuclei. *Journal of Physics G: Nuclear and Particle Physics*, 43(2):020402, 2016.

[24] T. Nakamura, N. Kobayashi, Y. Kondo, Y. Satou, N. Aoi, H. Baba, S. Deguchi, N. Fukuda, J. Gibelin, N. Inabe, M. Ishihara, D. Kameda, Y. Kawada, T. Kubo,

K. Kusaka, A. Mengoni, T. Motobayashi, T. Ohnishi, M. Ohtake, N. A. Orr, H. Otsu, T. Otsuka, A. Saito, H. Sakurai, S. Shimoura, T. Sumikama, H. Takeda, E. Takeshita, M. Takechi, S. Takeuchi, K. Tanaka, K. N. Tanaka, N. Tanaka, Y. Togano, Y. Utsuno, K. Yoneda, A. Yoshida, and K. Yoshida. Halo structure of the island of inversion nucleus ^{31}Ne. *Phys. Rev. Lett.*, 103:262501, Dec 2009.

[25] T. Nakamura, N. Kobayashi, Y. Kondo, Y. Satou, J. A. Tostevin, Y. Utsuno, N. Aoi, H. Baba, N. Fukuda, J. Gibelin, N. Inabe, M. Ishihara, D. Kameda, T. Kubo, T. Motobayashi, T. Ohnishi, N. A. Orr, H. Otsu, T. Otsuka, H. Sakurai, T. Sumikama, H. Takeda, E. Takeshita, M. Takechi, S. Takeuchi, Y. Togano, and K. Yoneda. Deformation-driven p-wave halos at the drip line: ^{31}Ne. *Phys. Rev. Lett.*, 112:142501, Apr 2014.

[26] Y. Utsuno, T. Otsuka, T. Mizusaki, and M. Honma. Varying shell gap and deformation in $N \sim 20$ unstable nuclei studied by the Monte Carlo shell model. *Phys. Rev. C*, 60:054315, Oct 1999.

[27] H. Sakurai, N. Aoi, A. Goto, M. Hirai, N. Inabe, M. Ishihara, H. Kobinata, T. Kubo, H. Kumagai, T. Nakagawa, T. Nakamura, M. Notani, Y. Watanabe, Y. Watanabe, and A. Yoshida. Production and identification of new neutron-rich nuclei, ^{31}Ne and ^{37}Mg, in the reaction 80A mev ^{50}Ti+^{181}Ta. *Phys. Rev. C*, 54:R2802–R2805, Dec 1996.

[28] D. Guillemaud-Mueller, J. C. Jacmart, E. Kashy, A. Latimier, A. C. Mueller, F. Pougheon, A. Richard, Yu. E. Penionzhkevich, A. G. Artuhk, A. V. Belozyorov, S. M. Lukyanov, R. Anne, P. Bricault, C. Détraz, M. Lewitowicz, Y. Zhang, Yu. S. Lyutostansky, M. V. Zverev, D. Bazin, and W. D. Schmidt-Ott. Particle stability of the isotopes ^{26}O and ^{32}Ne in the reaction 44 MeV/nucleon ^{48}Ca+Ta. *Phys. Rev. C*, 41:937–941, Mar 1990.

[29] B. Jurado, H. Savajols, W. Mittig, N. A. Orr, P. Roussel-Chomaz, D. Baiborodin, W. N. Catford, M. Chartier, C. E. Demonchy, Z. Dlouhý, A. Gillibert, L. Giot, A. Khouaja, A. Lépine-Szily, S. Lukyanov, J. Mrazek, Y. E. Penionzhkevich, S. Pita, M. Rousseau, and A. C. Villari. Mass measurements of neutron-rich nuclei near the $N = 20$ and 28 shell closures. *Physics Letters B*, 649(1):43–48, 2007.

[30] M. Takechi, T. Ohtsubo, T. Kuboki, Mitsunori Fukuda, D. Nishimura, Takeshi Suzuki, Taiyo Yamaguchi, A. Ozawa, Tatuya Moriguchi, T. Sumikama, H. Geissel, N. Aoi, Naoki Fukuda, I. Hachiuma, N. Inabe, Y. Ishibashi, Y. Itoh, D. Kameda, K. Kusaka, and Tomoha Kubo. Measurements of nuclear radii for neutron-rich Ne isotopes ^{2832}Ne. *Nuclear Physics A*, 834:412, 03 2010.

[31] M. Takechi, T. Ohtsubo, T. Kuboki, M. Fukuda, D. Nishimura, T. Suzuki, T. Yamaguchi, A. Ozawa, T. Moriguchi, T. Sumikama, H. Geissel, N. Aoi, N. Fukuda, I. Hachiuma, N. Inabe, Y. Ishibashi, Y. Itoh, D. Kameda, T. Kubo, K. Kusaka, M. Lantz, M. Mihara, Y. Miyashita, S. Momota, K. Namihira, H. Ohishi, Y. Ohkuma, T. Ohnishi, M. Ohtake, K. Ogawa, Y. Shimbara, T. Suda, S. Suzuki, H. Takeda, K. Tanaka, R. Watanabe, M. Winkler, Y. Yanagisawa, Y. Yasuda, K. Yoshinaga, A. Yoshida, and K. Yoshida. Measurements of interaction cross sections towards neutron-rich ne isotopes at ribf. *Modern Physics Letters A*, 25(21-23):1878–1881, 2010.

[32] M. Takechi, T. Ohtsubo, M. Fukuda, D. Nishimura, T. Kuboki, T. Suzuki, T. Yamaguchi, A. Ozawa, T. Moriguchi, H. Ooishi, D. Nagae, H. Suzuki, S. Suzuki, T. Izumikawa, T. Sumikama, M. Ishihara, H. Geissel, N. Aoi, Rui-Jiu Chen, De-Qing Fang, N. Fukuda, I. Hachiuma, N. Inabe, Y. Ishibashi, Y. Ito, D. Kameda, T. Kubo, K. Kusaka, M. Lantz, Yu-Gang Ma, K. Matsuta, M. Mihara, Y. Miyashita, S. Momota, K. Namihira, M. Nagashima, Y. Ohkuma, T. Ohnishi, M. Ohtake, K. Ogawa, H. Sakurai, Y. Shimbara, T. Suda, H. Takeda, S. Takeuchi, K. Tanaka, R. Watanabe, M. Winkler, Y. Yanagisawa, Y. Yasuda, K. Yoshinaga, A. Yoshida, and K. Yoshida. Interaction cross sections for Ne isotopes towards the island of inversion and halo structures of ^{29}Ne and ^{31}Ne. *Physics Letters B*, 707(3):357–361, 2012.

[33] W. Horiuchi, Y. Suzuki, P. Capel, and D. Baye. Probing the weakly-bound neutron orbit of ^{31}Ne with total reaction and one-neutron removal cross sections. *Phys. Rev. C*, 81:024606, Feb 2010.

[34] I. Hamamoto. Interpretation of Coulomb breakup of ^{31}Ne in terms of deformation. *Phys. Rev. C*, 81:021304, 2010.

[35] Shubhchintak and R. Chatterjee. Deformation effects in the Coulomb breakup of ^{31}Ne. *Nuclear Physics A*, 922:99–111, 2014.

[36] Y. Urata, K. Hagino, and H. Sagawa. Ground state properties and Coulomb dissociation of the deformed halo nucleus ^{31}Ne. *Phys. Rev. C*, 83:041303, Apr 2011.

[37] Y. Urata, K. Hagino, and H. Sagawa. Reaction cross sections of the deformed halo nucleus ^{31}Ne. *Phys. Rev. C*, 86:044613, Oct 2012.

[38] K. Minomo, T. Sumi, M. Kimura, K. Ogata, Y. R. Shimizu, and M. Yahiro. Deformation effect on total reaction cross sections for neutron-rich Ne isotopes. *Phys. Rev. C*, 84:034602, Sep 2011.

[39] T. Sumi, K. Minomo, S. Tagami, M. Kimura, T. Matsumoto, K. Ogata, Y. R. Shimizu, and M. Yahiro. Deformation of Ne isotopes in the region of the island of inversion. *Phys. Rev. C*, 85:064613, Jun 2012.

[40] M. Kimura, N. Furutachi, Y. Taniguchi, Y. Kanada-En'yo, and H. Horiuchi. Clustering aspects of highly excited states and neutron-rich nuclei. *Progress of Theoretical Physics Supplement*, 196:176–183, 10 2012.

[41] B. A. Brown and W. D. M. Rae. The Shell-Model code NuShellX@MSU. *Nuclear Data Sheets*, 120:115–118, 2014.

[42] R. S. Lubna, K. Kravvaris, S. L. Tabor, Vandana Tripathi, E. Rubino, and A. Volya. Evolution of the $N = 20$ and 28 shell gaps and two-particle-two-hole states in the fsu interaction. *Phys. Rev. Research*, 2:043342, Dec 2020.

[43] . J. Thompson and F. M. Nunes. *Nuclear Reactions for Astrophysics*. Cambridge University Press, New York, 2009.

[44] J. A. Tostevin and B. A. Brown. Diffraction dissociation contributions to two-nucleon knockout reactions and the suppression of shell-model strength. *Phys. Rev. C*, 74:064604, Dec 2006.

[45] F. Marti, P. Miller, D. Poe, M. Steiner, J. Stetson, and X. Y. Wu. Commissioning of the coupled cyclotron system at NSCL. *AIP Conference Proceedings*, 600, 12 2001.

[46] D. J. Morrissey, B. M. Sherrill, M. Steiner, A. Stolz, and I. Wiedenhoever. Commissioning the A1900 projectile fragment separator. *Nucl. Instrum. Meth.*, 204:90–96, 2003.

[47] I. Tanihata. Radioactive beam facilities and their physics programs. *Nucl. Phys. A*, 553:361–372, 1993.

[48] T. Redpath, T. Baumann, J. Brown, D. Chrisman, P.A. DeYoung, N. Frank, P. Guèye, A.N. Kuchera, H. Liu, C. Persch, S. Stephenson, K. Stiefel, M. Thoennessen, and D. Votaw. New segmented target for studies of neutron unbound systems. *Nuclear Instruments and Methods in Physics Research Section A: Accelerators, Spectrometers, Detectors and Associated Equipment*, 977:164284, 2020.

[49] T. Redpath. *Measuring the half-life of* ^{26}O. PhD thesis, Michigan State University, East Lansing, MI 48823, 2019.

[50] B. Luther, T Baumann, M Thoennessen, J. Brown, P. Deyoung, J Finck, J. Hinnefeld, R Howes, K Kemper, P. Pancella, G. Peaslee, W. Rogers, and S Tabor. Mona–the modular neutron array. *Nuclear Instruments and Methods in Physics Research Section A*, 505:33–35, 06 2003.

[51] N. Frank. *Spectroscopy of neutron unbound states in neutron rich oxygen isotopes*. PhD thesis, Michigan State University, East Lansing, MI 48823, 2006.

[52] G. Christian. *Spectroscopy of neutron-unbound fluorine*. PhD thesis, Michigan State University, East Lansing, MI 48823, 2011.

[53] M. Jones. *Spectroscopy of neutron unbound states in* ^{24}O *and* ^{23}N. PhD thesis, Michigan State University, East Lansing, MI 48823, 2015.

[54] D. Votaw. N=7 Shell Evolution at and Beyond the Neutron Dripline. PhD thesis, Michigan State University, East Lansing, MI 48823, 2019.

[55] Ron Fox. NSCLDAQ 11.2 documentation. http://docs.nscl.msu.edu/daq/newsite/nscldaq-11.2/index.html.

[56] Ron Fox. SpecTcl documentation. http://docs.nscl.msu.edu/daq/spectcl/.

[57] J.M. Paul. The density effect and rate of energy loss in common plastic scintillators. *Nuclear Instruments and Methods*, 96(1):51–59, 1971.

[58] K. Makino and M. Berz. COSY INFINITY Version 9. *Nuclear Instruments and Methods in Physics Research Section A*, 558(1):346 – 350, 2006. Proceedings of the 8^{th} International Computational Accelerator Physics Conference.

[59] J. Smith. *Unbound states in the lightest Island of Inversion: neutron decay measurements of* ^{11}Li, ^{10}Li, *and* ^{12}Be. PhD thesis, Michigan State University, East Lansing, MI 48823, 2014.

[60] H. Liu. *Reaction mechanism dependence of the population and decay of* ^{10}He. PhD thesis, Michigan State University, East Lansing, MI 48823, 2019.

[61] W. Peters. *Study of neutron unbound states using the modular neutron array (MoNA)*. PhD thesis, Michigan State University, East Lansing, MI 48823, 2007.

[62] A.S. Goldhaber. Statistical models of fragmentation processes. *Physics Letters B*, 53(4):306–308, 1974.

[63] K. Van Bibber, D. L. Hendrie, D. K. Scott, H. H. Weiman, L. S. Schroeder, J. V. Geaga, S. A. Cessin, R. Treuhaft, Y. J. Grossiord, J. O. Rasmussen, and C. Y. Wong. Evidence for orbital dispersion in the fragmentation of ^{16}O at 90 and 120 MeV/nucleon. *Phys. Rev. Lett.*, 43:840–844, Sep 1979.

[64] J. B. Birks. The specific fluorescence of anthracene and other organic materials. *Phys. Rev.*, 84:364–365, Oct 1951.

[65] Glen Cowan. *Statistical Data Analysis*. Clarendon Express, Oxford, 1998.

[66] M. Wang, W.J. Huang, F.G. Kondev, G. Audi, and S. Naimi. The AME2020 atomic mass evaluation (II). Tables, graphs and references. *Chinese Physics C*, 45(3):030003, 2021.

[67] M. Wang, G. Audi, A. H. Wapstra, F. G. Kondev, M. MacCormick, X. Xu, and B. Pfeiffer. The AME2012 atomic mass evaluation (II). Tables, graphs and references. *Chin.Phys.C*, 36:1603, 2012.